



The 4th ASEAN –UEC Workshop on Informatics and Engineering

Collaboration with ECTI Computer & Information Technology
and IEEE Computer Society, Thailand Chapter
Hybrid in Vietnam and Thailand in person as well as on line by Zoom

9 December 2022

Co main venue:

Le QuyDon Technical University, Hanoi, Vietnam
Burapha University, Chonburi, Thailand
held in parallel of On site and On line

The 4th ASEAN UEC Workshop 2022

Conference Organizer



on 9th December 2022 Co main venue: Le QuyDon Technical University, Hanoi, Vietnam
Burapha University, Chonburi, Thailand held in parallel of On site and On line

WELCOME MESSAGE FROM GENERAL CHAIRS



To create the stage for gathering researchers in ASEAN and Japan, the 1st Workshop entitled “ECTI & UEC Workshop on AI and Application” has been launched in 2019 at Rajamangala University of Technology Krungthep, Bangkok, Thailand. There were 24 poster papers presented at the workshop, and 13 professors, who were active and well known in AI fields, performed their invited talks. The poster papers were mainly submitted from Japan, Thailand, and ASEAN countries. Based on the success of the 1st workshop, the organizing committee considered to expand the network to ASEAN countries so that they decided to change the workshop title to "ASEAN-UEC Workshop". During COVID-19 pandemic, the workshop with new title has been held online by the team of ITB in Bandung, Indonesia in 2020, and KMUTNB, Bangkok, Thailand in 2021.

In 2022, the organizing committee decided to restart the 4th workshop in person, and modify the title to “ASEAN-UEC Workshop on Informatics and Engineering” in order to attract papers in hot issues in the fields of informatics and engineering. Then, the committee selected Le Quy Don Technical University (LQDTU) located in Hanoi as the main venue of the workshop due to many active and high potential researchers in Vietnam. However, technologies of virtual meetings and conferences via internet have been dramatically improved and recently become popular by the needs during COVID-19, people get familiar

with remote work and online conference. The organizing committee utilized the emerged online conferencing technologies not only to invite world-level keynote speakers from remote countries but also offer convenience for local Thai researchers to attend in person by establishing another stage of the workshop at Burapha University (BUU), Chonburi, Thailand, and both of venues are virtually linked by the teleconferencing technologies.

The 4th ASEAN-UEC Workshop on Informatics and Engineering will be started by the opening ceremony and the keynote speech given by five world renown professors in the morning, and followed by poster sessions at LQDTU and BUU in the afternoon on Dec 9, 2022. On behalf of organizing committee, we look forward to welcoming all participants, and discussing with keynote speakers and all presenters in the workshop.

Hoang Van Phuc (LQDTU/VN)

Krisana Chinnasarn (BUU & ECTI & & IEEE Computer Soc. Thailand Chap./TH)

Kosin Chamnongthai (KMUTT & UAREC/TH)

Koichiro Ishibashi (UEC & UAREC/JP)

Pham Cong-Kha (UEC & UAREC/JP)

COMMITTEE

General Co Chairs:

Hoang Van Phuc, LQDTU/VN

Krisana Chinnasarn, BUU & ECTI & IEEE Computer Soc. Thailand Chap./TH

Kosin Chamnongthai, KMUTT&UAREC/TH

Koichiro Ishibashi, UEC &UAREC/JP

Pham Cong-Kha, UEC &UAREC/JP

Local Arrangement:

Nguyen Van Trung, LQDTU/VN

Luong Duy Manh, LQDTU/VN

Program Committee Members:

Natapong Wongprommoon, SU/TH

Krit Angkeaw, KMUTNB/TH

Kamon Jirasereeamornkul, KMUTT/TH

Taworn Benjanarasuth, KMITL/TH

Nuttaphong Sornsuwit, KMUTNB/TH

Rachada Kongkachandra, TU/TH

I Gusti Bagus Baskara Nugraha, ITB/ID

Agung Tri Wijayanta, UNS/ID

Le Duc Hung, HCMUS/VN

Tran Ngoc Thinh, HCMUT/VN

Pham Nguyen Thanh Vinh, HCMUE/VN

Nguyen Thuy Linh, LQDTU/VN

Nguyen Quang Nhu Quynh DUT/VN

Luu Manh Ha, VNU-UET/VN

Han Trong Thanh, HUST/VN

Nattapong Kitsuwat, UEC/JP

Koji Enoki, UEC/JP

PROGRAM

Date: December 9, 2022

TIME	EVENT	SPEAKER
08:30 – 09:00	Registration	
		Prof. Tran Xuan Nam
		Prof. Kosin Chamnongthai
09:00 – 09:30	Opening Remarks	Prof. Koichiro Ishibashi
KEYNOTE SPEECH SESSION		
09:30 – 10:00	Advantages and challenges of Cell-free systems	Assoc. Prof. Pham Thanh Hiep
10:00 – 10:30	Trends and Challenges of AI Accelerator Design	Prof. Trio Adiono
	Neuron Function with Single Device by PN-Body	
	Tied SOI-FET and Activity on Cryo-CMOS for Quantum	
10:30 – 11:00	Computing	Prof. Jiro Ida
	Computer Design Classes Using Open-source	
	RICE-V: Linux Bootable SoC on FPGA and VLSI	
11:00 – 11:30	Implementations	Prof. Hoang Trong Thuc
11:30 – 13:00	Lunch Break	
13:00 – 13:30	Quality over quantity: An introduction to feature selection	Prof. Veronica Bolon-Canedo
13:30 – 15:30	Poster Recorded Video Presentations	
15:30 – 16:30	Poster Presentations	
16:30 – 17:00	Award and Wrap-up	
17:00 – 19:00	Banquet	

Table of Contents

Keynote Talks

- | | | |
|---|--|-----|
| 1 | Advantages and challenges of Cell-free systems
Assoc. Prof. Pham Thanh Hiep, Le Quy Don Technical University | I |
| 2 | Trends and Challenges of AI Accelerator Design
Prof. Trio Adiono, ITB | II |
| 3 | Neuron Function with Single Device by PN-Body Tied SOI-FET and Activity on Cryo-CMOS for Quantum Computing
Prof. Jiro Ida, Kanazawa Institute of Technology | III |
| 4 | Computer Design Classes Using Open-source RISC-V: Linux Bootable SoC on FPGA and VLSI Implementations
Prof. Hoang Trong Thuc, UEC | IV |
| 5 | Quality over quantity: An introduction to feature selection
Prof. Veronica Bolon-Canedo, UDC | V |

Regular Paper

- | | | |
|---|--|---|
| 1 | A Slanted-Edge Method for High-Accuracy Measurement of Modulation Transfer Function
Miu Fujita and Kazuki Nishi/ UEC | 1 |
| 2 | Real-Time Vital Sign Monitoring using 24 GHz Radar
Hoang Thi Yen and Guanghao Sun/ UEC | 3 |
| 3 | Analysis of Connection Characteristics between Random Sections and Patternized Groups in No-lane Heterogeneous Traffic
Akihito Nagahama and Kenji Tanaka/ UEC, Katsuhiro Nishinari/ U-Tokyo | 5 |
| 4 | Information presentation aiming intention share in ADAS
Yumeno Hatori, Akihito Nagahama, and Kenji Tanaka/ UEC | 7 |
| 5 | A Note on Correlation-Based Watermarking Scheme for Auto-RDS Images using 2-D Orthogonal Transforms
Shun Kitakaze and Hiromu Koda/ UEC | 9 |

6	A Review on Applications of Earth Observation Datasets in Ecological Vulnerability Assessment Muhammad Kamran, Kayoko Yamamoto/ UEC	11
7	Fabrication and characterization of CuAlO ₂ thin film transistor by Digitally Processed DC Reactive Sputtering Ali Mehdi and Hideo Isshiki/ UEC	13
8	Neutronics Design of Small 100MWe of Plutonium Fuelled Molten Salt Nuclear Power Plant A.Waris, C. Wulandari, S. Permana, and S. Pramuditya, I G B Baskara Nugraha/ ITB	15
9	Protecting Hot Carriers by Introducing Organic Cations in Halide Perovskite Quantum Dots Hua Li, Chao Ding and Qing Shen/ UEC	16
10	Automatic Allocation of Parking Lot's Lanes utilizing Methods of Image Processing and Machine Learning Apiwat Sangnoree/ UTCC	18
11	Cyclone Dust Collector: Apparatus Design and Analysis Ahmad Imam Rifa/ POLSRI, Budi Kristiawan/ UNS, Koji Enoki/ UEC, Agung Tri Wijayanta/ UNS	20
12	Impact of Several Terrain Clutter Models on Detection Performance of Bistatic Passive Radar System Using P1 Symbol in Vietnamese DVB-T2 Signals Quang Huy Duong and Tien Hai Nguyen/ LQDTU	22
13	Hybrid model SARIMA-LSTM based on data decomposition by STL for prediction PM _{2.5} in central district in Hanoi Nguyen Quang Dat/ HUS, Do Duy Nhat/ LQDTU	25
14	Title of Abstract: Acoustic, light-based Emergency Vehicle Detection using deep neural networks Nguyen Quang Dat, Dineshwar Doddapaneni, Vijender Kumar Solanki, Do Duy Nhat/ HUS	27
15	Preparation And Characterization of Activated Carbon from Coconut Shell Using Steam Activation Kinkind Raras Heliani, Fitria Rahmawati, Agung Tri Wijayanta/ UNS, Arika Fitonna Ridassepri/ UEC	29

16	Numerical Investigation on Heat Transfer Coefficient of TiO ₂ -CNTs/Water Nanofluids Sukmo Utomo Abdillah Amin/ UNS, Budi Kristiawan/ UNS, Koji Enoki/ UEC, Wibawa Endra Juwana/ UNS, Agung Tri Wijayanta/UNS	31
17	Vietnamese Sign Language Recognition using Mediapipe and Deep Learning Nghia Cao Xuan, Quang Nguyen Van and Trong Thanh Han/ HUST	33
18	Online deep neural networks model based multi seasonal decompose for short-term electricity load forecasting Nguyen Quang Dat/ HUS	35
19	Denoising methods for non-profile the side channel attack in hardware security evaluation Phu-Cuong Le, Van-Nam Le, Ngoc-Tuan Do and Van-Phuc Hoang/ LQDTU	37
20	High-order Chebyshev Notch Filter based on MO-OTA Siradanai Srisamranrungrueang, and Natapong Wongprommoon/ SU	39
21	Design QPSK Communication System by Software Defined Radio (SDR) Siraphop Tooprakai, Korpakit Kobthanyakit, and Tin Suwanmad/ KMITL	41
22	Recognition of Face Expression for Masked Face Images Susanta Malakar and Kosin Chamnongthai/ KMUTT	43
23	Jerk-based High Complex Chaotic Generator with Modified Rectangular and Signum Functions Khunanon Karawanich, and Pipat Prommee/ KMITL	45
24	The Computerized Test for Screening Dementia in the Elderly: Pilot Study Warissara Limpornchitwilai, Chatchai Paengkumhag, Boonserm Kaewkamnerdpong, and Kosin Chamnongthai/ KMUTT	47
25	Effects of the tablet-based gaming app to promote personal help and social skills in student with autism Chatchai Paengkumhag, M.Ed., Warissara Limpornchitwilai, M.Eng., Kosin Chamnongthai, Ph.D., and Boonserm Keawkamnerdpong, Ph.D./ KMUTT	49
26	Application for Analyzing Data Transmission Path on Communication Network Using Optical Character Recognition Pattara Kladkaew, Werapon Chiracharit/ KMUTT	51

27	A Development of LVDT Demodulator Circuit Based on FPAA chip Krit Angkeaw, Preechar Thongdit, and Surachai Chanchay/ KMUTNB	53
28	A Study on Programming Control for Sorting Robots Narissara Thoonthaisong, Tanaporn Payommai, Somsin Wangkhuntod/ RMUTI and Kosin Chamnongthai/ KMUTT	56
29	A Resistorless Temperature-insensitive Electronicallyadjustable Single VDGA-based Voltage-mode Instrumentation Amplifier Montree Siripruchyanun, Burin Theppota, and Wiset Saksiri/ KMUTNB	58
30	Title of Abstract: Classification of COVID-19 severity based on self- reported symptoms through the Home- Isolation platform Sriengchhun Chheang, Wiroom Sriborrix, and Krisana Chinnasarn/ BUU	60
31	Semantic Scene Understanding in Fast Camera Motion Using Spatial and Local-Global Temporal Feature Fusion Dipanita Chakraborty, Werapon Chiracharit, and Kosin Chamnongthai/ KMUTT	62
32	A Phase-Locked-Loop Algorithm Enhancement for Off-Board EV Charger Based on a Three-Level NPC Converter Under Non-Ideal Three-Phase Grid Voltages Thidarat Thanakam and Yuttana Kumsuwan/ CMU	64
33	Towards Eye Gaze Gesture Passwords Recognition Zakariyya Abdullahi Bature, Kosin Chamnongthai and Sunusi Bala Abdullahi/ KMUTT	66
34	IDF-Sign: Addressing Inconsistent Depth Features for Dynamic Sign Words Recognition Sunusi Bala Abdullahi and Kosin Chamnongthai/ KMUTT	68
35	Efficient PDM-to-PCM Converter Rithea Sum, Chanon Khongprasongsiri, Watcharapan Suwansantisuk, and Pinit Kumhom/ KMUTT	71

Advantages and challenges of Cell-free systems



Ass. prof. Pham Thanh Hiep

Le Quy Don Technical University, Ha Noi, Viet Nam

Abstracts: Fifth-generation (5G) mobile communication technology has been developed and now widely installing in many countries, with millions of 5G customers. Therefore, it's time for us to focus on the next generation and its key technologies. As an evolution from conventional BS-centric networking, user-centric cell-free networks has been considered as one of the most promising candidates for beyond 5G technologie. The cell-free system has recently been investigated as a way to achieve uniform communication performance over the beyond 5G cellular system. The cell-free model can be combined with another technology, such as antenna design, system architecture, signal processing and so on, for improving the specific quality of service requirements of users. This work carry out an overview of cell-free model, including motivations, use case scenarios, requirements, supported technologies. The cell-free model is applied in several systems to confirm its high efficiency comparing with small-cell model. However, deploying cell-free systems is a challenging task.

Trends and Challenges of AI Accelerator Design



Trio Adiono

The School of Electrical Engineering and Informatics of Institut Teknologi Bandung (ITB)

Abstracts: The application of AI is currently growing very rapidly. With the development of these various applications, the density and computational complexity of AI are very high. On the other hand, the need for devices with low power consumption and small dimensions is a challenge in implementing AI algorithms. Therefore, it is necessary to design a VLSI architecture specifically for the AI application. Application design must take advantage of various special characteristics of AI algorithms, such as data reuse and data independence. Here will be presented several techniques to improve the performance of the AI accelerator. Some AI accelerator performance parameters will also be presented.

Neuron Function with Single Device by PN-Body Tied SOI-FET and Activity on Cryo-CMOS for Quantum Computing



Prof. Jiro Ida

EE Department, Kanazawa Institute of Technology (K.I.T.), Ishikawa, Japan

Abstracts: Performance improvement on computing continues on evolution by scaling of CMOS and is also expected to be accelerated by AI technology and quantum computing. I review current status of AI research and also show motivation on next AI technology which is Bio-inspired or neuromorphic. We started applying our newly proposed steep slope device “PN-Body Tied SOI-FET(PNBT)” for morphing neuron function. We confirmed that PNBT has LIF(leaky integrate and fire) function, which is the simple and useful model of the neuron in the never cell. My laboratory has also involved in one of the big quantum computing research-program in Japan, recently. I show the short review on quantum computing and also shows motivation of Cryo-CMOS for quantum computing. I will show our data of 200nm SOI MOSFET at 3K. The new phenomena still observed on Cryo-CMOS, such as freeze-out related issues, oscillation of current. It indicates that more study on Cryo-CMOS is necessary for proper Cryo circuit design.

Computer Design Classes Using Open-source RISC-V: Linux Bootable SoC on FPGA and VLSI Implementations



Hoang Trong Thuc

University of Electro-Communications (UEC), Tokyo, Japan

Email: hoangtt@uec.ac.jp

Abstracts: From the beginning of the 21st century, the Reduced Instruction Set Computer (RISC) architecture was already dominant in both the Personal Computer (PC) and mobile marketplace due to its low-cost characteristics. Recently, an open-source Instruction Set Architecture (ISA) named RISC-V emerged. It was first presented by the Berkeley architecture group in 2014 and is now maintained by the RISC-V Foundation. The development of RISC-V was turning the silicon industry more efficient than ever. Up to now, plenty of RISC-V processors and related products have been presented in academic and industrial forums. Among the rich development tools of the RISC-V ecosystem is the novel idea of using Scala language with the Chisel library to generate a Verilog code. The generated Verilog can be easily used for Field-Programmable Gate Array (FPGA) and Very Large Scale Integrated circuit (VLSI) implementations. This approach created a new playground for developers to share and reuse each other designs with virtually no effort. With RISC-V and Chisel, a group of 3 to 5 graduate students can design and implement a complete computer system within a semester, a task usually costing Intel a team of a hundred employees within two years. Therefore, this talk aims to present a series of classes with RISC-V. At the end of the classes, the participants can customize their own Linux-bootable computer system implemented on both FPGA and chip.

Quality over quantity: An introduction to feature selection



Prof. Veronica Bolon-Canedo

Computer Science and Information Technologies of the University of A Coruna

Abstracts: Feature selection has been widely used as a preprocessing step that reduces the dimensions of a problem and improves classification accuracy. The need for this kind of technique has increased dramatically in recent years in order to cope with scenarios characterized by both a high number of input features and/or of samples. In other words, the big data explosion now has the added problem of big dimensionality. In this talk we discuss the importance of feature selection and outline some of its applications to real problems.

A Slanted-Edge Method for High-Accuracy Measurement of Modulation Transfer Function

Miu Fujita* and Kazuki Nishi

The University of Electro-Communications, 1-5-1, Chofugaoka, Chofu-shi, Tokyo 182-8585, Japan

*f2231130@edu.cc.uec.ac.jp

1. Introduction

The Modulation Transfer Function (MTF) is an index used to specify the image resolution of digital cameras as the spatial frequency response. The resolution of digital cameras has been improved year by year. The slanted-edge method specified in ISO Standard 12233[1] is one of the methods for measuring the MTF and has widely been used for evaluating the consumer camera products. However, the averaging procedure of image pixels that is embedded in this method causes some errors in the MTF estimation. In this paper, an improved slanted-edge method is proposed and compared with the conventional method through numerical simulations.

2. Slanted-edge method and its improvement

2.1. Principle of slanted-edge method

The MTF is gained by calculating degree of edge blurring from a slanted-edge image. The slanted-edge method specified in ISO Standard 12233 has four main processes. First, pixel data are gathered to an axis perpendicular to the edge along the edge from shoot edge-slanted images. Next, each pixel is divided on the axis (divided pixel is called sub-pixel) and sum of pixel values in sub-pixel are averaged to gain finer and equally spaced pixel values and obtain the ESF (Edge Spread Function). This averaging process is called the binning. Then, the LSF (Line Spread Function) is calculated by differentiating the obtained the ESF. Finally, the MTF (Modulation Transfer Function) is gained by Discrete Fourier Transform of the LSF.

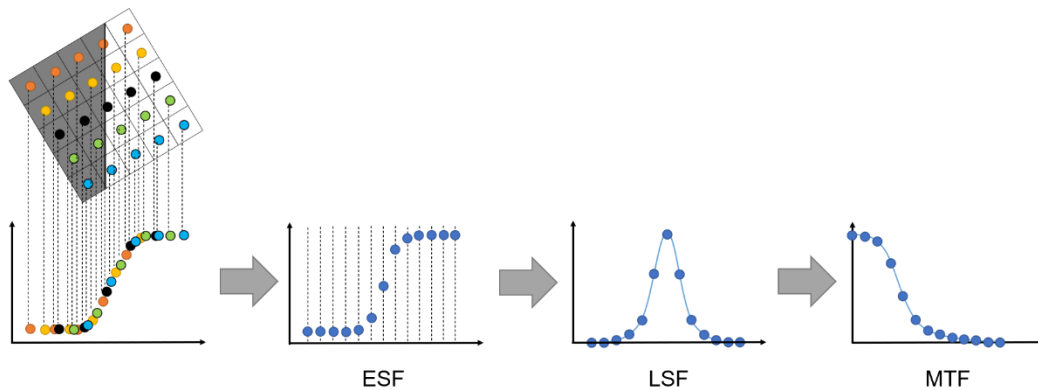


Fig.1: Computation procedure based on slanted-edge method

2.2. Problem of binning process

The data projected from each row of images are unequally spaced. Therefore, the binning is used for rearranging the data equally. It is a process of dividing a pixel into equally spaced segments and averaging the data within each segment. Each segment is called a sub-pixel bin. The binning allows data to be equally spaced, and to obtain a high-density ESF.

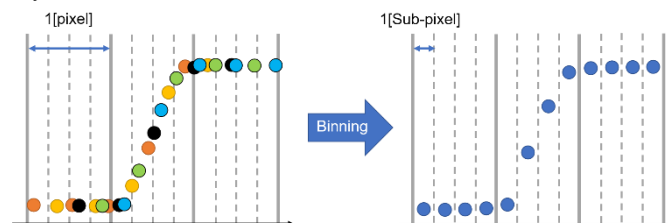


Fig.2: Binning process

However, the averaging process of unequally spaced data in each sub-pixel bin causes instability in the MTF estimation. Thus, the improvement of the binning process is necessary for the high-accuracy measurement.

3. Improved method

We propose one of the improvements of the conventional slanted-edge method. Assuming that the same number and equally spaced data is in each sub-pixel bin equally, the averaging process based on our proposed method is more stable and accurate than the original method.

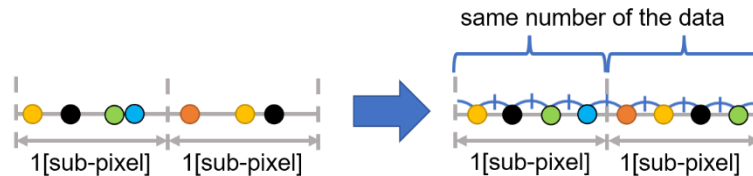


Fig.3: Improvement of binning process. It is valid for the case that many pixel data are included in each bin.

The correction formula is added to the conventional slanted-edge method. After that, slanted-edge images with 2 kinds of blur are created by using a PC; one is with a gaussian blur and another is with a circular blur. These images are fixed in width and varied only in height. Then, the MTF is estimated with and without the correction formula and other two software programs. Finally, the differences between each estimate and the theoretical value are calculated and compared.

4. Simulation results

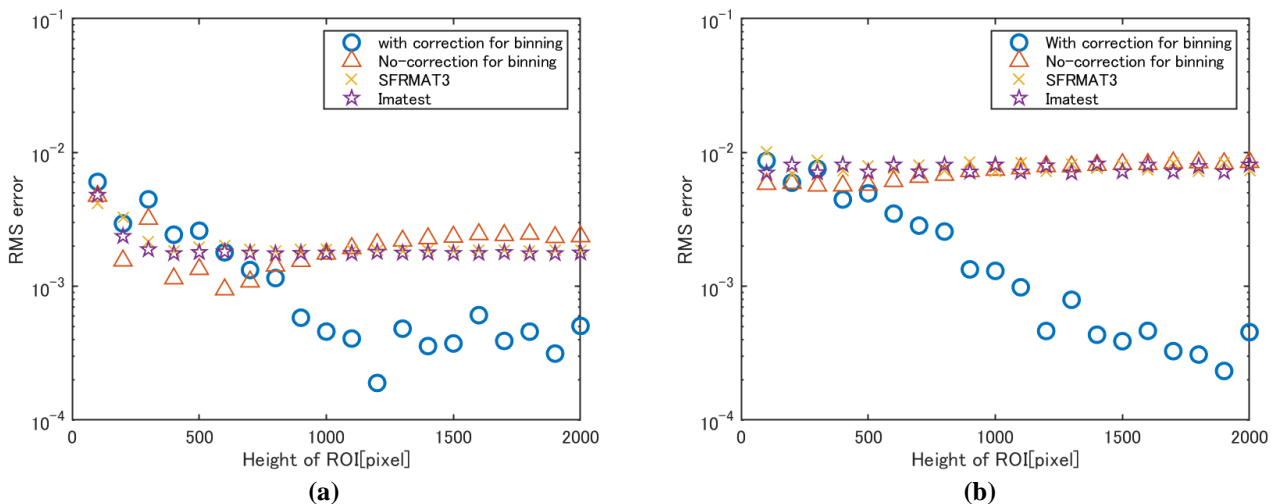


Fig.4: Effects of height of ROI on the MTF estimation accuracy. The binning division is 4. (a) Gaussian blur. (b) Circular blur.

The MTF estimates of four methods, the corrected method, the conventional method, and other two software are shown in Fig.4. There is any difference among all methods when the height of the images is small. Although, as the height increases, the error of the corrected method is decreased. It is because the larger the height is, the more evenly the data is in each sub-pixel bin. Also, the errors do not increase more and remained constant by the effect of the aliasing in the high spatial frequency area when the height increases sufficiently.

5. Conclusion

We proposed a correction of the binning process embedded in the slanted-edge method and verified the effectiveness through numerical simulations. It was shown that the proposed correction makes it possible to provide a high-accuracy estimate of the MTF when the height of image is comparatively large.

REFERENCES

1. "Photography--Electronic still picture imaging--Resolution and spatial frequency responses." ISO 12233:2017(E).

Real-Time Vital Sign Monitoring using 24 GHz Radar

Hoang Thi Yen and Guanghao Sun
 Graduate School of Informatics and Engineering,
 The University of Electro-Communications, Tokyo, Japan
 Email: yen@secure.ee.uec.ac.jp and guanghao.sun@ieee.org

1. Abstract

Owing to the Covid-19 epidemic, medical radar has become a potential non-contact method in patient monitoring. However, the medical radar is sensitive to external interference. The output signal obtained by the radar when a patient makes random body movements can significantly reduce the accuracy of vital sign detection algorithms. In this study, we present a real-time model of the 24-GHz radar signal quality classification system and a technique to enhance the resolution of respiration (RR) and heart rate (HR) extraction. The signal quality classification was evaluated on the measured signals of 10 healthy subjects. Accordingly, the obtained results indicate that with specific features, the accuracy of signal quality classification reaches 89.8%–100% while real-time RR and HR extraction results demonstrate significant agreement between radar measurement and the contact-type sensor.

2. Introduction

With the sustained increase in Covid-19 cases, the trend of employing non-contact devices to monitor patients' signal has become beneficial and necessary. The 24-GHz radar has garnered considerable interest and is studied for its application in monitoring vital signs including respiration rate (RR), heart rate (HR) [1-3] and heart rate variability (HRV) [4,5]. However, the radar signal is significantly susceptible to body random movements or the approaching motion of a doctor or nurse to the patient's bed. These noises reduce the accuracies of RR and HR extraction algorithms [6]. Therefore, prior to detecting RR and HR, it is necessary to discard low-quality signal intervals. Previous studies have also developed signal quality classification models [7]. However, these studies extracted data from the internet or adopted radars other than the 24-GHz radar. In the scope of our survey, there are no papers presenting signal quality classification in real time. In this study, we develop a system that runs in real time towards practical applications to solve these problems.

3. Method

The classification of radar signal quality and vital sign detection are conducted in actual time. The training signal was performed with some models, the quadratic-support vector machine (SVM) obtained highest validation accuracy; accordingly, we selected quadratic-SVM as the model in this paper. The features were extracted for input of classification model as description below.

- Feature 1 The smaller of two amplitudes of the I and Q channels
- Feature 2 The higher of two amplitudes of the I and Q channels
- Feature 3 The oscillation of the arctangent
- Feature 4 The smaller of two center frequencies of I and Q channels
- Feature 5 The larger of two center frequencies of I and Q channels

To detect RR and HR, we employ a [0.1-0.6] bandpass filter (BPF) and a [0.7–3.0] BPF combined with the technique of determining peak-to-peak distance in time domain. On LabVIEW, we design a real-time system including data acquisition, signal quality classification, and RR and HR extraction to display vital sign results, the system can be shown as Figure 1.

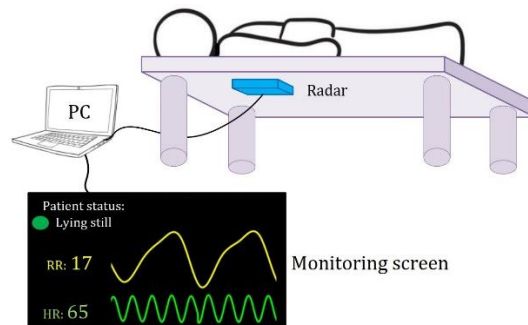


Fig.1: Overview of real-time monitoring system

4. Results

We measured the signals of 10 healthy subjects in the laboratory. The measurements were taken while the subjects were lying on the beds of the laboratory, and a 24-GHz radar was equipped beneath their beds. Each student took the measurement for 10 min, during this time, the subjects were asked to make movements while lying in bed. The random body motion generation was controlled and labeled. The signal quality classification results were obtained at 89.8–100%, as Table 1.

Table 1. Test results for signal quality classification of 10 healthy subjects

Subject	Proposed method		Number of wrong decisions	Accuracy (%)
	Number of high-quality samples	Number of low-quality samples		
Subject 1	48	11	1	98.3
Subject 2	51	8	0	100
Subject 3	33	26	6	89.8
Subject 4	44	15	1	98.3
Subject 5	39	20	5	91.5
Subject 6	52	7	1	98.3
Subject 7	48	11	0	100
Subject 8	54	5	2	96.6
Subject 9	54	5	1	98.3
Subject 10	45	14	2	96.6

After the signals are classified into high- and low-quality signal groups, the high-quality signal segments are sent to the next block to detect HR and RR. The results showed that the mean bias values of RR and HR are -0.14 and -0.18 bpm, respectively, while the $1.96 \times SD$ (95% limits of agreement) values of RR and HR are 2.53 and 6.62 bpm, respectively, as Figure 2.

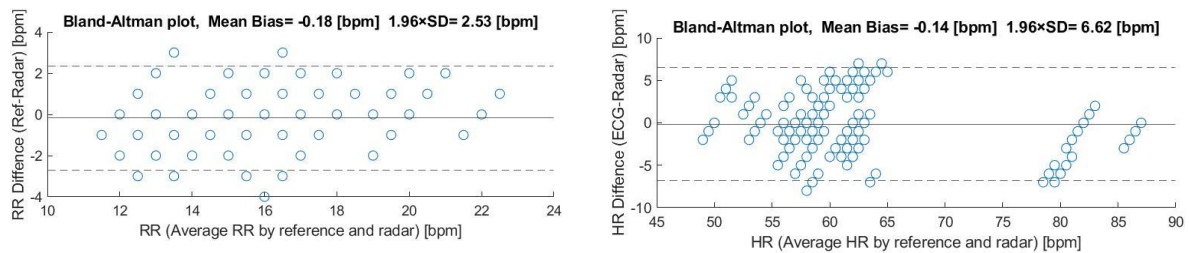


Fig.2: Bland-Altman plot of RR and HR present the agreement between real-time radar measurement and contact-type sensor

References

- [1] Y. Xu, et al. "Accurate and contactless vital sign detection in short time window with 24 GHz doppler radar," *Journal of Sensors*, vol. 2021, 2021.
- [2] G. Sun, et al. "Twenty-four-hour continuous and remote monitoring of respiratory rate using a medical radar system for the early detection of pneumonia in symptomatic elderly bedridden hospitalized patients," *Clinical case reports*, vol. 7, no. 1, p. 83, 2019.
- [3] H. T. Yen, et al. "A medical radar system for non-contact vital sign monitoring and clinical performance evaluation in hospitalized older patients," in *Biomedical Signal Processing and Control* (2022).
- [4] P. L. Vladimir, et al. "High-accuracy real-time monitoring of heart rate variability using 24 GHz continuous-wave Doppler radar." *IEEE Access* 7, pp. 74721–74733, 2019.
- [5] G. Sun, et al. "Non-contact monitoring of heart rate variability using medical radar for the evaluation of dynamic changes in autonomic nervous activity during a head-up tilt test." *Journal of Medical Engineering & Technology*, vol 43.7, pp. 411–417, 2019.
- [6] K. Sun, et al. "Validation of noncontact cardiorespiratory monitoring using impulse-radio ultra-wideband radar against nocturnal polysomnography." *Sleep and Breathing*, vol 24.3, 841–848, 2020.
- [7] H. Tang, et al. "Automated signal quality assessment for heart sound signal by novel features and evaluation in open public datasets," *BioMed Research International*, vol. 2021, 2021.

Analysis of Connection Characteristics between Random Sections and Patternized Groups in No-lane Heterogeneous Traffic

Akihito Nagahama¹, Kenji Tanaka¹, and Katsuhiko Nishinari²

¹ Graduate School of Informatics and Engineering, The University of Electro-communications

² Research Center for Advanced Science and Technology, The University of Tokyo

naga0862@uec.ac.jp, tanaka@is.uec.ac.jp, tknishi@mail.ecc.u-tokyo.ac.jp

Abstract

In many Asian countries, one can observe heterogeneous traffic with low lane discipline. Previous research clarified that the vehicle order of various types of vehicles affects traffic characteristics, and such order has a specific pattern. However, the relation between such patterns and other random sections has yet to be investigated. Through the graph-based investigation, we clarified that they often have small numbers of relations, e.g., one edge on the graph, and the patternized groups in the traffic relatively stack random sections.

Introduction

The widespread of automobiles is accelerating the global economy in the 21st century while our daily convenience and liberalization of traveling are also enhanced by automobiles. On the other hand, the increase in the number of automobiles causes traffic congestion. It is becoming a fundamental problem in many Asian countries. One of the features of traffic in such countries is that road traffic consists of various types of vehicles, e.g., motorcycles, three-wheelers, and passenger cars. Besides, lane discipline is poor in such traffic. In this study, such traffic is referred to as no-lane heterogeneous traffic.

Previous studies showed that behavioral differences between these types of vehicles affect the macroscopic properties of heterogeneous traffic. For example, heterogeneous traffic would exhibit different traffic flow according to the arrangement or order of vehicles. Here the order is defined as the sequence of vehicle types in a chain (i.e., platoon) of vehicles in a leader-follower relationship¹). However, such an order of the platoon cannot be defined in no-lane traffic because the leader-follower relationship is not a chain-like shape but is complicatedly connected.

In order to replicate the multiple leader-follower relationships for a vehicle, we proposed to assume the heterogeneous no-lane traffic as a network of these relationships, as shown in Fig. 1²). In²), we found the distribution of the relations between each type of vehicle did not follow the random process but had a certain bias. The analyzed data were based on a video observation conducted in Mumbai, India, in January 2017. For example, motorcycles and auto-rickshaws less frequently had relationships than statistically estimated.

Based on this result, we also explored whether there are vehicle groups comprising arbitrary types of vehicles³). Applying a graph mining technique⁴), we successfully obtained the groups (or sub-networks) comprising even several types of vehicles. Table 1 shows the most prominent groups from the observed numbers and time duration perspectives. In Table 1, m, r, c, and h represent motorcycles, auto-rickshaws, normal passenger cars, and heavy vehicles, respectively. The result of this research implies that when one observes no-lane heterogeneous traffic, as shown in Fig. 2, one can divide it into groups apparently often observed and other remaining vehicles, i.e., sections. Here, because the network of leader-follower relationship is the extended concept of order of such relations, the network features, including random sections and groups, should be replicated in traffic simulation. Otherwise, the accurate traffic characteristics cannot be reproduced in the simulator.

Result and Conclusion

We have already distinguished groups frequently observed and other random sections in³). Therefore, we need to clarify the features of connections between these groups and random sections, which are depicted in red arrows in Fig. 2. In this research, focusing on relations entering from the groups to the random sections (in-edges) and leaving from the random sections to groups (out-edges), we analyze the distributions of these relations, i.e., in/out degrees.

The obtained distributions are shown in Fig. 3. The left figure shows the number of in-edges, i.e., in-degree to the random sections, and the right one shows the out-degree from the random sections. Firstly, we concluded that most random sections had no relation to the groups because the most prominent frequency was located at zero in both cases of /out-degrees. Besides, the random sections would often be followed by the groups because the number of in-degrees more than zero is larger than that of out-degree. This result implied that the groups are stuck by the random sections from the traffic flow perspective.

Reference

- 1) Liu, L., et al. : "Modeling and simulation of the car-truck heterogeneous traffic flow based on a nonlinear car-following mode." *Applied Mathematics and Computation*, Vol. 273, 706–717 (2016)
- 2) Nagahama, A., et al. : "Detection of leader–follower combinations frequently observed in mixed traffic with weak lane-discipline." *Physica A: Statistical Mechanics and its Applications*, Vol. 570, No. 15, 125789 (2021)
- 3) Nagahama, A., et al. : "Certain Types of Vehicles in Heterogeneous Traffic in India Tend to Gather." *Journal of the Eastern Asia Society for Transportation Studies*, Vol. 14, 1794–1813. (2021)
- 4) Nguyen, P. C., et al. : " CI-GBI: A novel approach for extracting typical patterns from graph-structured data." *Proceedings of the 9th Pacific-Asia conference on Advances in Knowledge Discovery and Data Mining*, Vol. 14, 639–649. (2005)

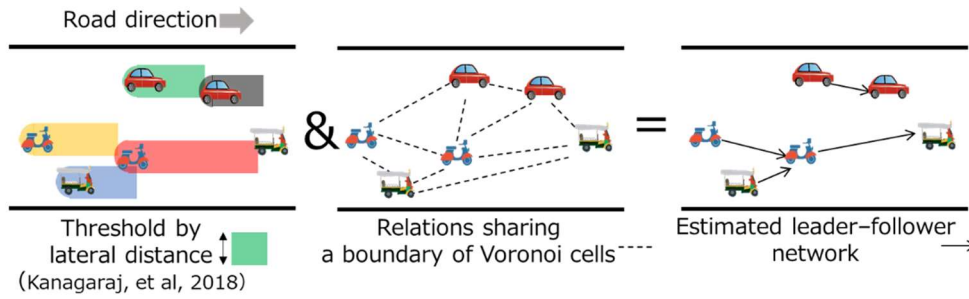


Fig.1: Image of estimation of leader-follower network



Fig.2: Image of division of groups and remaining random sections

Sub-network	λ_i^0 (/10 ⁸ frames)	$\Delta\lambda_i^{norm}$
	3.72×10^6	33.63
	1.38×10^6	12.04
	2.30×10^6	11.88
	3.70×10^6	7.58
	1.68×10^6	6.89
	7.61×10^5	6.15
	6.32×10^6	6.02
	1.49×10^6	5.91
	1.79×10^7	3.54
	7.24×10^6	3.45

Tab.1: The most prominent groups (subnetworks) detected in ³⁾

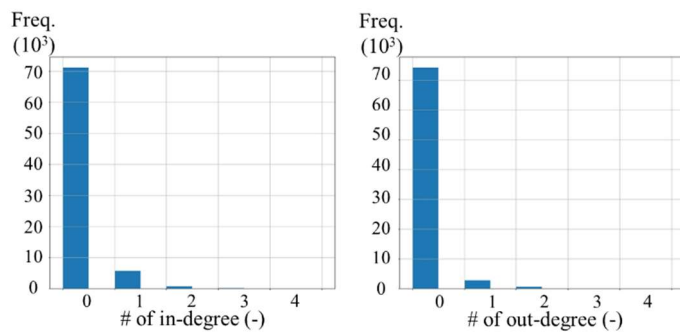


Fig.3: The distributions of frequency of in/out-degrees from random sections

Information presentation aiming intention share in ADAS

Yumeno Hatori¹, Akihito Nagahama¹, and Kenji Tanaka¹

¹ Graduate School of Informatics and Engineering, The University of Electro-communications

yball8@gmail.com, naga0862@uec.ac.jp, tanaka@is.uec.ac.jp

Abstract

When using automated systems including advanced driver-assistance systems (ADAS), it is essential to prevent mistrust to maintain the appropriate trust to enhance safety. However, distrust is particularly likely to occur when there is a discrepancy in intentions between drivers and systems. Through the investigation, additional information sharing the system intention as well as communication interface between drivers and the system enhanced trust on the ADAS using the tactile feedback.

Introduction

Advanced driver-assistance systems (ADAS) have been widely used in the market. In this context, shared control has been proposed to compensate for the disadvantages of manual driving and ADAS. Shared control has the advantage that the driver and the ADAS can share their intentions and methods using the sense of touch, for example, have been proposed¹). In general, when using automated systems, it is essential to prevent mistrust and overconfidence to enhance safety. However, because shared control enhances shared intentions, it is thought that distrust is particularly likely to occur when there is a discrepancy in intentions. Therefore, measures to prevent such a discrepancy are necessary. In addition, it has been shown that tactile feedback (FB) from the steering wheel alone is insufficient for understanding the intent of the system²). The purpose of this study is to investigate and propose a method of presenting additional information necessary for drivers to have appropriate trust in a shared control system using tactile FB. We especially consider false alarms when distrust is likely to occur.

Effect of additional information

We clarify how the additional information on a display about the location of objects that the system perceives as dangerous (dangerous objects) affects the driver's trust in the system and his/her understanding of the system's intentions when the tactile FB is activated. As shown in the left figure of Fig. 1, the evaluation event used in the analysis was an event in which the subjects overtook a parked vehicle while a vehicle approached from the right rear. In the event, the driver is assumed to change lanes, while the system judges the vehicle behind to be dangerous and generates a reaction force (tactile FB) on the steering wheel. As the experimental stimulus, we used a driving simulator (DS) shown in the right figure of Fig. 1. We observed the subjective trust in the system, etc., under the conditions with and without the presentation of the additional information. Three scenarios were prepared. In scenario A, the system correctly alarms the dangerous object, and drivers can recognize it. In scenario B, the system correctly alarms the dangerous object, but drivers cannot recognize it. In scenario C, the system falsely alarms the object, and the driver can recognize it.

The left figure of Fig. 2 shows the change in understanding of the system intent. The percentage of subjects correctly understood the intention increased by 20 % in Scenario A and 15 % in Scenario B. However, the percentage in Scenario B was 30 % even with the presentation, which is lower than in Scenarios A and C. Therefore, we can conclude that the additional information about the dangerous object increased the percentage of people who understood the system's intention. Besides, it can be supposed that the additional information was inadequate for invisible hazards. However, there was a tendency for the participants to understand the system's intention when the dangerous object was presented. On the other hand, the percentage of people who correctly understood the system's intentions decreased by 13 % in Scenario C. This is because the system's intentions were not accurately presented. This may be due to driver confusion caused by the incorrect presentation of the dangerous object. Besides, in Scenario B, the trust of all six participants increased, as shown in the right figure of Fig. 2. The presentation of the dangerous object made subjects aware of unseen hazards and increased their trust.

Distrust avoidance by communication with system

In the first experiment, especially in Scenario C, we expected to prevent a loss of trust in false alarms by presenting the additional information; the results did not follow the expectation, though. Previous studies on conversational systems have reported that increased communication with systems contributes to increased trust. Therefore, in the second experiment, we examined the effect on driver trust by introducing a "false alarm button" that enables the driver to inform the system when the system incorrectly recognizes a dangerous object. By pressing the button and getting a response from the system, the drivers can communicate with the system. Besides, we prepared four scenarios from a to d. Scenario a is the control scenario where there is no button to communicate.

In scenario b, the driver can press the button, but there is no response from the system. In scenario c and d, the system responds by voice but the system output a longer response in scenario d than in c.

In Fig. 3, the differences between scenarios b, c, and d were calculated for trust in the system, acceptance of the system, and communication feelings, using scenario a with no false alarm button as the control data. Trust was highest for scenario b, suggesting that the false alarm button improves trust under false alarms. Acceptability was also highest in Scenario b. This indicates that the false alarm button increases acceptability. On the other hand, the results of scenarios c and d were the same as those of scenario a. In free descriptions and questionnaires, some subjects answered that the audio was too long. Although the introduction of buttons tended to increase trust and acceptability, the addition of voice did not further improve acceptability, suggesting that the user may feel annoyed by the long voice and that acceptability and trust may decrease.

Conclusion

Through the investigation, additional information sharing the system intention enhanced trust on the ADAS using the tactile feedback. However, because trust on the system was not sufficient under the condition with invisible danger, we proposed communication interface between drivers and the system. The results showed that relatively simple interface, i.e., false alarm button, can enhance the trust on the system.

Reference

- 1) Steele, Micah, and R. Brent Gillespie : "Shared control be-tween human and machine: Using a haptic steering wheel to aid in land vehicle guidance." Proceedings of the human factors and ergonomics society annual meeting, Vol. 45, No. 23, 1671–1875 (2001)
- 2) Johns, Mishel, et al : "Exploring shared control in automated driving." 2016 11th ACM/IEEE International Conference on Human-Robot Interaction, (2016)

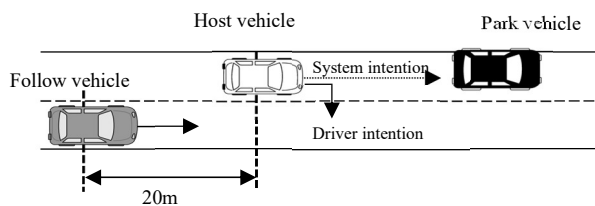


Fig.1: The left figure shows the experimental situation. The right figure shows the utilized driving simulator.

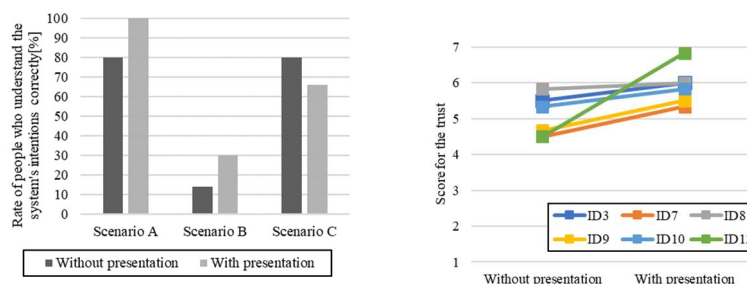


Fig. 2: The results of the first experiment; the left figure shows the rate of subjects who understand the system’s intention correctly, and right figure shows the scores for the trust in Scenario B.

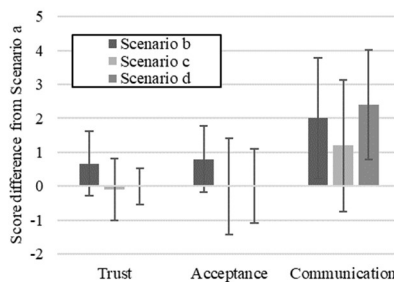


Fig. 3: The results of the second experiment.

A Note on Correlation-Based Watermarking Scheme for Auto-RDS Images using 2-D Orthogonal Transforms

Shun KITAKAZE and Hiromu KODA

Graduate School of Informatics and Engineering, The University of Electro-Communications

k2231035@edu.cc.uec.ac.jp

ABSTRACT

In this paper, we investigate the basic performance of digital watermarking scheme for auto-RDS (random dot stereogram) images. First, we describe the feature of auto-RDS images briefly. Next, we propose a correlation-based watermarking scheme for auto-RDS images using 2-D orthogonal transforms (DCT, LOT (lapped orthogonal transform)), and explain the procedures of embedding and detecting watermarks for proposed scheme. Finally, experimental results for test images show that the characteristic of BER (bit error rate) for the LOT is superior to that of BER for the DCT.

Keywords: Auto-RDS images, Digital watermarking, Orthogonal transforms.

1. INTRODUCTION

Digital watermarking is used for copy protection and copyright protection purposes [1]. Its techniques can complement encryption by embedding a secret imperceptible signal (i.e., a watermark) into host data (speech, image, etc.) [1]. In previous study [2], RDS (random dot stereogram) [3] was used as the watermark information of digital watermarking scheme, where the size of host images was 256^2 pixels (pels).

In this paper, we investigate the basic performance of digital watermarking scheme for auto-RDS images. First, we describe the feature of auto-RDS images briefly. Next, we propose a correlation-based watermarking scheme for auto-RDS images using 2-D orthogonal transforms (DCT [5], LOT (lapped orthogonal transform)[6]), and explain the procedures of embedding and detecting watermarks for proposed scheme. Finally, experimental results for test images (512^2 [pels]) show that the characteristic of BER (bit error rate) for the LOT is superior to that of BER for the DCT.

2. FEATURE OF AUTO-RDS IMAGES

Auto-RDS image (Fig. 1) consists of spatially repetitive patterns, and it is the stereogram that enables one image to be viewed three-dimensionally according to the disparity between both eyes [4].



Fig. 1: An example of auto-RDS image for the perception pattern “T” shown in Fig. 2, where “•” indicates the reference point for both eyes.



Fig. 2: Perception pattern “T”.

3. 2-D ORTHOGONAL TRANSFORMS

Let X be $N \times N$ input image matrix, Y be $N \times N$ transformed output matrix, and A be DCT basis matrix. Then the transform formula for 2-D DCT is expressed as follows [5].

$$\bullet \text{ Forward transform: } Y = AXA^T \quad (1)$$

$$\bullet \text{ Inverse transform: } X = A^T YA \quad (2)$$

Here A^T is the transpose of matrix A .

Next, let X' be $2N \times 2N$ input image matrix, Y be $N \times N$ transformed output matrix, and P^T be the transpose of LOT basis matrix. Then the transform formula for 2-D LOT is expressed as follows [6].

$$\bullet \text{ Forward transform: } Y = P^T X' P \quad (3)$$

$$\bullet \text{ Inverse transform: } X' = P Y P^T \quad (4)$$

4. BASIC PROCEDURES OF EMBEDDING AND DETECTING WATERMARKS

Figures 3 and 4 show the procedures of embedding and detecting watermarks for proposed scheme, respectively. Here the basic algorithm of [2] is used. “#2” of Fig.3 denotes the right half of auto-RDS image, while “#2’ ” of Fig. 4 denotes the detected watermarks.

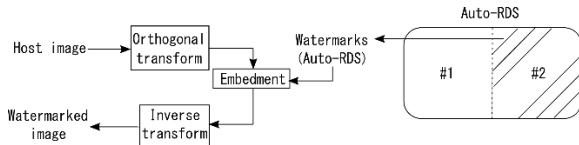


Fig. 3: The procedure of embedding watermarks for proposed scheme, where the basic algorithm of [2] is used.

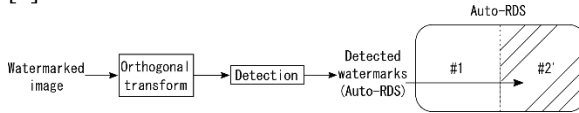


Fig. 4: The procedure of detecting watermarks for proposed scheme, where the basic algorithm of [2] is used.

5. COMPUTER EXPERIMENTS

5.1. Experimental Conditions

We conduct the computer experiments using the following conditions.

- Test images: “ELAINE”, “MILKDROP” (512² [pels], 256 levels).
- M'-sequence: the 8th order ($m=8$), length $L=256$.
- Method of orthogonal transform in Figs. 3 and 4:
 - (1) DCT method (output size $N \times N=8 \times 8$).
 - (2) LOT method (output size $N \times N=8 \times 8$).
- Watermark information: the right half (32×40 [pels], 2 levels) of Auto-RDS image, i.e., 1280 bits.
- Parameters for watermarks:
 - (s [=start position], l [=bit length]) = (12, 11).
- Image quality measure: $SNR=10\log_{10}(255^2/MSE)$, where MSE is the mean square error between an original host image and a watermarked image.

5.2. Results and Considerations

Figure 5 shows BER vs. SNR, where vertical and horizontal axes indicate BER of detected watermarks and SNR of watermarked image, respectively. Figures 6 and 7 show examples of watermarked images (SNR = 40[dB]) and error images for Fig. 6, respectively. From Fig.5, it is found that the max values of SNR such that BER = 0[%] are about 43[dB] and 46[dB] (> 40[dB]) for DCT and LOT, respectively. Therefore, the characteristic of BER for the LOT is superior to that of BER for the DCT.

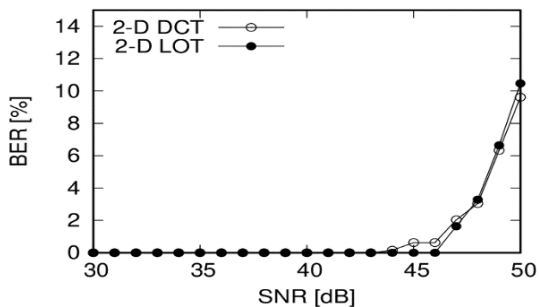


Fig. 5: BER vs. SNR (“ELAINE”, 512² [pels]).

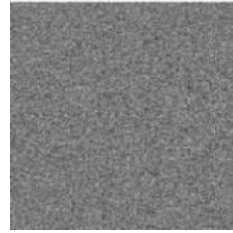


(a) DCT method.

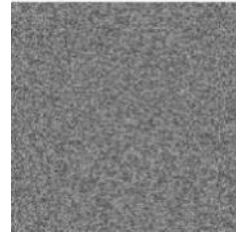


(b) LOT method.

Fig. 6: Examples of watermarked images (40[dB]).



(a) DCT method.



(b) LOT method.

Fig. 7: Examples of error images (×20) for Fig. 6.

From Figs. 6 and 7, it is found that the degradation of watermarked images (40[dB]) is not perceptible.

The BER of image “MILKDROP” was slightly similar to that of image “ELAINE”.

6. CONCLUSION

In this paper, we have investigated the basic performance of correlation-based watermarking scheme for auto-RDS images using 2-D orthogonal transforms (DCT, LOT). From experimental results for test images (512² [pels]), it has been found that the characteristic of BER for the LOT is superior to that of BER for the DCT.

Future work is to investigate the resistance of our scheme to fundamental attacks.

7. REFERENCES

- [1] A. Hanjalic, *et al.*: Image and databases, Elsevier, 2000.
- [2] H. Furuta and H. Koda: “A note on correlation-based scheme of digital watermarking for images embedding the half-RDS in DCT domain”, *Proc. of Image Media Processing Symposium (IMPS 2017)*, P-1-12, pp.44-45, 2017-11 (in Japanese).
- [3] B. Julesz: Foundations of cyclopean perception, *The MIT Press*, 2006.
- [4] I. P. Howard and B. J. Rogers: Binocular vision and stereopsis, *Oxford University Press*, 1995.
- [5] N. Ahmed, T. Natarajan and K. R. Rao: “Discrete cosine transform”, *IEEE Trans. on Comput.*, Vol.C-23, No.1, pp.90-93, Jan. 1974.
- [6] H. S. Malvar and D. H. Staelin: “The LOT: Transform coding without blocking effects”, *IEEE Trans. on ASSP*, Vol.37, No.4, pp.553-559, Apr. 1989.

A Review on Applications of Earth Observation Datasets in Ecological Vulnerability Assessment

Muhammad Kamran*, Kayoko Yamamoto

Joint Doctoral Program for Sustainability Research, Graduate School of Informatics and Engineering,
University of Electro-Communications, Tokyo, Japan

*muhammad.kamran@go.wt-jdpsr.jp,

Abstract

This paper presents a comprehensive review of the use of earth observation technology (with a focus on remote sensing datasets) in ecological vulnerability assessment research. The general trends and role of remote sensing datasets are discussed based on published literature. Recommendations are also furnished for future researchers.

Introduction

The interaction among natural, social, and economic systems builds the ‘ecological environment’ which is essential for human subsistence [1]. It is also referred to as ‘eco-environment’ in the literature. The increasing ecological vulnerability (EV) arising from unprecedented urbanization and economic growth is a global concern. This is recognized as a threat to sustainable development [2]. The ecological vulnerability assessment (EVA) is a scientific approach to determine the quality of the regional ecological environment. Conducting EVA requires various datasets belonging to natural, social and economic systems which are not easy to acquire through traditional means such as surveys [3]. However, the advancement of earth observation (EO) technologies such as satellite remote sensing (RS) has resulted in the availability of a multitude of datasets on various temporal and spatial resolutions. Consequently, the EVA research leveraging the use of RS datasets has increased rapidly in recent times. The main role of RS datasets in EVA research is for the development of a database of ‘indicators’ related to natural, social and economic systems (also called ecological vulnerability indicators (EVIs) [4].

There is an ever-increasing number of EVIs derived from RS datasets and reported in respective publications. However, a holistic understanding of the use of RS for EVA is missing from the literature. In response to this research gap, we conducted a comprehensive review of EVA-related literature with a focus on the usage of RS datasets.

The primary focus of this review is on expanding our understanding of the role of RS datasets in EVA research. This work has a potential to set the ground for future innovation in EVA regarding the selection of EVIs and study design. The progress in EVA research will help in meeting regional sustainable development targets.

Methodology

A total of 80 peer-reviewed journal publications were selected from Web of Science and Scopus using a combination of keywords that can grasp the concept of ‘EV’ and ‘RS’. The initial search resulted in approximately 1000 articles which were reduced to 640 after removing duplicates. In the next step, the titles and abstract screening resulted in the exclusion of a significant number of studies. The publications that presented results of integrated evaluation of EV using RS have been found using the terms ‘indicators’, ‘variables’, or ‘factors’ in their abstract because these terms refer to EVIs. Thus, to keep the workload manageable, Endnote 20.4.1 was used for filtering studies that do not use one of these words in their abstract. Finally, the remaining studies were screened manually for their title and abstract and a few more studies were rejected because of a mismatch with the scope of this review. Finally, 80 publications were included in the review.

The full-length screening of 80 selected publications resulted in the aggregation of 135 EVIs. These EVIs are interpreted with respect to the type of their data sources and presented in the results section.

Results

A trend analysis of the ‘publication year’ for the 80 selected publications shows a gradually increasing trend over the past two decades. A visible increase can be seen after 2015 (Figure 1 (a)). In addition, a look at journal titles revealed that 28.8% of articles are published in ‘Ecological Indicators’ which is an internationally reputed journal published by Elsevier. This implies that not only the quantity but also the quality of EVA research has also increased over time.

Figure 1 (b) is made by using the networkD3 package in R and it presents the collaboration between different countries. Moreover, the selected 80 publications are checked for their spatial and temporal nature of EV investigation and are classified into two broad categories. The first category is “spatiotemporal” which contains those studies in which the goal is to analyze ‘change’ in EV over time and space. 69 % of the studies belong to this category. The rest of the 31% of studies belong to the ‘non-temporal’ category because they only aim at investigating the spatial distribution of EV in the region under investigation at a certain time without exploring the change in EV conditions over several years or decades (Figure 2 (a)).

The interpretation of EVIs reveals interesting facts. The 135 EVIs were divided into five groups based on the type of their data sources. The groups are named as, RS, Non-RS, Digital Elevation Model (DEM), RS & Non-RS, RS - Non-RS - UAV — abbreviated as G1, G2, G3, G4, and G5 respectively. Figure 2 (b) presents the number

of EVIs in each group. The total number of EVIs that can be derived from RS data (G1+G4) and Non-RS data (G2+G4) are 52 and 102 respectively. A sample of 14 EVIs and their data source are presented in Table 1.

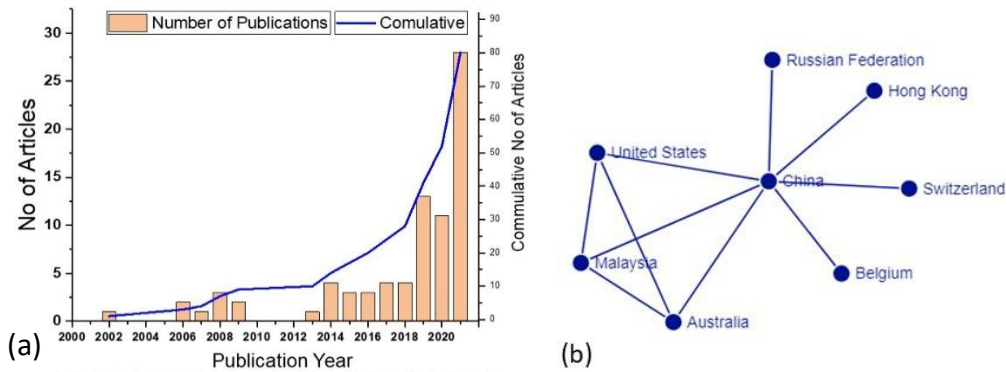


Fig.1: (a) Histogram showing the trend of publications, (b) Network diagram of collaboration among countries

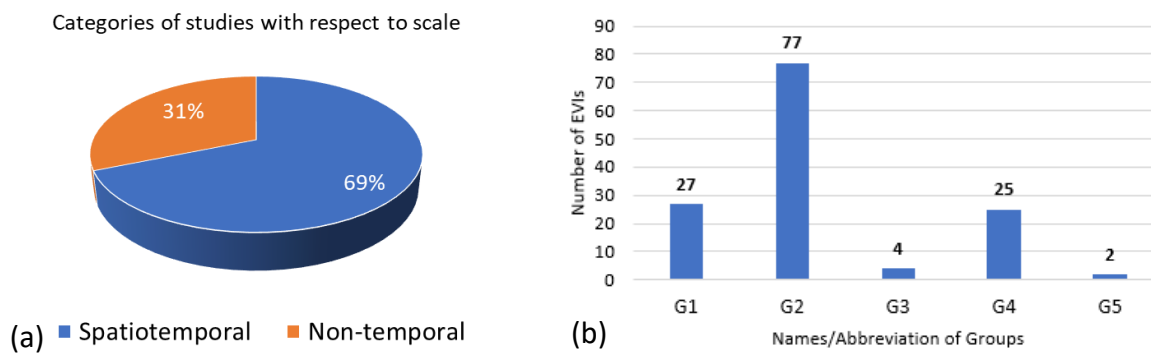


Fig. 2: (a) Categories of EVA studies concerning their scale, (b) Number of EVIs in each group with respect to their data source

Indicator Name	Source	Indicator Name	Source
Temperature	◆, ☒	Land Surface Moisture	◆, ☒
Normalized Difference Vegetation Index	◆	Vegetation Cover	◆, ☒
Land Use Land Cover	◆, ☒	Normalized Differential Build-up and Bare Soil Index	◆
Precipitation	☒	Water and Soil Erosion	◆, ☒
Elevation	○	Gross Domestic Product	☒
Slope	○	Aspect	○
Population Density	◆, ☒	Soil Type	◆, ☒

Table 1: Sample of 14 EVIs and their data sources (Note: Remote Sensing ◆, Non remote sensing ☒, Derived from DEM ○)

Recommendations

The RS datasets adopted in previous research are mainly coarse to medium-resolution datasets. It is suggested that future research should leverage high-resolution datasets for more actionable results on local scales. In addition, the development of software should also be considered to streamline the process of EVA with rapidity and accuracy. Finally, more research is needed on methods to develop a range of EVIs from RS datasets.

References

- Du, P., et al., *Evaluation of the spatio-temporal pattern of urban ecological security using remote sensing and GIS*. International Journal of Remote Sensing, 2013. **34**(3): p. 848-863.
- Ouyang, X., et al., *Applying a projection pursuit model for evaluation of ecological quality in Jiangxi Province, China*. Ecological Indicators, 2021. **133**.
- Wang, S.X., Y. Yao, and Y. Zhou, *Analysis of Ecological Quality of the Environment and Influencing Factors in China during 2005-2010*. International Journal of Environmental Research and Public Health, 2014. **11**(2): p. 1673-1693.
- Liou, Y.-A., A.K. Nguyen, and M.-H. Li, *Assessing spatiotemporal eco-environmental vulnerability by Landsat data*. Ecological Indicators, 2017. **80**: p. 52-65.

Fabrication and characterization of CuAlO₂ thin film transistor by Digitally Processed DC Reactive Sputtering

Ali Mehdi ¹ and Hideo Isshiki ²

Department of Engineering Science, The University of Electro-Communications Tokyo, Japan

a2043013@edu.cc.uec.ac.jp and hideo.issshiki@uec.ac.jp

Abstracts

Researchers are interested in the wide-band gap (< 3 eV) metal oxides (MOs) having high mobility as well as reliable optical transparency for the application in large-area electronics. Majority of MOs reported in commercial applications are *n*-type and the improvement in the performance of *p*-type MOs comparable to *n*-type counterparts are still challenged. The main purpose of this research is to synthesize *p*-type CuAlO₂ (CAO) Digitally Processed DC Reactive Sputtering technique under LBL approach and the integration of CAO in transistors to check its electrical performance. For the fabricated CAO *p*-TFT, threshold voltage (*V_t*) and a hole mobility were improved with higher annealing temperature. To our best knowledge, this work demonstrates the first time LBL approach is utilized in the growth of CAO thin film with good field effect mobility. It opens an important route towards the development of CMOS logic circuits.

Introduction

CuAlO₂ oxides are interesting due to its potential applications i.e., TCO, optoelectronic materials, thermoelectric material, and photo catalytic nature. CAO (a ternary oxide) is one of the prominent members of delafossite family. Being a part of delafossite family, CAO is composed of AlO₆ octahedra spread out forming a basal layer and alternating stacking layers of O-Cu-O dumbbells structure vertically. In the context of stacking, two poly types are reported: rhombohedral *3R* type with *R3m* space group symmetry and hexagonal *2H* type with space group symmetry of P63/mmc. Rhombohedral-*3R* phase possesses *ABCABCABC* stacking sequence while hexagonal-*2H* compounds have *ABABAB* stacking sequence.

Research Objectives

The main purpose of this research is to synthesize *p*-type CuAlO₂ by Digitally Processed DC Reactive Sputtering technique under layer by layer (LBL) approach and integration in thin film transistors.

Methodology

Deposition was performed on Si (100) substrates utilizing Cu and Al metallic targets of 2-inches diameter, by a digitally processed DC sputtering (DPDS) [1] system (*p*-RAS, Shincron) under a layer-by-layer (LBL) approach. The sequential sputtering was performed under plasma pulse frequency of 80 kHz, pulse duty at 50 %, and process pressure of 5 Pa. The DC power supply of 70 W was driven in a constant power (CP) mode. The Ar-gas of 50 sccm while O₂-gas of 13 sccm introduced in the chamber. The cycle time frame was set for 15.9 s to take oxygen purge time. Employing DPDS, the independent sequential pulse of the plasma current was stably observed as shown in Fig.1(a). Here the oxidation process was performed in the gap between each current pulse. To proceed with the LBL approach, *c*-axis coordination of CAO was chosen. Because the atomic arrangement indicates the Cu-O-Al-O stacked structure as shown in Fig.1(c). The height of the unit cell along the *c*-axis is 1.14 nm. The deposition was desirable to half of the height i.e., 0.57 nm/cy confirmed by FESEM shown in Fig. 1(b). The elemental composition was confirmed by an electron probe micro-analyzer (EPMA) as shown in Fig. 1(d). TFT consists of electrodes, active channels, and dielectric layers. Bottom gate top contact CAO/SiO₂/Si TFTs were fabricated by a shadowmask.

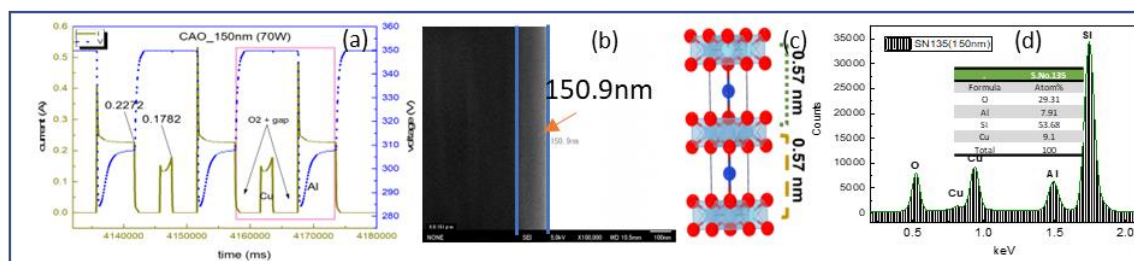


Fig. 1: (a) Pulse voltage and plasma current, (b) FESEM image, (c) CAO Unit cell and (d) EPMA micro-graph.

Results

XRD patterns of CAO films obtained under different annealing temperatures for 30 minutes have plots in Fig.2(a). In CAO thin film, annealing is an essential factor for a qualitative improvement in the grown film [2]. From the XRD graph, no peaks were observed in the film that annealed below 500 °C. However, for post annealing over 600 °C several peaks appeared. The peaks at 35.8° depicts the presence of CuO for post annealed film at 600 °C. For further increments in annealing temperatures of above 800 °C beside other peaks the CAO also observed. The diffraction peaks at 2 θ value of 31.28°, 36.89° corresponding to the planes (004), (102) respectively are the assigned to CAO. With the increasing annealing temperature, the number of peaks decreased as a result of the phase conversion toward CAO. The more energy absorption at higher temperature is the reason behind the enhancement in crystalline nature at upper temperature. The peaks of CAO (004) become more prominent in the XRD pattern at higher temperatures indicating the preferred growth orientation in a along(004) direction. The XRD results confirmed hexagonal crystal structure for CAO in the space group P6₃/mmc.

The TFT device is evaluated while using two main characteristic curves: output (I_D vs V_{DS}) depicted by Fig. 2(b) and transfer (I_D vs V_g) characteristic curves shown by Fig. 2(c). Field effect mobility (μ_{FE}) is the main electrical parameters of TFTs. Along with μ_{FE} , V_t is also an important parameter involved in the evaluation of TFT devices which can be extracted from the characteristic curves. The CAO TFTs present typical *p*-type behavior. The threshold and field effect mobility gradually enhance with the increase in annealing temperatures. Two main factors are involved: the first one is the improvement of morphology and stoichiometry at higher temperatures. The 2nd factors are the elimination of insulator-like CuAl₂O₄ phase and dominance in CAO phase at higher temperatures and the enhancement of hole transport due to phase conversion from a mixture of nanocrystalline and enlargement of grain size. The higher annealing is useful in the reduction of trap at channel/dielectric interface which is attributed in the improvement of V_t [3].

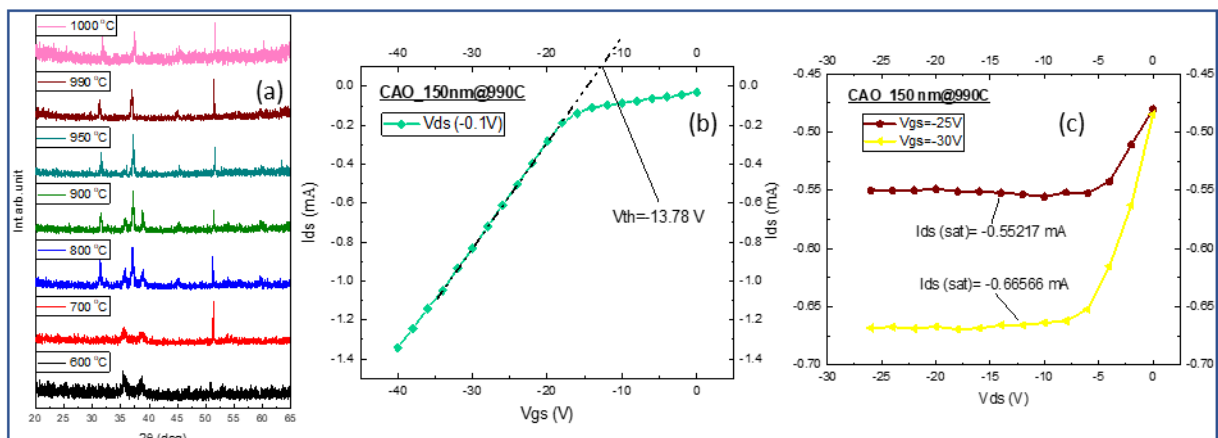


Fig. 2: (a) XRD pattern (b) Transfer characteristics (I_{ds} - V_{gs}) (c) Output characteristics (I_{ds} - V_{ds}) of CAO TFT at 990 °C.

Conclusion

CAO thin films were deposited on (100)Si substrates by DPDRS under LBL growth technique. This work optimized the deposition rate to our desired Rd/cy of 0.57 nm/cy where the Al to Cu was slightly over stoichiometry. The deposited films were annealed with varying annealing temperature about 1000 °C. We found that 990 °C is an optimized annealed condition. It is concluded that DPDRS under LBL approach is a good way in the growth of CAO crystalline thin film. Under the same deposition condition, CAO was grown on SiO₂/Si substrate and the aluminum electrodes are thermally deposited by thermal evaporation and finalized CAO *p*-TFTs. For the optimized TFTs the threshold was 13.78 V and mobility of 7.29 cm²V⁻¹s⁻¹ recorded.

References

- [1] H. Isshiki, Y. Tanaka, K. Miyagi, T. Kasumi, G. Nakamura and S. Saisho, Jpn. J. Appl. Phys. 61(2022) SA1001.
- [2] Castillo-Hernández, G., Mayén-Hernández, S., Castaño-Tostado, E., DeMoure-Flores, F., Campos-González, E., Martínez-Alonso, C., & Santos-Cruz, J., *Results in Physics*, 9, (2018) 745-752.
- [3] Ding, X., Qin, C., Song, J., Zhang, J., Jiang, X., & Zhang, Z. J. N. r. l. (2017). The influence of hafnium doping on density of states in zinc oxide thin-film transistors deposited via atomic layer deposition. *I2*(1), 1-7.

Neutronics Design of Small 100MWe of Plutonium Fuelled Molten Salt Nuclear Power Plant

A. Waris^{1,2*}, C. Wulandari¹, S. Permana^{1,2}, and S. Pramuditya^{1,2}, I G B Baskara Nugraha³

¹Department of Physics, Faculty of Mathematics and Natural Sciences, Bandung Institute of Technology, Indonesia

²Department of Nuclear Science and Engineering, Faculty of Mathematics and Natural Sciences, Bandung Institute of Technology, Indonesia

³Department of Electrical Engineering, School of Electrical & Informatics Engineering, Bandung Institute of Technology
Jl. Ganesa 10 Bandung 40132, INDONESIA

*awaris@itb.ac.id, wulandari@student.itb.ac.id, psidik@itb.ac.id, syeilendra@itb.ac.id, baskara@stei.itb.ac.id

Recently, the net-zero carbon emission become the biggest issue regarding the energy or electricity generation. During the 2021 Summit, most of G20 leaders pledge to work toward zero carbon emissions by 2050. To achieve this goal, the nuclear energy can play the significant role. The nuclear power plants can produce electricity with high efficiency and without carbon emission.

As of May 2022 there were 439 nuclear reactors in operation and connected to the grid in some 30 countries around the world. The United States had the largest number of nuclear power reactors in operation at the time, at 92 units.

Almost all of the operating nuclear power plants all over the world now, are categorized as the 3rd Generation of Nuclear Power Plants. One of the consideration regarding the nuclear energy utilization is the spent fuels or nuclear wastes management.

Since the end of the 20th century, the Generation IV Forum has been established to select and promote the 4th Generation of Nuclear Power Plants to be constructed and utilized from the year 2040. The six new nuclear reactor technologies have been selected, those are: Sodium fast reactor (SFR), Lead fast reactor (LFR), Very high temperature reactor (VHTR), Gas cooled fast reactor (GFR), Supercritical water cooled reactor (SWCR), and Molten salt reactor (MSR).

Neutronic analysis of a small 100 MWe Molten Salt Reactor with Plutonium fuel has been performed. The reactor has a power output of 100 MWe which meets the demand for electricity generation in several regions or provinces in Indonesia outside Java Island. SRAC Code has been used for this neutronic evaluation with JENDL 4.0 as the nuclear data library. In this study, LiF-BeF₂-ThF₄-PuF₄ is used as an initial fuel composition. Thorium and Plutonium concentrations in the fuel salt were varied to obtain the optimum fuel composition, leading to a criticality condition.

The results show some neutronic parameters, such as the conversion ratio, neutron spectra, and the effective multiplication factors. By changing the Plutonium concentration in the initial fuel salt composition, we obtained the minimum Plutonium loaded for the reactor criticality for 2000 days of operation time is 0.90 mol%.

Keywords; Neutronics, Plutonium, Small MSR, Thorium, SRAC

Protecting Hot Carriers by Introducing Organic Cations in Halide Perovskite Quantum Dots

Hua Li¹, Chao Ding¹ and Qing Shen¹

The University of Electro-Communications

r2043014@edu.cc.uec.ac.jp; ding@jupiter.pc.uec.ac.jp; qingshen3@yahoo.co.jp

Abstract

Perovskite quantum dots with mixed A-site cations have been a promising class of materials for optoelectronic applications owing to the spontaneous cross-exchange of A-site cations. A deeply understanding of how the A-site cations cross-exchange affects the hot carrier relaxation dynamics in PQDs has a profound implication for further developing the disruptive hot-carrier solar cells (HCSCs). However, it has yet to be experimentally studied so far. Here, we investigate the hot carrier cooling kinetics in pure FAPbI₃, CsPbI₃ and the alloyed FA_{0.5}Cs_{0.5}PbI₃ QDs by using ultrafast transient absorption (TA) spectroscopy in combination with temperature-dependent PL methods. It is demonstrated that A-site cations cross-exchange can not only reduce the defect states but also exhibit longer hot carriers cooling lifetime at higher excitation intensity. The lifetimes of initial fast cooling stage (<1 ps) for all organic cation-containing PQDs were observed to be shorter than those of inorganic CsPbI₃ QDs in the low-excitation regime which was verified by the strength of electron-phonon coupling extracted from temperature-dependent PL. We found that, however, thanks to the introduction of optical ‘hybrid phonon’ in alloyed PQDs facilitates the efficient acoustic phonon up-conversion, and thus the slow stage cooling lifetimes in alloyed PQDs were significantly extended at higher excitation intensity.

Introduction

In the past few years, the metal halide perovskite quantum dots (PQDs) semiconductor materials with an APbX₃ (X = Cl, I, Br or mixed halide ions) formula (see Fig. 1), in which A is a monovalent cation formamidinium (FA⁺, CH(NH₂)₂⁺), methylammonium (MA⁺, CH₃NH₃⁺), or cesium (Cs⁺), have attracted a great deal of research for their unique properties such as easily tuned energy levels over the whole visible spectra by changing their size and chemical compositions, superior phase stability, high photoluminescence quantum yield (PLQY) and low open circuit voltage deficit (V_{oc} deficit) in contrast to the bulk perovskite materials. It has shown great promise for application in optoelectronic devices. Several recent experimental and theoretical reports revealed that the HCs cooling lifetime in halide perovskites strongly depends on the A-site cations composition. Chen et al. uncovered that at the same excitation energy, the HCs cooling time is cation-dependent in APbBr₃ PQDs with the following order: CsPbBr₃ > MAPbBr₃ > FAPbBr₃, which was explained by altering electron-phonon coupling resulting from the different interaction between A-site (Cs, MA and FA) cations and Pb-Br framework.^[1] Madjet et al. further supported this trend in iodide-based perovskites employing nonadiabatic molecular dynamics simulations.^[2] In contrast, yang et al. validated that the presence of rotatable organic cations (FA, MA) in lead-halide perovskites can generate several times slower phonon emission than in Cs-based counterparts as a result of an effective acoustic phonon up-conversion.^[3] As above, the impacts of A-site cations on HCs relaxation dynamics are still controversial and needed more fundamental studied. A deeply understanding of how the A-site cations cross-exchange affects the ultrafast HCs relaxation processes in PQDs is a key to further optimize the design and utilization of these materials for next generation optoelectronic applications such as HCSCs.

Research Results

The pure FAPbI₃ and CsPbI₃ QDs exhibited PL emission peaks at ~783 and ~686 nm, respectively. Upon mixing two of them, the emission peak position for alloyed PQDs can be easily tuned, and the two peaks eventually merged into a narrow single one within several minutes, indicating the formation of alloyed PQDs without phase segregation (see Fig. 2a). The X-ray diffraction (XRD) was performed to further analyze the structural evolution of the A-site cation cross-exchange. As depicted in Fig. 2b, no additional peak was observed upon A-site cations cross-exchange, the alloyed FA_{0.5}Cs_{0.5}PbI₃ QDs still retain their pure cubic perovskite phase. The zoomed portion of the main diffraction peaks in Fig. 2c show that the diffraction peaks of the alloyed FA_{0.5}Cs_{0.5}PbI₃ QDs shift obviously between the patterns of the two pure PQDs. Such a gradual shift is due to the different sizes of FA (253 pm) and Cs (167 pm) cation and the crystal lattice will be expanded by a larger cation. To investigate the hot carriers (HCs) cooling dynamics, the hot carrier temperature (T_c) was extracted by fitting the high-energy tails of prominent photobleach spectrum for all pure and alloyed PQDs using the Maxwell–Boltzmann function (Fig. 3b). The T_c as a function of time delay for all pure and alloyed PQDs at low pump fluence are summarized in Fig. 3c.

Notably, the HCs lifetime τ_{c-ph} of CsPbI₃ QDs is longer (~ 0.38 ps) than those of PQDs with organic cation (FA: ~ 0.29 ps). After A-site cations cross-exchange, the HCs cooling dynamics wasn't efficiently slowed down with lifetime τ_{c-ph} close to that of pure PQDs with organic cations (~ 0.3 ps), which can be proved by the results of temperature-dependent PL. However, the case is different at high excitation intensity, the cooling lifetime of this slow stage for CsPbI₃ (3.6 ps) is shorter than that of FAPbI₃ (6.1 ps), upon A-site cations cross-exchange, the significant slow cooling lifetimes of about 8.4 ps were also obtained in FA_{0.5}Cs_{0.5}PbI₃ QDs.

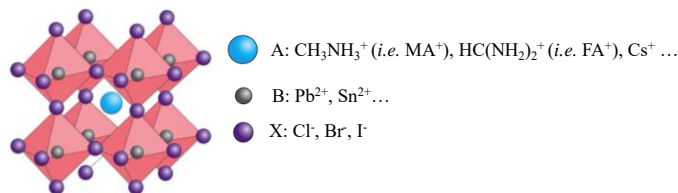


Fig. 1. Crystallographic structure of perovskite materials.

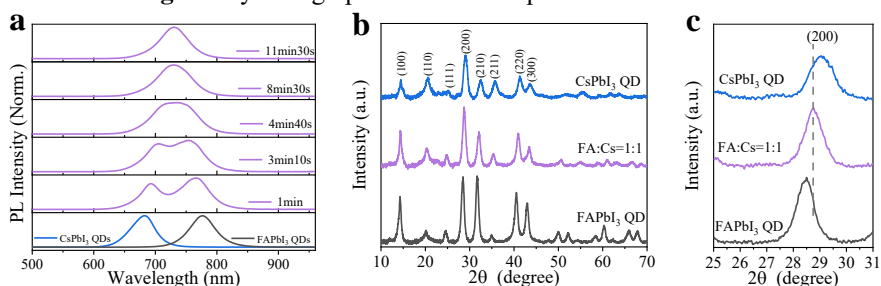


Fig. 2. Kinetics of FA and Cs cation cross-exchange under the conditions of lower concentration PQDs in the solution. (b) Wide-angle XRD patterns of all pure and alloyed PQDs. (c) Zoomed-in view of the (200) diffraction peaks.

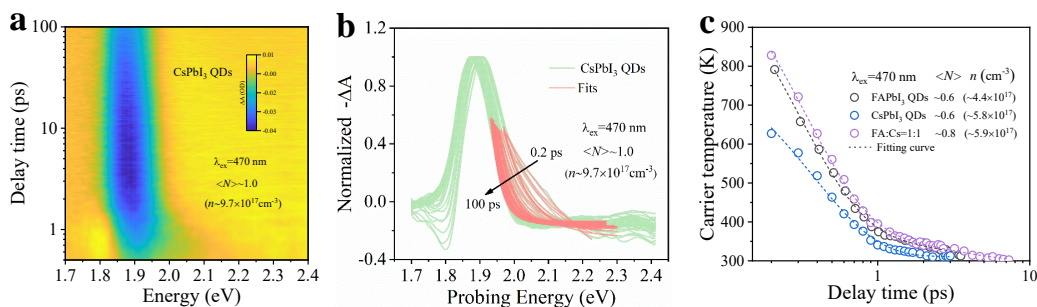


Fig. 3. (a) Representative pseudo-color TA spectra of CsPbI₃ QDs. (b) The normalized TA spectra pumped at 470 nm with an initial carrier density of $9.7 \times 10^{17} \text{ cm}^{-3}$. The red lines are fitting curves. (c) Time-dependent carrier temperature (T_c) of all pure and alloyed PQDs.

Conclusion

In summary, the lifetime of initial fast cooling stage (< 1 ps) for all organic cation-containing PQDs are shorter than inorganic CsPbI₃ QDs, which is ascribed to the strong coupling of electron-phonon due to the motion of organic cation, this was verified by the strength of electron-phonon coupling extracted from temperature-dependent PL. Surprisingly, the slow stage cooling lifetimes in alloyed FA_{0.5}Cs_{0.5}PbI₃ QDs were significantly prolonged under higher excitation intensity. These findings reveal that the presence of organic cation in alloyed PQDs materials benefits to slow down the HCs relaxation process at higher carrier density.

References

- [1] Chen, J., Messing, M. E., Zheng, K., & Pullerits, T. (2019). *Journal of the American Chemical Society*, 141(8), 3532-3540.
- [2] Madjet, M. E., Berdiyrov, G. R., El-Mellouhi, F., Alharbi, F. H., Akimov, A. V., & Kais, S. (2017). *The journal of physical chemistry letters*, 8(18), 4439-4445.
- [3] Yang, J., Wen, X., Xia, H., Sheng, R., Ma, Q., Kim, J., ... & Conibeer, G. (2017). Acoustic-optical phonon up-conversion and hot-phonon bottleneck in lead-halide perovskites. *Nature communications*, 8(1), 1-9.

Automatic Allocation of Parking Lot's Lanes utilizing Methods of Image Processing and Machine Learning

Apiwat Sangnooree¹

Computer & AI department, School of Engineering, The University of Thai Chamber of Commerce , 126/1 Vibhavadee-Rangsit road, Rachadaphisek, Dindeang, Bangkok, Thailand, 10400

apiwatsangnooree@gmail.com, apiwat_san@utcc.ac.th

Abstract: This research utilizes a modified AI (artificial intelligent)'s method for automatic allocation of parking lot's lanes. The mentioned method uses image processing procedures and SVM (Supported Vector Machine) which is a machine leaning for deciding the availability of free lanes in a parking lot instead of an installed object detection's sensor in each lane. For the process of the research, it begins with inputting recorded images, consisting of parking lot's lanes, vehicles and non-vehicle objects from a static camera into a trained data's collection procedure. Secondly, a tested image from the camera is inserting in SVM in order to compare with those trained data for available lanes' analysis. Lastly, the analysis of SVM will be displayed as an analyzed image comprises the recorded parking lot as well as available lanes. Experimentally, the percentage of accuracy is 100. According to the research's concept, it will also able to be implemented for any temporal parking lots as well as free space's allocations in any outdoor areas.

Keywords: automatic lanes' allocation, image processing, machine learning, AI.

Introduction: Nowadays, for automatic allocation of lanes, many parking lots use an installed object detection's sensor in each lane for indicating whether the lane is occupied or not. Therefore, they need purchasing for a large number of sensors, time consumption for installation and the maintenance of related devices and peripherals. Furthermore, the sensors cannot categorize non-vehicle objects out of vehicles in any lanes so that they declare all mentioned lanes are occupied which is not true. As a reason, our research introduces methods of image processing and machine learning instead of the sensors because only a static camera and laptop computer used for recording images, including the analysis is able to capture many lanes so that it is an inexpensive technology comparing to the disadvantages of sensors. Besides, such technology is portable so that it will also able to be implemented for any temporal parking lots as well as free space's allocations in any outdoor areas. From the advantages mentioned earlier, we design the research's concept and schematic to conform our requirements which will be declared in the latter section.

The Research's Concept and Schematic: According to the analyzing schematic of the research as shown in Fig.1, it begins with inputting recorded images, consisting of parking lot's lanes, vehicles and non-vehicle objects from a static camera into a trained data's collection procedure. In this research, we define vacant lanes and occupied lanes by non-vehicle objects such as humans, pets or traffic cones as available lanes meanwhile, occupied lanes by vehicles as unavailable ones, respectively. From this process, all data will be exploited as trained data for supervised learning of the research which is SVM in the latter step. Secondly, when we already had trained data, a tested image consisting of parking lot's lanes, vehicles and non-vehicle objects from a static camera is inputting in SVM as a tested data in order to analyze for available lanes. Lastly, the analysis of SVM will be displayed as an analyzed image comprises the recorded parking lot as well as available lanes.

Experimental Results: For the results from simulations, they are illustrated in Fig.2 and Fig.3, respectively. Fig.2 shows the sample results recorded from UTCC's parking lot. Fig. 2(a) displays that one lane is occupied with a car meanwhile other six lanes are available, including a lane occupied with a traffic cone which we defined as a non-

vehicle object in the research. In addition, Fig. 2(b) illustrates that one lane is occupied with a car meanwhile other six lanes are available, including a lane occupied with a human which we defined as a non-vehicle object as well as a traffic cone. To support more reliable results, another experiment is undertaken as shown in Fig. 3. Fig.3 shows the sample results recorded from Lotus's parking lot on Tiwanon, 26 th road. Fig. 3(a) displays that two lanes are occupied with cars meanwhile other three lanes are available, including a lane occupied with humans. Moreover, Fig. 3(b) illustrates that two lanes are occupied with cars meanwhile other three lanes are available but it is a different scene, comparing to Fig 3(a). Experimentally, 220 lanes are analyzed and the percentage of accuracy is 100.

Conclusion: This research utilizes image processing procedures and SVM for deciding the availability of free lanes in a parking lot. Experimentally, the correction of the analysis is extremely high.

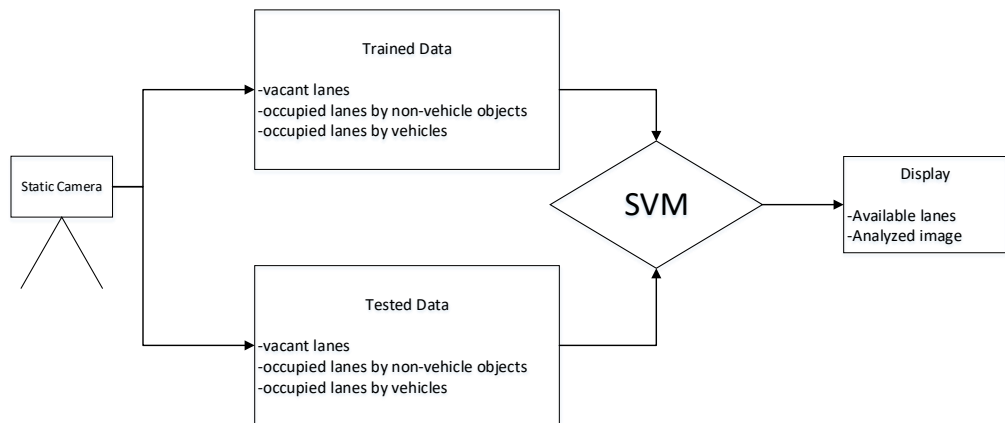


Fig.1: Available Lanes' Analyzing Schematic of the Research



Fig. 2: Sample Results of the Research Recorded from UTCC's Parking Lot

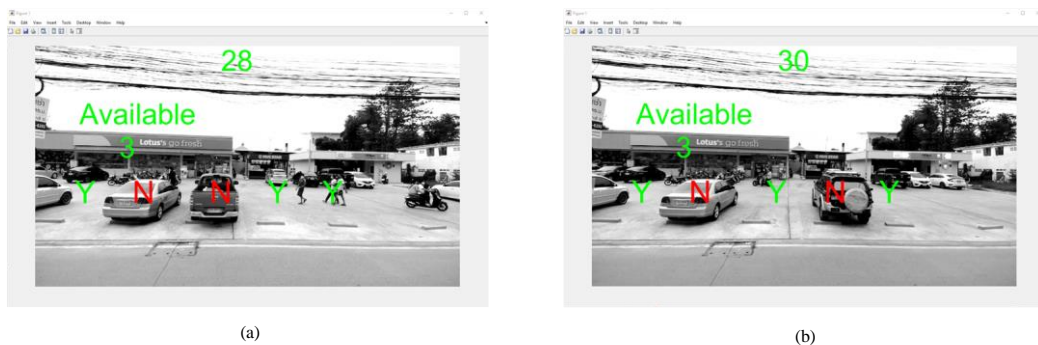


Fig. 3 Sample Results of the Research Recorded from Lotus's Parking Lot on Tiwanon, 26 th Road

Cyclone Dust Collector: Apparatus Design and Analysis

Ahmad Imam Rifa'i^{1*}, Budi Kristiawan², Koji Enoki³, Agung Tri Wijayanta^{2*}

¹Mechanical Engineering, Politeknik Negeri Sriwijaya, Jl. Sriwijaya Negara Bukit Besar, Palembang 30139, Indonesia

²Mechanical Engineering, Universitas Sebelas Maret, Jl. Ir. Sutami 36A Ketingan, Surakarta 57126, Indonesia

³Mechanical and Intelligent Systems Engineering, The University of Electro-Communications, 1-5-1 Chofugaoka, Chofu, Tokyo 182-8585, Japan

imamrf@polsri.ac.id; budi_k@staff.uns.ac.id; enoki.koji@uec.ac.jp; aguntw@uns.ac.id

ABSTRACT

Dust collectors are widely used in various industries to reduce hazardous air pollution from the working place. The dust particles can be separated from the airflow and trapped on the wall by centrifugal force and then fall into the dust hopper by gravity. In this research, dust collectors have been designed which are removed during the industrial roasting coffee process. The result analysis shows that the frictional weight collection efficiency of the designed dust collector was 70% with a particle size larger than 5 microns.

Keywords: Collector, Cyclone, Lapple.

1. INTRODUCTION

Industries that are using the technologies for the purification of the air. The cyclone dust collector can also be used to filter the air by removing the dust particles. Numerous studies have been conducted to improve the dust collector and particle classification performance. Taiwo et al. designed a cyclone dust collector for a cement factory. The findings were reported that the number of effective turns in a cyclone is the number of revolutions the gas spins while passing through the cyclone outer vortex. A higher number of turns of the air stream results in a higher collection efficiency [1]. Kosaki and Chono, investigated the time characteristics of the dust collection and particle classification performance of a conical cyclone. The result is that the dust collection efficiency and partial separation efficiency of the cyclone decrease with time, and become approximately constant after 60 min [2]. Xie et al. proposed combining both cyclone separator and cartridge filter. The result shows that the pressure drop of the cartridge-filtering cyclone is higher than that of the common cyclone and cartridge filter at the same inlet flow rate [3]. Kanojiya et al. reported designing a dust collection machine for collecting the dust of polyurethane material which is removed during the grinding operation with the efficiency of the cyclone dust collector coming to 61% by using the lapple graph. Additionally, reduced the diameter of the inlet hose pipe, the efficiency of the dust collector machine will be improved [4] [5]. Hooke et al reported separation efficiency was also found to increase with the particle concentration [6]. The purpose of this paper is to

report the design and analysis of frictional weight collection efficiency cyclone dust collector for industrial roasting coffee with a lapple model..

2. METHOD

A dust Collector is a tool that serves to separate solid particles with clean air. In general, the dust collector consists of four main components, namely: blower, dust collector tube, cone, and bag filter. Dimensions standard of cyclone dust collector can be shown in Fig. 1. and Table 1, respectively.

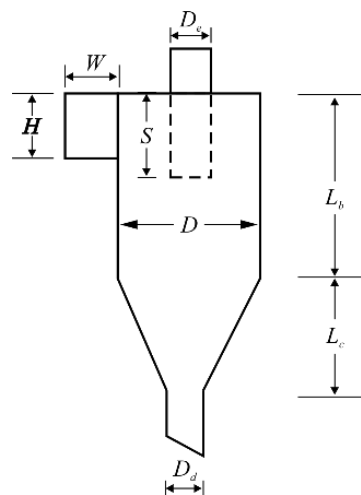


Fig. 1 Dimensions

Table 1. Standard Cyclone Dimensions

Dimension	Conventional	
	(1)	(2)
Body Diameter, D/D	1.0	1.0
High of Inlet, H/D	0.5	0.5
Width of Inlet, W/D	0.25	0.25
Diameter of Gas Exit, D_e/D	0.5	0.5
Length of Vortex Finder, S/D	0.625	0.6
Length of Body, L_b/D	2.0	1.75
Length of Cone, L_c/D	2.0	2.0
Diameter of Dust Outlet, D_d/D	0.25	0.4

The Number of Effective Turns (N_e) was expressed the following equation (1):

$$N = \frac{1}{H} \left[L + \frac{Z}{2} \right] \quad (1)$$

where N is the number of turn inside the device, H is the height of inlet duct, L is the length of cyclone body, Z is the length (vertical) of cyclone cone.

To determine the diameter of the resulting particle diameter, the empirical equation was expressed as follows eq. (2) :

$$d_p = \left[\frac{9\mu W}{\pi N V (\rho_1 - \rho_2)} \right]^{\frac{1}{2}} \quad (2)$$

Particle size ratio, the empirical equation was expressed as follows eq. (3) :

$$d_{pc} = \left[\frac{9\mu W}{2\pi N V (\rho_1 - \rho_2)} \right]^{\frac{1}{2}} \quad (3)$$

where N is the number of turn inside the device, W is the width of inlet, V is the terminal drift transverse velocity, d_p diameter of particle, ρ is the density of the particle.

3. RESULTS AND DISCUSSION

3.1. Working Model

Coffee roasting smoke dust pollution that enters the dust collector tube due to the blower suction power at a certain speed will flow centrifugally. The air carrying the dust will be thrown centrifugally so that it will gather around the wall of the dust collector tube and at a certain mass will fall to the bottom of the cone due to the force of gravity. The cone shape on the lower side of the dust collector tube wall allows dust to be accommodated and will flow into the collection tube as the mass of dust particles increases. Dust with small particle size and still attached to the wall of the dust collector tube will be carried back by the air velocity which will be forwarded to the outlet. A filter is provided to filter the air and particles of the air are trapped in the filter before being discharged into the surrounding air. Dimensions of cyclones used in this research were denoted in **Table 2**. the dimension of cyclones were shown in **Fig. 1**.

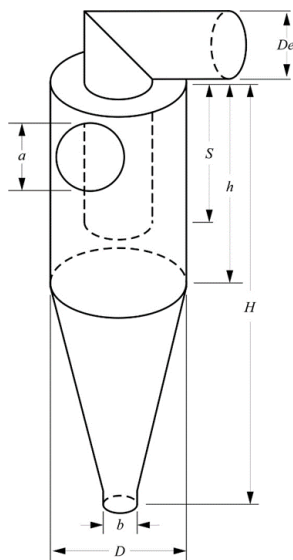


Fig. 2 Dimension

Table 2 Dimension of cyclone

D	a/D	b/D	De/D	S/D	h/D	H/D
1.0	0.4	0.2	0.4	1.0	1.4	1.2

3.2 Collection Efficiency

Fig. 3 shows the efficiency of the cyclone dust collector where the particle size ratio D_p/D_{cut} is larger than 5 micron have frictional weight collection efficiency 70%. The velocity of the swirling flow is believed to decrease the number of effective turns with the results that reduce the velocity of the swirling flow inside the cyclone. The increasing resistance of the swirling flow increases as more particles are introduced to the cyclone over time. Moreover, by reducing the diameter of the inlet hose pipe, the efficiency of the dust collector machine will be increased.

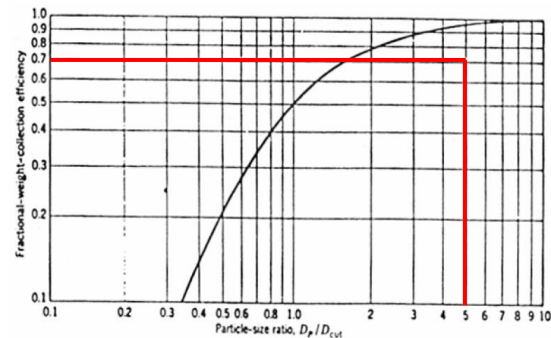


Fig. 3 Frictional weight-size collection efficiency of cyclone dust collector

4. CONCLUSION

Analysis performance of the cyclone dust collector can be concluded that the dust collection efficiency of the designed dust collector was 70% with a particle size larger than 5 microns.

5. ACKNOWLEDGEMENT

Research grants supported by Politeknik Negeri Sriwijaya and Universitas Sebelas Maret, Indonesia are acknowledged.

6. REFERENCES

- [1] M. I. Taiwo, M. A. Namadi, and B. Mokwa, *American Journal of Engineering Research (AJER)*, no. 5, pp. 130–134, 2016.
- [2] Y. Kosaki, T. Hirai, Y. Yamanaka, and K. Takeshima, *Powder Technol*, vol. 277, pp. 22–35, Jun. 2015.
- [3] B. Xie, S. Li, H. Jin, S. Hu, F. Wang, and F. Zhou, *Powder Technol*, vol. 339, pp. 695–701, Nov. 2018.
- [4] B. Kristiawan, A. I. Rifa'i, K. Enoki, A. T. Wijayanta, and T. Miyazaki, *Powder Technol*, vol. 376, pp. 254–262, Oct. 2020.
- [5] M. T. Kanojiya, N. Mandavgade, V. Kalbande, and C. Padole, *Materials Today: Proceedings*, vol. 49, pp. 378–382, 2021
- [6] J. Haake, T. Oggian, J. Utzig, L. M. Rosa, and H. F. Meier, *Powder Technol*, vol. 374, pp. 95–105, Sep. 2020.

IMPACT OF SEVERAL TERRAIN CLUTTER MODELS ON DETECTION PERFORMANCE OF BISTATIC PASSIVE RADAR SYSTEM USING P1 SYMBOL IN VIETNAMESE DVB-T2 SIGNALS

Quang Huy Duong¹, Tien Hai Nguyen²

Le Quy Don Technical University

huydq_k31@lqdtu.edu.vn, haint0511@gmail.com

1. Abstract

DVB-T2 digital video broadcasting-terrestrial signal is being widely used for passive radar systems as an illuminator of opportunity. In the DVB-T2 signal structure, there is P1 symbol with a known and simple structure that can be applied to radar. The article records Vietnam's DVB-T2 signal and uses P1 symbol on the recorded data as a signal to detect target. Investigate the influence of clutter reflected from different terrain types on the detection performance of bistatic passive radar system using P1 symbol of Vietnam DVB-T2 signal for the Swerling 5 target model, the investigated clutter has Weibull, Log-Normal and Rayleigh distribution functions. To evaluate the detection performance, we used the Monte-Carlo simulation method. The results of the article have shown that the detection performance of the passive radar system using P1 symbol in the conditions of clutters with Gauss, Weibull, Log-Normal and Rayleigh distributions is different.

2. Introduction

Passive radar systems use non-cooperative illuminators of opportunity to detect and track targets by processing available signals. These signals are usually commercial signals. Recently, the Digital Video Broadcasting Terrestrial Version 2 standard (DVB-T2) [1][2], has been introduced and implemented in many countries. In this paper, we research the passive radar system model using the P1 symbol in DVB-T2 frame and study the target detection problem of the system. Specifically, we use a unique structure of P1 symbol, which presents in every DVB-T2 data frame recorded in Vietnam, and the correlation-based detection algorithm has been used in the document [3] to build detector. At the same time, we evaluate the influence of clutter reflected from different terrain types according to the Weibull, Log-Normal and Rayleigh distribution functions [4][5][6] on the detection performance of the system for the target sample Swerling 5. To evaluate the detection performance of the radar system, we added patterns of clutter to the DVB-T2 signal recorded in Vietnam.

3. Proposed Scheme

The DVB-T2 signal is an OFDM modulated signal with a standard, predefined structure, where the number of subcarriers depends on the mode of operation. The structure of the DVB-T2 frame is shown in Figure 1a. The frame begins with P1 symbol. This is used in the DVB-T2 frame to speed up channel searching and to enable fundamental time and frequency synchronization of the DVB-T2 signal. P1 symbol is a 1K OFDM symbol and consists of three distinct parts A, B, and C as shown in Figure 1b [7][8].

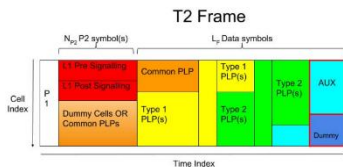


Fig 1a: DVB-T2 frame structure excluding the guard intervals for clarity

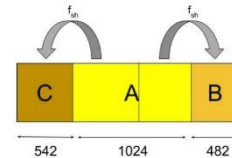


Fig 1b: P1 symbol structure with the main 1k FFT OFDM symbol (A)

To evaluate the detection performance of the radar system, we added patterns of clutter to the DVB-T2 signal recorded in Vietnam. The problem of target detection and evaluation of detection performance for passive radar can be formulated as a test of the binary hypothesis H_1 and H_0 :

$$\begin{cases} H_1: x_t(n) = as(n - n_t) + w_0(n) + c(n) \\ H_0: x_t(n) = w_0(n) + c(n) \end{cases} \quad (1)$$

Where $s(n)$ is the transmitted DVB-T2 signal with $n = 0, \dots, N - 1$, containing only one P1 symbol and a number of data symbols. $x_t(n)$ is received signal in the surveillance channel. α is the RCS parameter of the target, n_t represents the unknown propagation delay, $w_0(n)$ is the receiver noise, and $c(n)$ corresponds to clutter models such as Weibull, Log-Normal and Rayleigh.

The model of the correlation-based detection algorithm is shown in Figure 2.

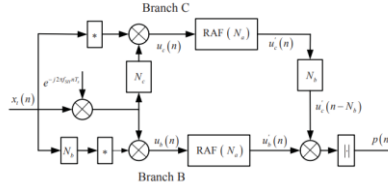


Fig 2: Diagram of correlation-based detection in the target channel

4. Simulation results

In Fig. 3, Fig. 4, Fig. 5, Fig. 6, we evaluate the performance in terms of the detection probability using 100000 independent computer trials, where Pd is plotted versus SCR for $P_{fa} \in \{10^{-2}, 10^{-3}, 10^{-4}, 10^{-5}\}$. Among the above distributions, the Weibull distribution has the highest required SCR ratio to achieve the same detection performance as the Log-Normal and Rayleigh distributions.

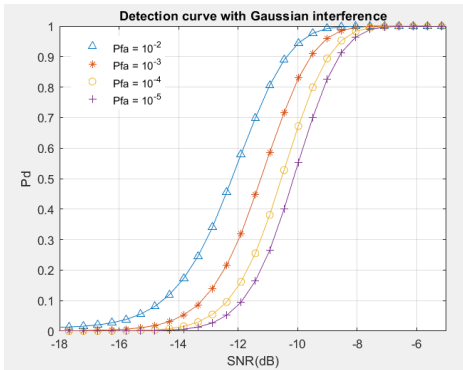


Fig 3: Detection curve on Gaussian PDF clutter and $P_{fa} \in \{10^{-2}, 10^{-3}, 10^{-4}, 10^{-5}\}$

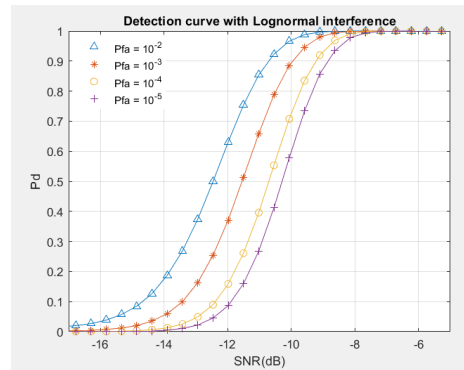


Fig 4: Detection curve on Log-normal PDF clutter and $P_{fa} \in \{10^{-2}, 10^{-3}, 10^{-4}, 10^{-5}\}$

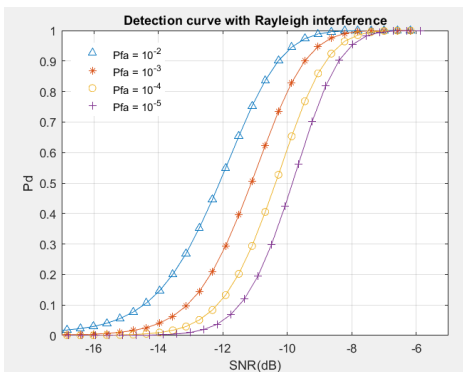


Fig 5: Detection curve on Rayleigh PDF clutter and $P_{fa} \in \{10^{-2}, 10^{-3}, 10^{-4}, 10^{-5}\}$

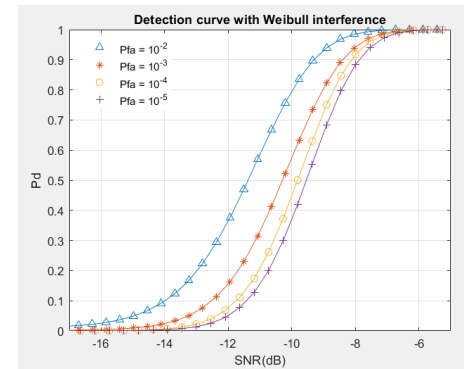


Fig 6: Detection curve on Weibull PDF clutter and $P_{fa} \in \{10^{-2}, 10^{-3}, 10^{-4}, 10^{-5}\}$

In this paper, detecting the presence of the target based on the C-A-B structure of the P1 symbol has been researched. The target detection problem of passive radar with a DVB-T2 illuminator has been considered in the presence of clutters with Weibull, Log-Normal and Rayleigh distribution models.

Finally, we have assessed the performance of the detector under the influence of clutter models through computer simulations. It is shown that the proposed algorithm can reliably detect the target even without a full knowledge of the transmit waveforms and in a variety of clutter conditions.

References

- [1] Digital Video Broadcasting (DVB), Frame structure channel coding and modulation for a second television broadcasting system (DVB- T2), European Telecommunications Standards Institute, European standard ETSI EN 302 755, Rev. V1.4.1 (2015-07), 2015.
- [2] Digital Video Broadcasting (DVB), Implementation guidelines for a second generation digital terrestrial television broadcasting system (DVBT2), European Telecommunications Standards Institute, ETSI TS 102 831, Rev. V1.2.1 (2012-08), 2012.
- [3] G. Cui, H. Li, and B. Himed, “A Correlation-Based Signal Detection Algorithm in Passive Radar with DVB-T2 Emitter”, The FortyEighth Asilomar Conference on Signals, Systems and Computers, Pacific Grove(CA), USA, 2-5 November 2014, pp. 1418-1422.
- [4] Matsuo Sekine, Yuhai Mao, Weibull Radar Clutter, London, UK: P.Peregrinus Ltd., 1990. ISBN 0863411916.
- [5] Vichet Duk, Diego Cristallini, Philipp Wojaczek and Daniel W. O’Hagan Statistical Analysis of Clutter for Passive Radar on an Airborne Platform 2019 International Radar Conference.
- [6] J. Barrie Billingsley, “Low angle radar land clutter” William Andrew Publishing, TK6580 .B45 2001.
- [7] D. O’Hagan, M. Setsubi and S. Paine, “Signal reconstruction of DVB-T2 signals in passive radar”, 2018 IEEE Radar Conference, 2018, pp. 1111-1116.
- [8] S. Cazalens, G. Lesthievant, B. Ros, and C. Boustie, “Theoretical study of P1 detection (synchronisation for DVB-T2 standard)”, in Proc. 36th Int. Conf. Telecommun. Signal Process. (TSP), Rome, Italy, Jul. 2013, pp. 249–253.

Hybrid model SARIMA-LSTM based on data decomposition by STL for prediction PM2.5 in central district in Hanoi

Nguyen Quang Dat¹, Do Duy Nhat²

⁽¹⁾ Hanoi University of Science, Vietnam National University, Hanoi, Vietnam

⁽²⁾ Le Quy Don Technical University, Hanoi, Vietnam

(1)nguyenquangdat@hus.edu.vn

(2)ddnhat@lqdtu.edu.vn

Hanoi has about 10 million citizens and is also the largest economic center in northern Vietnam. Hanoi's air quality has a direct effect on people's health, as well as the tourism of the 1000 years old capital. So, the government is carrying out adjustment on traffic in Hanoi, with over 500000 cars and 4 million motorcycles, it is one of the main reason for pollution in Hanoi. Therefore, the prediction of pollutants is an important issue in helping the government to make decisions on this problem. In this study, we propose a new hybrid model that combine from STL, SARIMA and LSTM (STL-SARIMA-LSTM) in order to replace the models are being used. The proposed model gave a very good accuracy when comparing with the Regression and Bi-LSTM are applied at present. The study proposed a feasible plan for traffic management, limiting vehicles during the rush hour, contributing to stabilizing and reducing air pollution in the urban area in Hanoi.

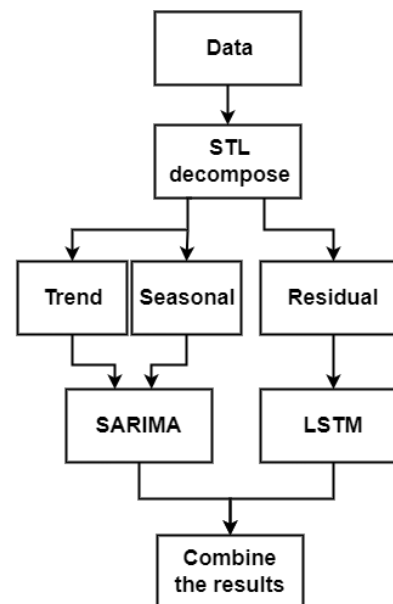
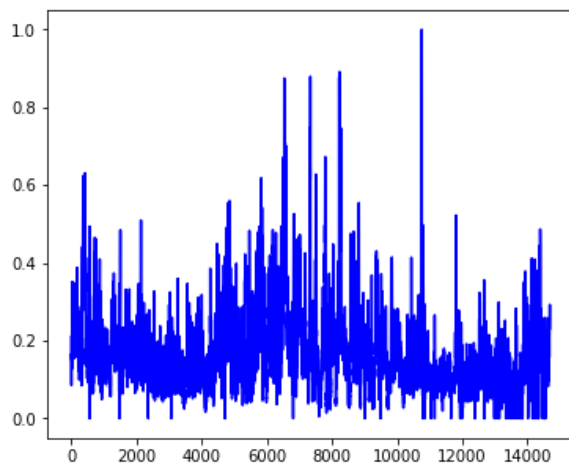


Fig 1: The dataset of PM2.5 at Cau Giay's station (Hanoi) and the proposed model to predict the PM2.5.

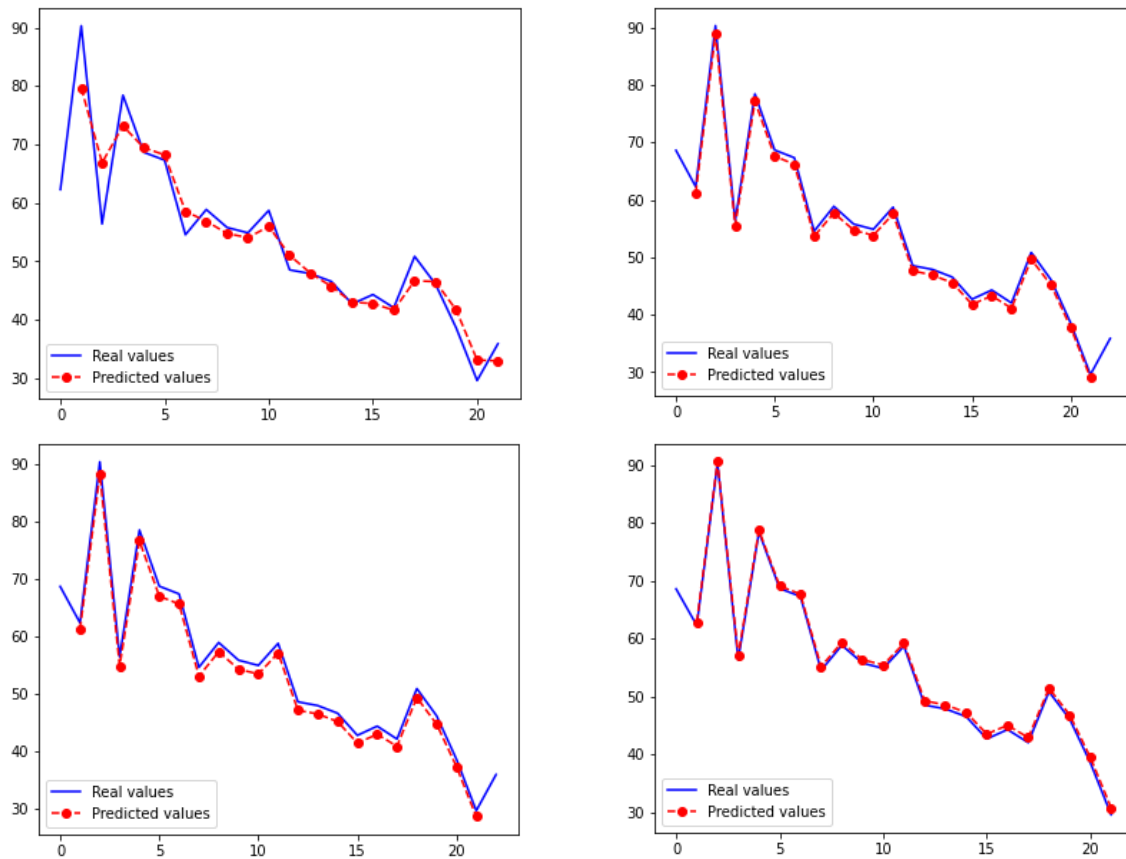


Fig 2: Results of the models for data of Cau Giay district: AR model (upper left), RNN model (upper right), LSTM model (lower left) and STL-SARIMA-LSTM model (lower right)

Table 1: the information on the result of the model after applying actual the data.

Model	MSE	MAPE	Note
AutoRegression	1.066325	0.501106	
RNN	0.683190	0.340086	<i>Hien's model</i> ¹
Bi-LSTM	0.632388	0.320123	<i>Thuan's model</i> ²
STL-SARIMA-LSTM	0.626369	0.312813	

¹ P.D. Hien, N.T. Men, P.M. Tan, M. Hangartner, "Impact of urban expansion on the air pollution landscape: A case study of Hanoi, Vietnam", *Science of The Total Environment*, Volume 702, 2020

² Nguyen Dinh, T., Phan Hoang, N. (2021). "Air Pollution Forecasting Using Regression Models and LSTM Deep Learning Models for Vietnam". In: Dang, T.K., Küng, J., Chung, T.M., Takizawa, M. (eds) "Future Data and Security Engineering. Big Data, Security and Privacy, Smart City and Industry 4.0 Applications". FDSE 2021. Communications in Computer and Information Science, vol 1500. Springer, Singapore

Title of Abstract: Acoustic, light-based Emergency Vehicle Detection using deep neural networks

Nguyen Quang Dat¹, Dineshwar Doddapaneni^{2a}, Vijender Kumar Solanki^{2b}, Do Duy Nhat³

¹Hanoi University of Science, Vietnam National University, Hanoi, Vietnam

²CMR Institute of Technology, Hyderabad

³Le Quy Don Tech. University, Hanoi, Vietnam

¹nguyenquangdat@hus.edu.vn, ^{2a}dineshsupertchno@gmail.com, ^{2b}spesinfo@yahoo.com, ³nhatdd@lqdtu.edu.vn

Nowadays vehicles are all present. The increase in the usage of vehicles has led to traffic jams across the globe. These jammed roads aren't too significant in general terms but could be a major problem for emergency services like ambulances, fire trucks, police vehicles ...etc. These emergency services are the ones that are most affected by traffic jams, as every second is valuable to lives at stake. Our main aim is to solve this problem using deep neural networks by feeding it with the sound of an ambulance and the light produced by it. These deep neural networks find the patterns of sound and light produced by an ambulance and use them to predict whether there is an ambulance or not. Basically, we are using a deep neural network as a classifier. Here we use the Mel spectrogram to convert the audio to useful data. The sound and light from a lane will be converted features and sent to a deep neural network which detects and gives the output of whether the vehicle is present or not. To collect the sound and light of vehicles we use photoelectric sensors and acoustic sensor/microphone and apply Mel spectrogram. Based on deep neural network output we take proper action.



Fig.1: The ambulance in traffic jam

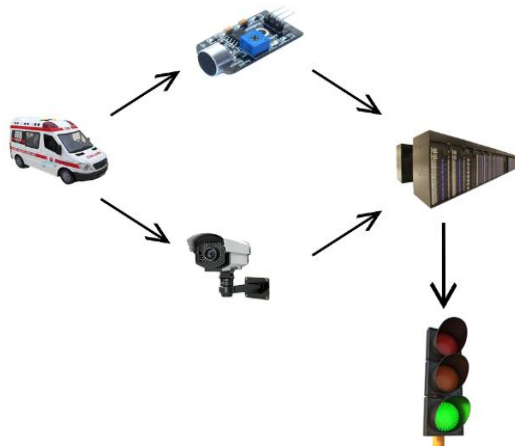


Fig. 2: Problem solving direction

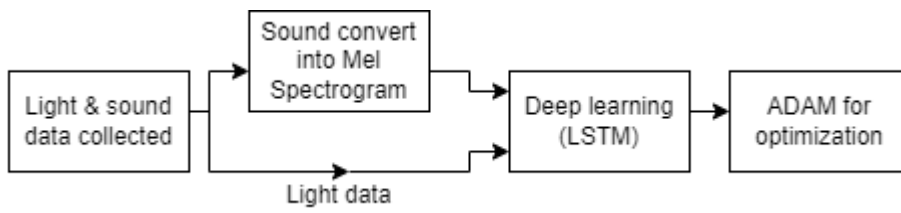


Fig. 3: Proposed method

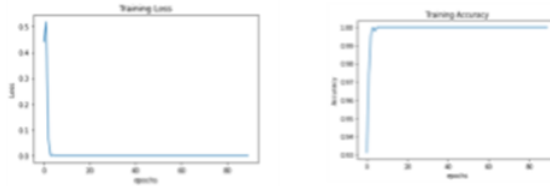


Fig. 4: The Accuracy and loss of model during training

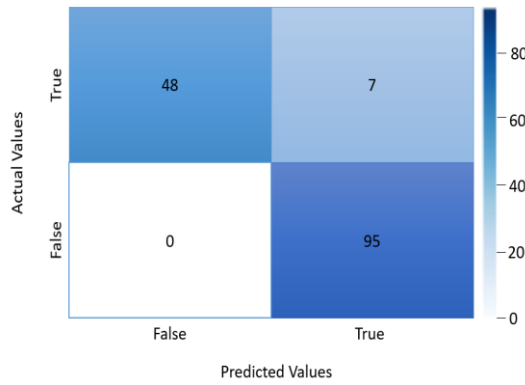


Fig 5: The result of LSTM optimization with ADAM

Preparation And Characterization of Activated Carbon from Coconut Shell Using Steam Activation

Kinkind Raras Heliani^{1,2}, Fitria Rahmawati^{1*}, Agung Tri Wijayanta³, Arika Fitonna Ridassepri⁴

¹Research Group of Solid State Chemistry and Catalysis, Chemistry Department, Sebelas Maret University, Indonesia

²Chemistry Department, Faculty of Mathematics and Natural Sciences, Sebelas Maret University, Indonesia

³Research Group of Sustainable Thermofluids, Mechanical Engineering, Sebelas Maret University, Indonesia

⁴Departement of Engineering Science, University of Electro-Communications, Japan

*Author to whom correspondence should be addressed:

E-mail: fitria@mipa.uns.ac.id

ABSTRACT

This research reports the potential of coconut shell, a solid waste which are abundantly available in tropical countries. Activated carbon based on coconut shell has been successfully synthesized using physical steam activation. The activation temperature is 700 °C, under steam flow of 200 mL/min. The prepared-materials were characterized by X-ray Diffraction (XRD), Fourier Transform Infrared (FTIR), Surface Area Analysis (SAA), and Scanning Electron Microscopy-Energy Dispersive X-Ray (SEM-EDX) to identify their crystal structure, functional group, surface area, morphology and elemental content. XRD analysis shows that the prepared-activated carbon is in amorphous phase with broad characteristic peaks at 2θ of 25° and 43°. Elemental analysis found that carbon (C), is the main content within the prepared-material, meanwhile oxygen (O), nitrogen (N), potassium (K), sulphur (S) sodium (Na), and silicate (Si) are also identified as minor content. The FTIR analysis shows the presence of C=C, -OH and C-O vibration as the specific functional groups found within activated-carbon. Surface area of the activated-carbon is also high, i.e., 816 m²/g due to the porous structure which was identified by SEM analysis. Impedance analysis followed by data fitting and conductivity calculation found $8.68 \times 10^{-2} \text{ S cm}^{-1}$ which is sufficient for some applications such as for electrode in electroanalysis or electrode for energy storage devices.

Introduction

In recent years, the increased development of industrial activities along with population growth around the world have triggered several environmental problems [1]. One of them is the use of energy sources that mainly come from non-renewable energy. The use of non-renewable energy can certainly cause problems such as greenhouse gases pollution, which caused global temperature increase and climate change. Therefore, it is important to move from non-renewable to renewable energy. Such as by using materials derived from biomass as a renewable resource [2].

Coconut shell is biomass which abundantly presence in Indonesia, up to 2.811.900 tons in 2020 [3]. Coconut shell is a potential raw material for activated carbon production, which can be applied in various fields such as for adsorbents [4], for anode materials for sodium ion batteries [2] and for electrodes on capacitors [5]. The main component contained in coconut shell is carbon 93.51%, oxygen 6.26%, and partly from inorganic impurities such as K, and Si (0.18 at% and 0.13 at%) [2]. The identified-elements are formed within some macromolecules such as pentose at 27.7%, cellulose 26.6%, lignin 29.4%, water 8%, extraction solvent 4.2%, uronate anhydrous 3.5%, and ash 0.6% [6]. The large carbon content within coconut shell ensure its high potential for activated-carbon production.

Experimental

1. Preparation of Coconut Shell Charcoal Waste

The coconut shell charcoal used was a solid waste of charcoal production (Klaten, Central Java, Indonesia). The coconut shell charcoal was chopped into small pieces, then crushed into powder in 100 mesh and then was washed and soaked in distilled water for 1 h, and stir it using magnetic stirrer then followed by drying at 60 °C for 1 h in an oven. The dry powder char was ready to be activated.

2. Synthesis of Activated Carbon

The produced char was activated by heating in furnace at 700 °C for 1 h with heating rate of 5 °C/min under steam flow. The activation was conducted within an installed-tube furnace as described in Fig. 1. Steam was produced by water which was boiled at 120 °C to produce steam, and then the steam flowed into furnace along with N₂ as gas carrier. The synthesized activated carbon was denoted as AC700.

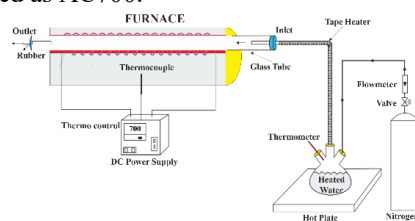


Fig. 1: Scheme of installed-tube furnace for the activation process

Result and Discussion

The XRD patterns of AC700 are displayed in Fig. 2. The XRD pattern shows a broad peak centered at $2\theta = 24^\circ$ corresponds to the (002) and 44° corresponds to the (100) crystal plane. Broad peaks confirm amorphous structure composed of randomly oriented aromatic graphene-like sheets (JCPDS no 41-1487).

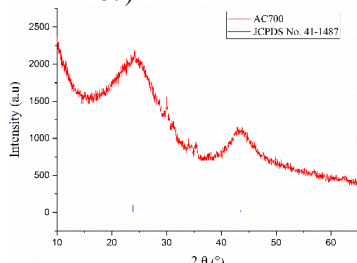


Fig. 2: XRD spectra of AC700

The FTIR transmission spectra of AC700 is shown in Fig. 3 which exhibit some peaks including a broad peak at 3329 cm^{-1} belong to O-H stretching. A peak at 2315 cm^{-1} represents the N-H stretching. The C=C stretching at 1534 cm^{-1} refers to the presence of aromatic ring. Fig. 3 shows that the activation process removes the C=O peak, indicating thermal decomposition of aldehyde and ketone group in coconut shell. The intensity of C-O vibration peak at 1010 and 1098 cm^{-1} increases in AC700. In addition, some small peaks of surface aromatic -CH groups are also reveal in between 500 and 898 cm^{-1} .

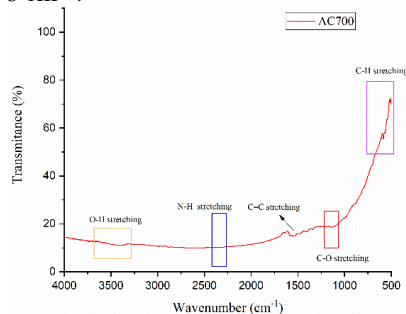


Fig. 3: FTIR spectra of AC700

The SEM images of AC700 is clearly show large wall-mounted tube structure with very low content of sheet particles. This is because ash and disorganized carbon, which formed from decomposition of organic matter and blocked the pores and tube structures were washed out by steam activation and the activated carbon surface to become smooth, wrinkled, and exhibiting open holes. The EDX result shows that AC700 contained of 49.6% of carbon as the main content, and oxygen, nitrogen, potassium, sulphur, sodium, and silicate at 32.42%, 10.68%, 2.48%, 1.29%, 0.79%, and 0.84%, respectively, as minor contents.

The adsorption isotherm (Fig. 5) shows that the N_2 adsorption-desorption isotherm in AC700 follows type I. Type I isotherm is belonged to microporous ($< 2\text{nm}$) materials with narrow pore size distribution. In addition AC700 has a H4 type

of hysteresis loop. The H4 hysteresis loop is usually provided by porous material consisting narrow pore channels from microporous carbon. The BET specific surface area of AC700 is $816.3\text{ m}^2/\text{g}$. Which is higher than the other results produced by a different activation method [7].

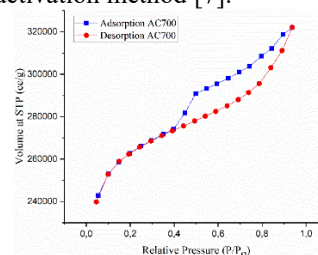


Fig. 5: Nitrogen adsorption – desorption isotherm of AC700

Conductivity of the AC700 was measured by impedance measurement resulting Nyquist plot as depicted as shown in Fig. 6. The plot was fitted by applying RL network as inserted in Fig 6. Fitting resulted resistance, R value of 11,41 Ohm. Electrical conductivity as calculated from R value is $8.68 \times 10^{-2}\text{ S cm}^{-1}$.

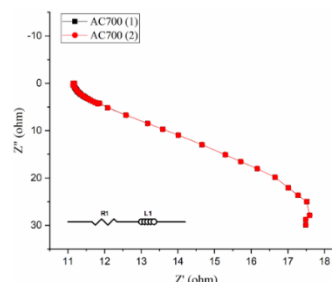


Fig. 6: Nyquist plots of AC700

Conclusion

Activated-carbon can be produced from coconut shell by steam activation. The activation successfully increased surface area and pore volume of the carbon. The steam activation removed C=O vibration indicating thermal decomposition of aldehyde and ketone group in coconut shell. The activated carbon AC700 provides a high electrical conductivity of $8.68 \times 10^{-2}\text{ S cm}^{-1}$.

References

- [1] S. Chen *et al.*, 2020, *Electrochim. Acta*, **346**, p. 136239.
- [2] C. Nita, B. Zhang, J. Dentzer, and C. Matei Ghimbeu, 2021, *J. Energy Chem.*, **58**, pp. 207–218.
- [3] “Badan Pusat Statistik,” 2020.
- [4] W. Widiyastuti, M. Fahrudin Rois, N. M. I. P. Suari, and H. Setyawan, 2020, *Adv. Powder Technol.*, **31**, no. 8, pp. 3267–3273.
- [5] S. C. G.-T. P. and C.-M. H. Kuan-Ching Lee, Mitchell Shyan Wei Lim, Zhong-Yun Hong, 2021, *Energies*, **14**, no. 15, p. 4546.
- [6] W. A. Rizal *et al.*, 2020, *IOP Conf. Ser. Earth Environ. Sci.*, **462**, no. 1.
- [7] E. H. Sujiono *et al.*, 2022, *Results Chem.*, **4**, p. 100291.

NUMERICAL INVESTIGATION ON HEAT TRANSFER COEFFICIENT OF TiO₂-CNTs/WATER NANOFLUIDS

Sukmo Utomo Abdillah Amin¹, Budi Kristiawan¹, Koji Enoki², Wibawa Endra Juwana¹, Agung Tri Wijayanta¹

¹Mechanical Engineering, Universitas Sebelas Maret, Jl. Ir. Sutami 36A Kentingan, Surakarta 57126, Indonesia

²Department of Mechanical and Intelligent Systems Engineering, The University of Electro-Communications, 1-5-1 Chofugaoka, Chofu, Tokyo 182-8585, Japan

(budi_k@staff.uns.ac.id; enoki.koji@uec.ac.jp; agungtw@uns.ac.id; sukmo@student.uns.ac.id)

ABSTRACT

Nanohybrid fluid technology has had a positive effect on increasing the value of the heat transfer coefficient. This study investigated numerically the effect of adding nanohybrid particles into the base fluid on the increase in the heat transfer rate in a concentric tube heat exchanger. The results showed that adding nanohybrid particles into the base fluid significantly increased heat transfer.

Keywords: Nanohybrid, heat transfer, TiO₂, CNTs

1. INTRODUCTION

The development of advanced technology like humans work dynamically, effectively, and efficiently particularly in the enhancement of the thermal system efficiency was very important currently. Factors affecting the change in the heat transfer coefficient of nanofluids include nanoparticle conductivity, viscosity, and nanofluid factors. Choi first proposed the concept of nanofluids in 1995. Kristiawan et al. (2020)¹ investigated the effect of adding TiO₂ nanoparticles to a water-based liquid with a volume concentration of 0.05 - 0.30 vol%. The results show that the heat transfer coefficient of the nanofluid is higher than the coefficient of the base fluid¹.

In some cases, combining two materials is expected to produce a product with superior properties compared to the individual components². Research using hybrid nanofluids has also been carried out by other researchers^{3,4,5}. Recently, several new studies have been carried out on the thermal performance of nanofluid CNTs⁶.

This study examines the increase in heat transfer coefficients in nanofluid TiO₂/water and nanohybrid TiO₂-CNTs/water in plain concentric tube heat exchangers.

2. METHODOLOGY

The heat transfer fluid in the form of a nanohybrid fluid has better thermophysical properties than a single nanofluid or conventional heat transfer fluid. This study numerically determines the convective heat transfer of nanohybrid fluids TiO₂-CNTs/water and TiO₂/water through a double heat

exchanger depicted in 3D using Ansys simulation software. The nanofluid flow was simulated by the k-ε RNG turbulence model using a single-phase model as nanofluids. Properties of a pipe material is copper. The horizontal pipe has a length of 414 mm with a diameter of 5.32mm. The simulation was run using a hot fluid with a shell velocity of 1.58 m/s and a temperature of 50°C for a cold fluid of 15°C with a flow in the counter flow. Nanoparticles concentrations of TiO₂/water and TiO₂-CNTs/water were 0.1vol.%, respectively. Reynolds number was varied in turbulent flow between 5000-10000.

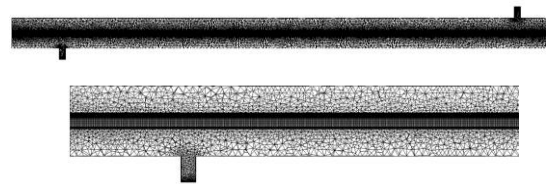


Fig.1: The Numerical model

3. DATA PROCESSING

Convective exchange of thermal energy

The exchange of thermal energy or heat-transfer rate (Q) determined by an energy-balance equation on the hot water and nanofluid sides can be expressed as follows.

$$Q_w = \dot{m}_w C_{pw} (T_{out} - T_{in})_w \quad (1)$$

$$Q_{nf} = \dot{m}_{nf} C_{nf} (T_{out} - T_{in})_{nf} \quad (2)$$

The whole heat transfer coefficient (U) in the inner tube is expressed as follows.

$$U = \frac{Q_{cold}}{A_i \Delta T_{LMTD}} \quad (3)$$

The log mean temperature difference is given as shown below.

$$\Delta T_{LMTD} = \frac{(T_{nf,in} - T_{w,out}) - (T_{nf,out} - T_{w,in})}{\ln \frac{(T_{nf,in} - T_{w,out})}{(T_{nf,out} - T_{w,in})}} \quad (4)$$

Heat-transfer coefficient (h) on the annulus side was computed

$$h_o = \frac{Q_{hot}}{A_o (T_{wo} - T_{wi})} \quad (5)$$

The convective heat-transfer coefficient of the tube (h) is formulated as follows

$$h_i = \frac{1}{\left(\frac{1}{U} - \frac{d_o \ln \left(\frac{d_o}{d_i} \right)}{2k_{cu}} - \frac{d_i}{d_o h_o} \right)} \quad (6)$$

To ensure the accuracy of the resulting simulation, the results of the Nusselt number are compared with the results of the well-known correlation from the Dittus-Boelter equation⁷ and friction factor results are compared from Petukhov equation⁷.

$$Nu = 0,023 Re^{0,8} Pr^{\frac{1}{3}} \quad (7)$$

$$f = (0,79 \ln Re - 1.64)^{-2} \quad (8)$$

4. RESULTS AND DISCUSSION

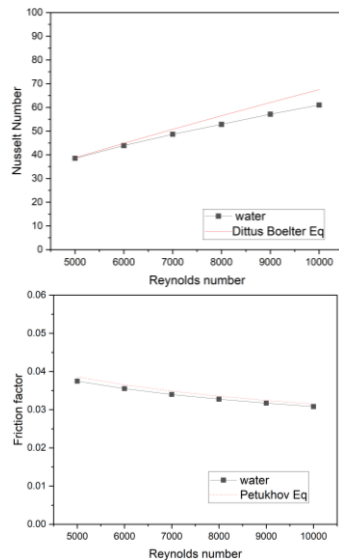


Fig.2: The validation of numerical results with Dittus Boelter equation for Nusselt number and Petukhov correlation for friction factor

Figure 2 shows that the numerical simulation results tend to follow the Dittus-Boelter and Petukhov equation [7] with an error percentage of less than 5%. Therefore, the simulation can be stated to be valid for later modelling and can be used in simulations using hybrid nanofluids.

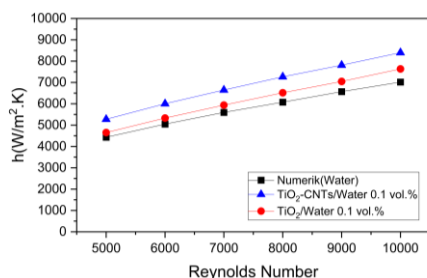


Fig.3: Result of heat transfer coefficient

The results showed an increase in heat transfer occurred when hybrid nanoparticles were added. The increased heat transfer occurred as the Reynolds number increased. TiO₂-CNTs/Water hybrid nanoparticles volume fraction 0.1% has an excellent heat transfer performance compared to water. This is indicated by the heat transfer coefficient which increases to 19.12% in a turbulent flow. The addition

of CNTs also causes an increase in the heat transfer coefficient by 11.69%. The use of nano-hybrid fluids is more efficient than the use of water-based fluids and single nanofluids. This is because the increased heat transfer is incredible and results in a more significant Nusselt number.

5. CONCLUSION

The heat transfer coefficient increases as the Reynolds number increases. The use of hybrid nanofluids has a high heat transfer coefficient compared to the use of water base fluids and single nanofluids. It can be concluded that the addition of CNTs to the TiO₂/water nanofluid can increase the heat transfer coefficient.

6. ACKNOWLEDGEMENTS

This work supported by the Institute of Research and Community Service of Universitas Sebelas Maret, Surakarta, Indonesia (LPPM UNS) in Penelitian Dasar Unggulan Perguruan Tinggi (PDUPT) with grant number: 054/E5/PG.02.00.PT/2022 and No. 254/UN27.22/PT.01.03/2022.

7. REFERENCES

- Kristiawan B, Rifa'i AI, Enoki K, Wijayanta AT, Miyazaki T. Enhancing the thermal performance of TiO₂/water nanofluids flowing in a helical microfin tube. *Powder Technol.* 2020;376:254-262. doi:10.1016/j.powtec.2020.08.020
- Arimi A. Investigation of Laminar Convective Heat Transfer of a Novel Tio 2 – Carbon Nanotube Hybrid Water- Based Nanofluid. 2017;(January 2015). doi:10.1080/08916152.2014.973974
- Madhesh D, Parameshwaran R, Kalaiselvam S. Experimental investigation on convective heat transfer and rheological characteristics of Cu-TiO₂ hybrid nanofluids. *Exp Therm Fluid Sci.* 2014;52:104-115. doi:10.1016/j.expthermflusci.2013.08.026
- Ramadhan AI, Azmi WH, Mamat R, Hamid KA. Experimental and numerical study of heat transfer and friction factor of plain tube with hybrid nanofluids. *Case Stud Therm Eng.* 2020;22(October):100782. doi:10.1016/j.csite.2020.100782
- Ghashim SL. A mathematical analysis of nanoparticles on heat transfer in a circular pipe. *Case Stud Therm Eng.* 2021;28(June):101524. doi:10.1016/j.csite.2021.101524
- Chougule SS, Nirgude V V., Gharge PD, Mayank M, Sahu SK. Heat Transfer Enhancements of Low Volume Concentration CNT/Water Nanofluid and Wire Coil Inserts in a Circular Tube. *Energy Procedia.* 2016;90(December 2015):552-558. doi:10.1016/j.egypro.2016.11.223
- Cengel JCYA. Momentum analysis of flow systems. *Fluid Mech Fundam Appl.* Published online 2013:227-268.

Vietnamese Sign Language Recognition using Mediapipe and Deep Learning

Nghia Cao Xuan, Quang Nguyen Van and Trong Thanh Han

Hanoi University of Science and Technology

nghia.cx193040@sis.hust.edu.vn , quang.nv193069@sis.hust.edu.vn and thanh.hantrong@hust.edu.vn

ABSTRACT

Sign language was invented to help deaf people communicate with each other and with everyone. This paper proposes a method to recognize Vietnamese Sign Language based on detecting skeletal points on the hand through Mediapipe. Since then, the Convolutional Neural Network is used to classify the hand symbols. The obtained results have an accuracy of 96.78% on the training dataset and 96.9% on the test dataset.

Keywords: computer vision, deep learning, Mediapipe, Vietnamese Sign language.

INTRODUCTION

Sign language was invented to help deaf and dumb people communicate with people. Recognition of sign languages helps to bridge the gap between deaf and normal people. A sign language consists of signs formed by 4 main components: hand shape, position in relation to the body, movement of the hand, orientation of the palm.

There are two main types of gestures in sign languages: static and dynamic. Static gestures are represented as still images. Dynamic gestures are displayed in videos that contain a series of frames (still images). In this paper, we propose a sign language recognition system for input video processing with 2 main stages: video pre-processing and deep learning. The preprocessing stage is to identify the object performing the sign in the video frames, from which to extract the skeleton points on the hand (keypoints) through the Mediapipe tool (a library developed by Google Developers) , and the coordinates of the keypoints are saved as csv file. Then, in the classification and deep learning phase, we build a CNN model to recognize the hand symbols.

METHOD AND RESULT

First, we propose an input video processing system with 2 main stages: preprocessing and deep learning. In the preprocessing stage, keypoints will be extracted from the sign language objects in the video. After, the hand symbols will be classified through CNN models.

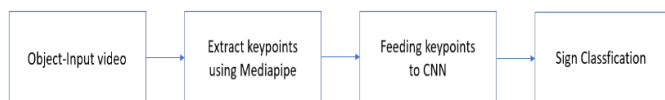


Fig 1. Deep Learning Processing

Stage 1: Get coordinates of keypoints according to the mechanism described in figure 2.

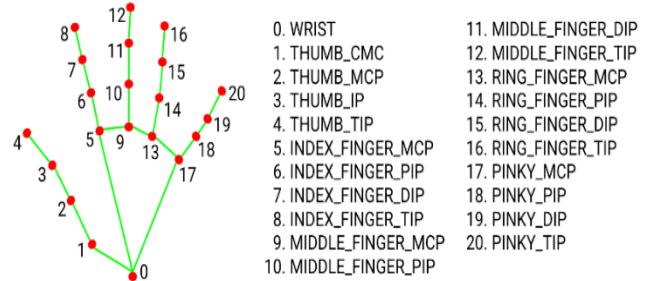


Fig 2. Coordinates of skeleton points (keypoints) according to Mediapipe Hands

Stage 2: After obtaining the coordinates of the keypoints on the hand, the data coordinates of the collected keypoints will be converted into coordinates relative to the origin of the skeleton (Point 0), from which flatten to a one-dimensional array and finally normalize to the maximum value as shown in figure 3.

Landmark Coordinates										
ID : 0	ID : 1	ID : 2	...	ID : 19	ID : 20					
[550,450]	[485,430]	[430,380]	...	[687,225]	[702,192]					
Convert to relative coordinates from ID : 0										
ID : 0	ID : 1	ID : 2	...	ID : 19	ID : 20					
[0,0]	[65,-20]	[-120,-70]	...	[137,-225]	[152,-258]					
Flatten to a one-dimensional array										
ID : 0	ID : 1	ID : 2	...	ID : 19	ID : 20					
0	0	65	-20	-120	-70	...	137	-225	152	-258
Normalized to the maximum value										
ID : 0	ID : 1	ID : 2	...	ID : 19	ID : 20					
0	0	0.25	-0.08	-0.47	-0.27	...	0.53	-0.87	0.59	-1

Fig 3. Coordinates of skeleton points after normalization

The normalized coordinates will be added to the csv file in the following format: the first column will be the id of n hand symbols (which are assigned from 0 to n-1), the next columns will be respectively normalized coordinates as shown above.

Next, we build a model to recognize the hand symbols that appear in the video. This model is built by a combination of Mediapipe and CNN. We build CNN model with 5 layers: Sequence layer, Dropout layer, Fully Connected layer, Softmax layer and Classification layer.

CONCLUSION

The CNN model uses the 'Adam' optimization function and uses the 'Sparse_categorical_crossentropy' loss function. It reduces the complexity of the learning process, helps the learning model to converge faster and gives more accurate results.

Fig 4 shows the accuracy and loss of the training and test sets while training the model.

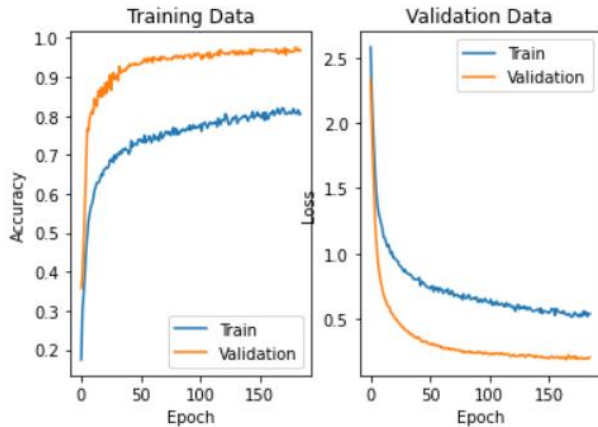


Fig 4. . Accuracy and loss of training and test sets

After finishing training, the model achieved high accuracy on the training set of 96.78%. We use this model to test with our test dataset, the accuracy is 96.9%.

There are 1033/1066 correctly identified labels. Only 33/1066 misidentified labels scattered among the labels 'Xin Chao', 'Tam biet', 'Im lang', are shown in Figure 5 below.

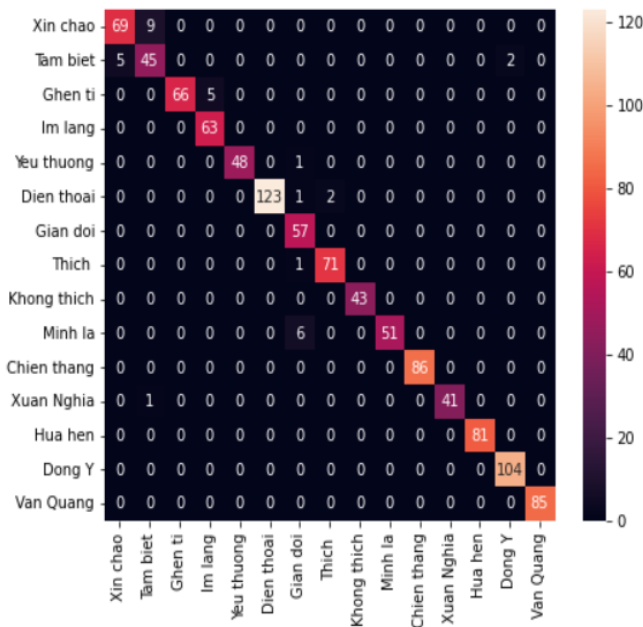


Fig 5. Result of the model with the test dataset

In this paper, we have presented an approach to Vietnamese sign language using deep learning and Google Mediapipe library to extract skeletal coordinates in the hand.

The extraction of skeleton coordinates depends on the styling difficulty of that sign language, the distance from the camera to the hand as well as the full brightness, ... In the rest of the work, our model reached accuracy high accuracy of 96.78% on the training set and 96.9% on the test set.

REFERENCES

- [1] S. Thylashri; D. Femi; V. Jawahar; D. Santhakumar; Y. V Rakesh Reddy, "Human Sign Language Recognition Using Deep Learning" 2022 International Conference on Innovative Computing, Intelligent Communication and Smart Electrical Systems (ICES)
- [2] Ahmed Hassan; Ahmed Elgabry; Elsayed Hemayed, "Enhanced Dynamic Sign Language Recognition using SlowFast Networks", 2021 17th International Computer Engineering Conference (ICENCO)
- [3] K Amrutha; P Prabu "ML Based Sign Language Recognition System", 2021 International Conference on Innovative Trends in Information Technology (ICITIIT)
- [4] Edwin Escobedo; Lourdes Ramirez; Guillermo Camara, "Dynamic Sign Language Recognition Based on Convolutional Neural Networks and Texture Maps" , 2019 32nd SIBGRAPI Conference on Graphics, Patterns and Images (SIBGRAPI)
- [5] Surejya Suresh; Haridas T.P. Mithun; M.H. Supriya, "Sign Language Recognition System Using Deep Neural Network" 2019 5th International Conference on Advanced Computing & Communication Systems (ICACCS)
- [6] P.T.Hai, H.C. Thinh, B.Van Phuc, and H. H. Kha, "Automatic feature extraction for Vietnamese sign language recognition using support vector machine," in 2018 2nd International Conference on Recent Advances in Signal Processing, Telecommunications & Computing (SigTelCom). IEEE, 2018, pp. 146-151.

Online deep neural networks model based multi seasonal decompose for short-term electricity load forecasting

Nguyen Quang Dat

Hanoi University of Science, Vietnam National University, Hanoi, Vietnam

nguyenquangdat@hus.edu.vn

Electricity load of a residential area is a very important indicator, because it directly affects people's lives and the operation of the economy in that area. Therefore, forecasting the electricity load index in the short term is an important issue. And especially, in the short-term forecast, the fact that the data is updated in the latest time has a great influence on the forecast values. At the same time, in the electricity load data, it is worth noting that there are many sequences that coexist in the data: repeating at each hour in the day, repeating at each day of the week, etc. In this study, the author proposed to use deep learning model based on online learning method, in order to take full advantage of the properties of the new value of the data, which are continuously updated in the input time series. Also use multi-season method based on Fourier formula to take full advantage of multi-season in real data. Since then, this study propose a machine learning model that combines online machine learning model and multi-season time series model. The proposed Fourier - Online NN method has been applied on the actual data of the electricity load time series of northern Vietnam, giving better short-term forecasting results than traditional SARIMA method (Seasonal model) and traditional deep learning methods (Neural Network).

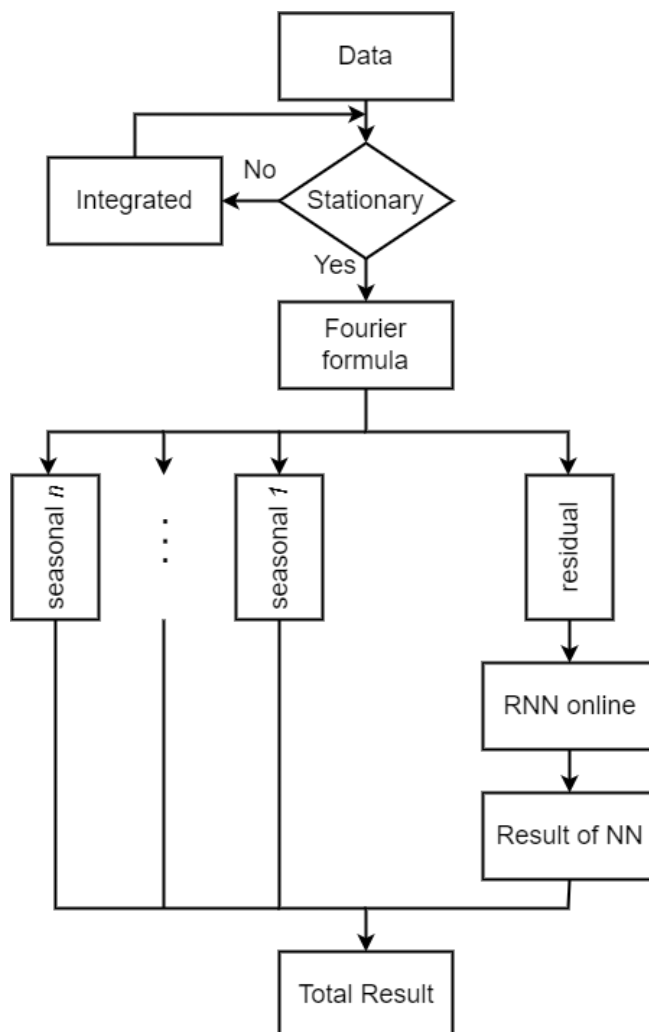


Fig.1: Proposed model that combine by Fourier formula and RNN online.

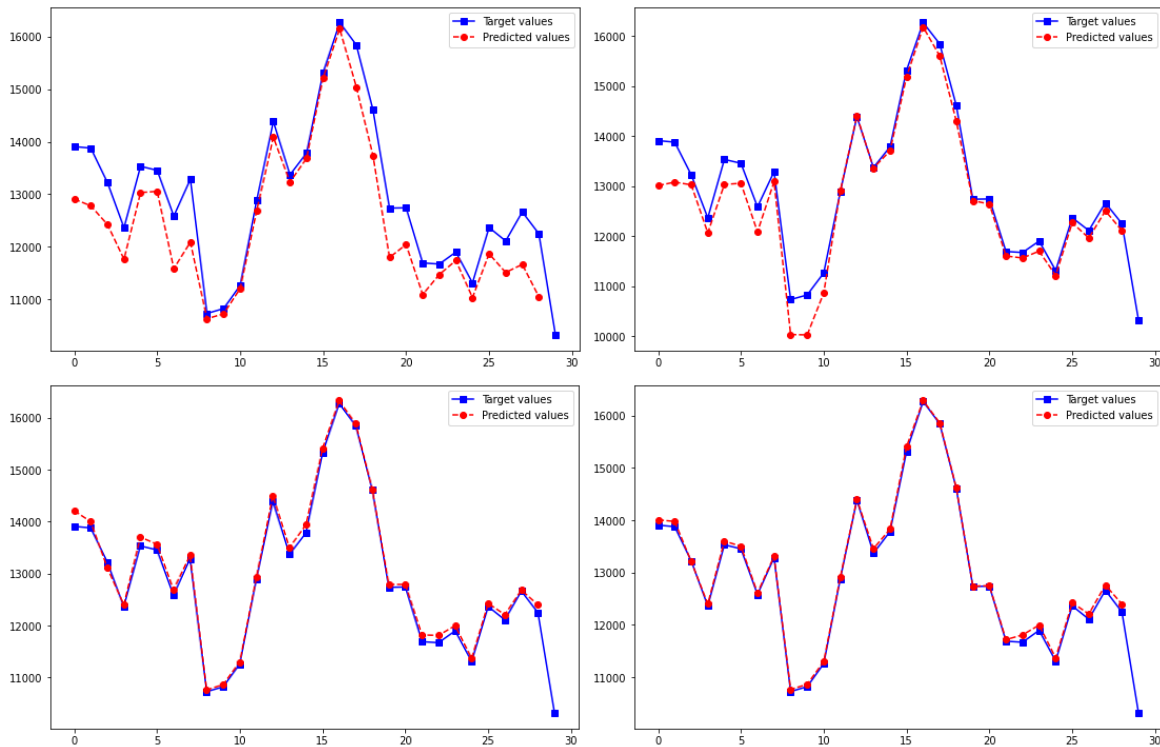


Fig 2: The result of several models: SARIMA (upper-left), RNN (upper-right), RNN online (lower-left) and proposed model Fourier-RNN online (lower-right). There are the first 30 values of the results.

SARIMA – Seasonal Auto-Regressive Integrated Moving Average model

RNN – Recurrent Neural Networks model

Fourier – Fourier Transform

Model	MSE	MAPE	Note
SARIMA	1491596.02	10.008377 %	
RNN	991287.60	4.243678 %	
Online learning ⁽¹⁾	989699.14	4.048132 %	<i>Rebuild</i>
Proposed model	981031.30	3.512340 %	

Tab. 1: The result of the proposed model

MSE – Mean Squared Error

MAPE – Mean Absolute Percentage Error

$$MSE = \frac{1}{n} \cdot \sum_{i=1}^n (\hat{y}_i - y_i)^2 \quad MAPE = \sum_{i=1}^n \left| \frac{\hat{y}_i - y_i}{n} \right|$$

¹ N.M. Vural et al. “Achieving Online Regression Performance of LSTMs with Simple RNNs”, arXiv:2005.08948v2, 2021.

Denoising methods for non-profile the side channel attack in hardware security evaluation

Phu-Cuong Le, Van-Nam Le, Ngoc-Tuan Do and Van-Phuc Hoang

Le Quy Don Technical University, Hanoi, Vietnam

Email: laphucuongtmta@gmail.com

ABSTRACT

In security devices, encryption algorithms can be implemented either as software or as hardware. However, the calculations of the algorithm are performed partially or completely on integrated circuits. Therefore, they often leak information related to algorithm execution such as power consumption, electromagnetic signal, running time, etc. which make the side channel attack possible. However, the side channel power consumption data used in the actual attack usually contains a lot of noise, which greatly reduces the success rate of attacks. In this paper, the authors investigate denoising methods applied in non-profile side channel attack. Thereby giving the results and commenting on the effectiveness of each method. To verify the performance of each method, the authors choose the correlation power analysis (CPA) method to attack. The effectiveness comparison is assessed by the success rate of the attack. Using methods, we obtained a significant reduction of the noise effect.

Keywords: Side channel attack; power consumption; wavelet denoising; PCA denoising; VMD denoising.

1. INTRODUCTION

Along with the strong development of the 4th industrial revolution, integrated circuits are being widely used in all areas of human life. More and more important data is stored and processed on integrated circuits. Therefore, ensuring the integrity, authenticity and confidentiality of data becomes extremely urgent. Encryption algorithm is a commonly applied solution today to ensure the security of electronic devices. Although designed to resist algorithmic attacks, encryption algorithms are implemented on hardware systems, which means they can be analyzed against side-channel leak data such as timing [1], power consumption [2], electromagnetic signal [3] and sound [4]. Side channel attacks (SCA) are attacks that use leaked information to retrieve data, such as secret keys. Among the attacks, the power analysis attack, which uses the instantaneous power consumption of cryptographic devices, is a very useful type of attack. Power consumption analysis exploits the relationship between the information contained within the device and the actual power consumed by the encoder. Differential power analysis (DPA) [2] is a type of initial power analysis attack. Later, it was extended to become more efficient, which is the CPA power consumption correlation analysis technique [5]. The CPA

technique exploits the correlation between the actual power consumption and the power consumption model inferred from the encryption algorithm, thereby predicting the secret key.

Currently, there are many research on side channel attacks. However, practice shows that when collecting information about the side channel, it is always affected by noise. This noise source can be caused by a number of reasons such as the noise source of the device itself, from the external electromagnetic interference environment, or it can be due to measures against attack by jamming. Noise is an important factor affecting the success rate of side-channel attacks. Many methods to perform filtering and noise reduction are proposed to improve the attack efficiency [6],[7]. The simplest is to average the leaks. However, the trace count requirement does not always meet the practical requirement.

This paper evaluates some noise reduction methods which are also considered as preprocessing techniques for side channel attack. Thereby contributing to improving the efficiency of side-channel attack risk assessment. The noise filtering techniques are: wavelet transform (WT: Wavelet Transform) [6], variable mode decomposition technique (VMD: Varitional Mode Decomposition) [7], principal components analysis (PCA: Principal Components Analysis)) [8]. From there, the evaluation and conclusions for each method are given.

2. PRACTICAL EXPERIMENTS

A. Experiments Setup

To evaluate the denoising ability as well as compare the effectiveness of the above denoising methods, the authors perform CPA attack. The noise used here is Gaussian noise with a ratio of SNR = 4 (strong noise) added to the power tracks to ensure generalizability. Theoretically, the larger the number of traces used, the more effective the attack. However, the attacker does not always have enough data to attack. Therefore, the criterion to compare these denoising methods is that the number of traces used to attack is the least so that the attack efficiency is highest.

B. Experiments Results and Analysis

The results of the success rate using denoising methods WT, PCA, VMD and not using denoising method are shown in Figure 3. It can be seen that the denoising techniques are much more effective when no denoising is applied in the attack.. Specifically, with a sufficiently large

amount of traces (500 traces) without noise filtering, the successful attack rate is only 34% while applying the main component analysis technique PCA this rate is 92%. , and is 98% when applying wavelet technique. Similarly, to achieve a successful attack rate of 80%, when applying wavelet transformation, the number of traces used is only 350 traces, when using PCA technique is 430 traces and when no noise filtering is used, the number of traces used is 430 traces and without filtering out noise, 700 traces are required to achieve this ratio.

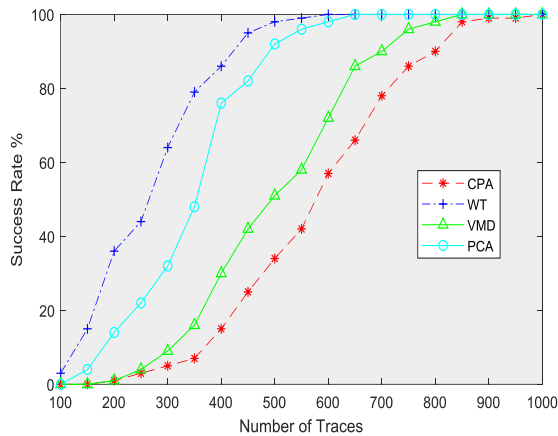


Figure 1. Success rate of CPA using different denoising methods.

The wavelet denoising technique gives the best performance compared to the remaining denoising techniques because, for the wavelet noise reduction technique, the denoising ability depends on the choice of the wavelet basis function. This selection is based on the form of the target signal, when choosing the most suitable basis function for the target signal will improve the noise filtering efficiency.

Next, the authors compare the Pearson correlation of the denoising techniques. For the same sample as the correct key, wavelet transform gives the highest output CPA level, followed by PCA and VMD techniques. Where there is the greatest correlation of method techniques are the correct keys to look for.

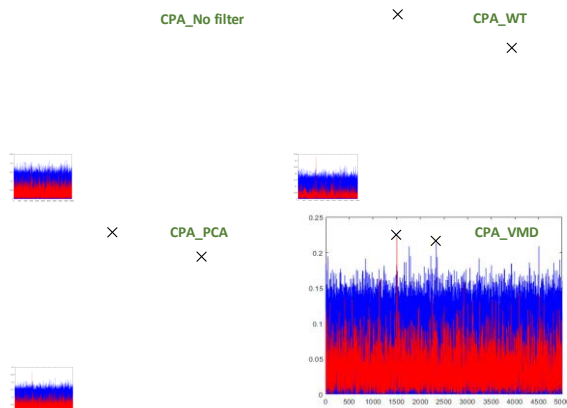


Figure 2. Correlation value using different denoising methods.

Also from Figure 4 shows that, when no denoising methods are applied, the output CPA is very low (approximately 0.2) and the CPA of the correct key and the wrong key are mixed, so it is difficult to find the right key. When applying denoising techniques such as VMD or CPA, now the output CPA has increased (CPA of correct key when applying PCA noise filter is 0.27) and there is a significant difference between the maximum CPA of the correct key and the correct wrong key. In particular, when applying wavelet transform to filter noise, the maximum CPA for the correct key is 0.34 and there is a clear difference between the correct key CPA and the wrong key.

3. CONCLUSIONS

In this paper, the authors have investigated denoising techniques in side-channel attacks and evaluated the effectiveness of each method. Specifically, the authors investigated three typical denoising methods such as wavelet transform, VMD denoising technique and PCA denoising technique. The results confirm that the attack efficiency is significantly improved when applying denoising methods in SCA side channel attacks. The results also show that the successful attack rate (success rate) of the wavelet denoising method gives the highest efficiency. In the future, the authors will also research and propose methods to further improve the noise filtering ability of wavelet transform techniques in side-channel attacks.

4. REFERENCES

- [1] P. C. Kocher, "Timing attacks on implementations of Diffie-Hellman, RSA, DSS, and other systems," in *Advances in Cryptology—CRYPTO'96*, 1996, pp. 104-113.
- [2] P. Kocher, J. Jaffe, and B. Jun, "Differential power analysis," in *Advances in Cryptology—CRYPTO'99*, 1999, pp. 388-397.
- [3] D. Agrawal, B. Archambeault, J. Rao, and P. Rohatgi, "The EM Side-Channel (s): Attacks and Assessment Methodologies," *Internet Security Group, IBM Watson Research Center*, ps, vol. 2, 2002.
- [4] D. Genkin, A. Shamir, and E. Tromer, "RSA key extraction via low-bandwidth acoustic cryptanalysis," in *Advances in Cryptology—CRYPTO 2014*, ed: Springer, 2014, pp. 444-461.
- [5] E. Brier, C. Clavier, and F. Olivier, "Correlation power analysis with a leakage model," in *Cryptographic Hardware and Embedded Systems—CHES 2004*, ed: Springer, 2004, pp. 16-29.
- [6] Jun Li, Shaoqing Li, Yobo Shi, Errui Zhou, "Wavelet de-nosing method in the side-channel attack" in *2015 IEEE International Conference on Signal Processing, Communications and Computing (ICSPCC)*, 2015.
- [7] Juan Ai; Zhu Wang; Xiping Zhou; Changhai Ou, "Variational mode decomposition based denoising in side channel attacks" in *2016 2nd IEEE International Conference on Computer and Communications (ICCC)*, 2016.
- [8] Eleonora Cagli, Cécile Dumas, Emmanuel Prouf, "Enhancing Dimensionality Reduction Methods for Side-Channel Attacks" in *Homma, N., Medwed, M. (eds) Smart Card Research and Advanced Applications. CARDIS 2015*.

High-order Chebyshev Notch Filter based on MO-OTA

Siradanai Srisamranrungrueang , and Natapong Wongprommoon

Department of Electrical Engineering, Faculty of Engineering and Industrial Technology, Silpakorn University, Nakhon Pathom 73000, Thailand

wongprommoon_n@su.ac.th

Abstract

This paper presents a high-order notch filter based on multiple output OTA (MO-OTA). The signal flow graph (SFG) method is applied as a design procedure based on the RLC prototype. The RLC Chebyshev low-pass filter is used as an original prototype. The network transform is applied to convert the LPF to a notch filter. From the SFG, the denormalized network can be replaced by integrators and differentiators. The current-mode lossy and lossless types of integrator and differentiator are realized by using CMOS MO-OTA and grounded capacitor. A simple and low-complexity structure is achieved and constructed by 9 MO-OTAs and 6 grounded capacitors. The stop-band frequency between 10Hz- 1kHz can be electronically tuned by the bias current between 1-100 μ A. The low power supply ± 0.75 V is required which consumes the power 15mW at 100 μ A bias current. An application in ECG signal with power line interference (PLI) removal is included.

Design and Methodology

There are many ways to realize the notch filter. This paper used the RLC basis due to the relatively low-sensitivity and rather high-performance. The transformed RLC notch filter is shown in Fig 1.

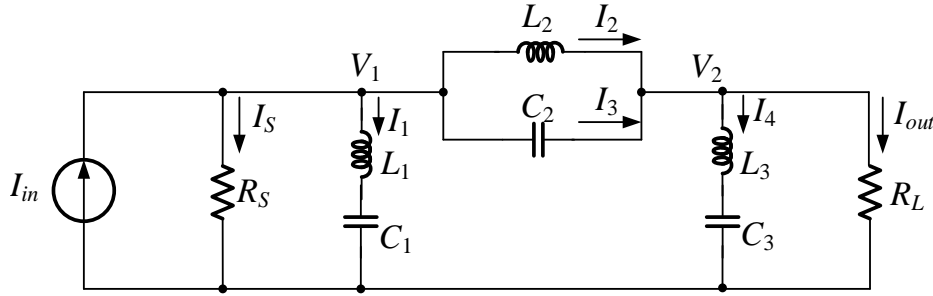


Fig.1: RLC Chebyshev ladder notch filter prototype

Using KCL in Fig.5, the current and voltage relationships of each designated nodes or branches can be written as (1)-(8)

$$I_1 = I_{in} - I_S - I_2 + I_3 \quad (1)$$

$$I = V_1/R_S \quad (2)$$

$$V_1 = I_1(sL_1 - \frac{1}{sC_1}) \quad (3)$$

$$(I_2 + I_3) = (V_1 - V_2)(\frac{1}{sL_2} + sC_2) \quad (4)$$

$$I_1 = I_{in} - \frac{V_1}{R_S} - (V_1 - V_2)(\frac{1}{sL_2} + sC_2) \quad (5)$$

$$V_2 = I_4(sL_3 - \frac{1}{sC_3}) \quad (6)$$

$$I_2 + I_3 - \frac{V_2}{R_L} = I_4 \quad (7)$$

$$I_{out} = \frac{V_2}{R_L} \quad (8)$$

From (1)-(8), the Signal Flow Graph (SFG) can be initially created in the term of current and voltage variables as shown in Fig.2.

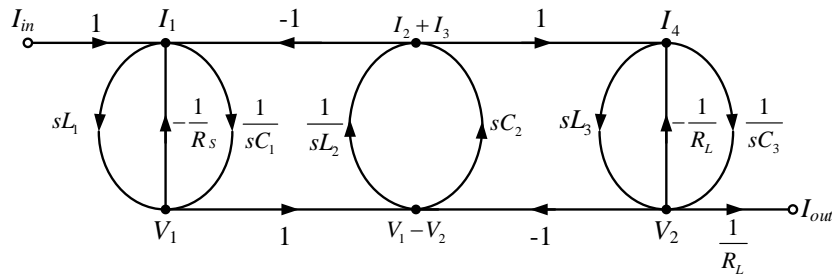


Fig.2: SFG of RLC Chebyshev ladder notch filter

The voltage nodes become to the current nodes by applying the transconductance (g_m) in the several branches. The doubly terminated resistors are given to be $R_S=R_L=1/g_m$. Note that feedback nodes at input and output are observed that the two lossless integrators and two lossless differentiators are replaced by lossy integrators and lossy differentiators, respectively. The final current-mode SFG can be rewritten as Fig.3.

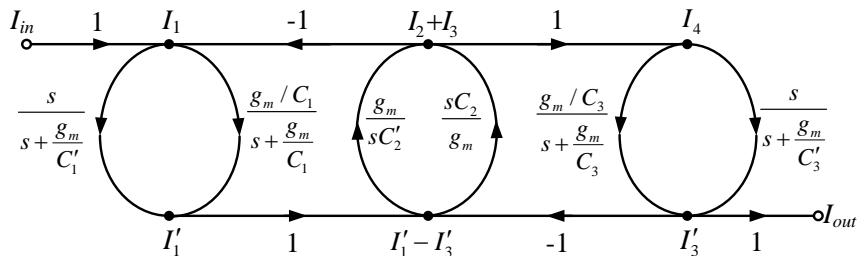


Fig.3: Current-mode SFG of RLC Chebyshev ladder notch filter

From current-mode version of SFG in Fig.3, it is obviously that, it can be realized by directly replaced SFG paths with integrators and differentiators. The proposed Chebyshev ladder notch filter consists of two lossy integrators, two lossy differentiators, a lossless integrator and a lossless differentiator. Note that the multiple positive and negative outputs of OTA are required.

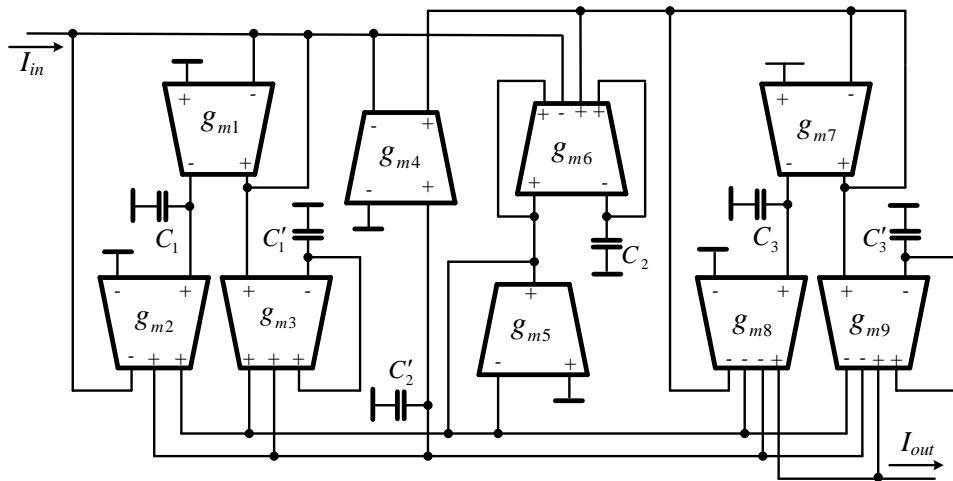


Fig.4: Chebyshev ladder notch filter based on MO-OTAs

The proposed Chebyshev ladder notch filter contains 9 MO-OTAs and 6 grounded capacitors which operate as 2 lossy, 1 lossless integrators and 2 lossy, 1 lossless differentiators.

DESIGN QPSK COMMUNICATION SYSTEM BY SOFTWARE-DEFINED RADIO (SDR)

Siraphop Tooprakai, Korpakit Kobthanyakit, and Tin Suwanmad

School of Engineering, King Mongkut's Institute of Technology Ladkrabang, Bangkok 10520, Thailand

E-mail: siraphop@telecom.kmitl.ac.th

Abstracts

This paper presents the design of a QPSK communication system with Software-Defined Radio (SDR). SDR communication system is a system that uses software to control the digital signal processing (DSP) within a communication system, such as a mixer, filter, modulator and demodulator circuits, etc. This SDR communication system is flexible. and easy to update. Choose a hardware platform and software, which is USRP B210 and MATLAB, respectively. Design and test the QPSK communication system for both receiving and transmitting.

Introduction

Nowadays, digital technology has evolved a lot including the development of radio communication [1]. In the 1980s, components of communication systems began to be developed with digital technology, including Audio Signal Processing, Modulator Circuits, Demodulator Circuits, filter circuit and mixer. It is currently being developed and controlled the processes within the digital communication system with software. This system is called Software Defined Radio (SDR) or Software Radio.

SDR to build a QPSK communication system using a hardware platform. and software, USRP B210 and MATLAB, respectively, using MATLAB software to design a digital signal processing process shows in Fig. 1(a).

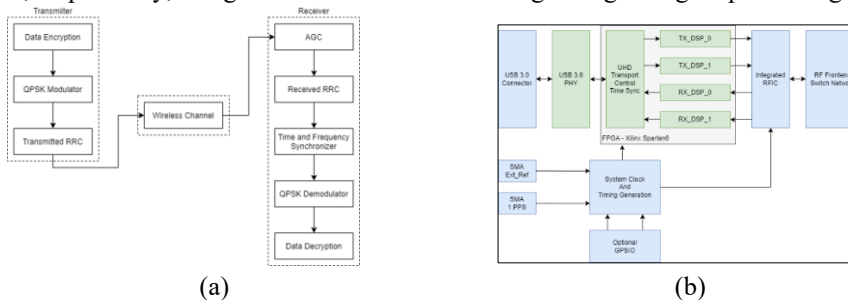


Fig. 1: a) Block diagram of the QPSK communication system. b) USRP B210 internal structure block diagram

Theory

It is a radio communication system which uses software for designing and configuring components such as integrated circuits, filter circuits, modulator circuits. and the modulator circuit, etc.

Ettus Research [2-3] is a leading SDR platform designing a hardware SDR product, USRP. This USRP acts as an RF front-end of a communications system. It consists of an FPGA processor for DSP functions and a microwave circuit, including a digital-to-analog converter circuit or a circuit converting an analog signal to a digital signal. The USRP B210 [2] is an RF-frontend consisting of two main components: a processor for Digital Signal Processing (DSP) computing using Xilinx Spartan6 FPGAs, and a microwave circuit, ADC and DAC range. The operating frequency is 70 MHz – 6 GHz shows in Fig. 1(b).

Design and experiment

The parameters used for the design of the QPSK communication system, shows in Table 1. This procedure uses the QPSK communication model designed in the simulation measurement section where communication from the send side to the receiver side. The signal is transmitted from the USRP B210 on the transmit side via the antenna to the USRP B210 on the receiver side as shown in Figure 2.

Table 1 The parameters used for the design of the QPSK communication system

General properties of communication system	
frequency	140 MHz (with coaxial cable), 4 GHz (with antenna)
data rate	2 Mbps
Technical properties of communication system	
modulation technique	QPSK (with Gray's order)
Scrambler	With polynomial = $x^7 + x^4 + 1$, Initial state = [0 0 0 0 0 0]
Filter	RRC filter, Roll off factor = 0.35, 41 tabs

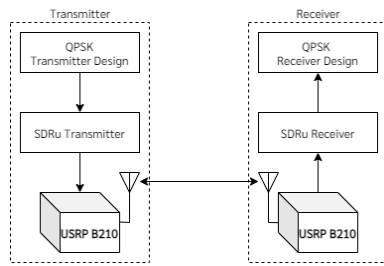


Fig. 2: Block diagram USRP B210.



Fig. 3: Equipment for testing the QPSK communication system over the antenna.

The QPSK communication system designed based on MATLAB and Simulink software is connected to the USRP B210 via blocks named “SDRu Transmitter” and “SDRu Receiver”. Fig3 shows the devices used to test the QPSK communication system at frequencies. 4GHz

Result

Fig. 4 shows the spectrum of the signal at the receiver. The yellow line spectrum is the spectrum received by the communication system, while the blue line spectrum is generated by the signal passing through the RRC filter at the receiver. which has a bandwidth of 77 kHz.

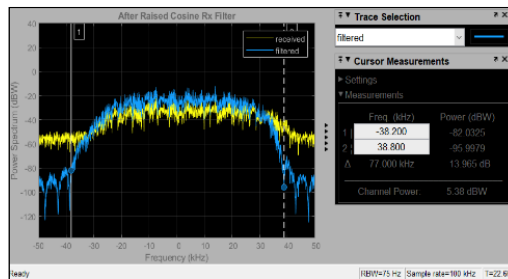


Fig. 4: Comparison of spectrum at the rear communication system through the Rx RRC Filter.

Add a noise channel into the designed communication system. and adjust the E_b/N_0 value of the AWGN Channel block to test the change in C/N value of the signal measured by the spectrum meter. The SDR gain is set to 60 dB, transmitted at a frequency equal to 4 GHz over the antenna as shown in Fig. 5.

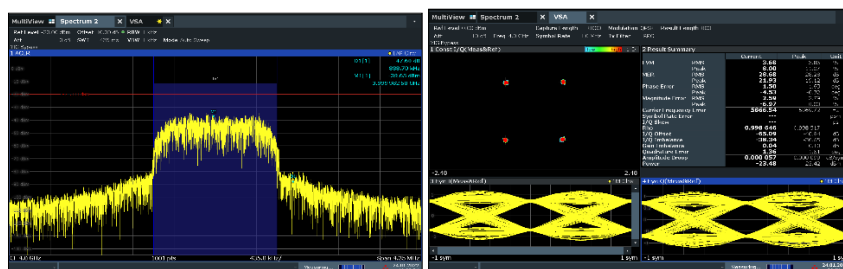


Fig. 5: The spectrum of the QPSK signal at E_b/N_0 is 100 dB.

Conclusion

Testing of the QPSK communication system with SDR revealed that the communication system can actually be built on the SDR communication platform. Reliability meets standards In addition, building a communication system with SDR is also a flexible system. and easy to study and develop

Reference

- [1] J. Muslimin, A. L. Asnawi, A. F. Ismail and A. Z. Jusoh, “SDR-based Transceiver of Digital Communication System using USRP and GNU.” Electrical and Computer Department, Kulliyah of Engineering, International Islamic University Malaysia (IIUM), 2016.
- [2] Ettus Research™, “USRP X Series.” <https://www.ettus.com/products>.
- [3] Ettus Research, “USRP B200 and B210 hardware,” https://www.ettus.com/wp-content/uploads/2019/01/b200-b210_spec_sheet.pdf.

Recognition of Face Expression for Masked Face Images

Susanta Malakar¹ and Kosin Chamnongthai²

King Mongkut's University of Technology Thonburi, Bangkok 10140 Thailand

susanta.Malakar@mail.kmutt.ac.th and kosin.cha@kmutt.ac.th

Abstract: Facial expression is very important to understand the mind state of a person. Facial expression recognition is important for normal people as well as Mentally disable people. Facial expression can help to understand personal emotions and indicate a person's intention[1][2]. There are plenty of research works on Facial expression recognition but in recent years it has been going through many challenges during pandemic because of the face mask. A face mask can cover up to 50-70% bottom area of a face and the bottom area which include the mouth and cheek has most of the features of a face expression. Some researchers have partially solved this problem by reconstruction method, where they can reconstruct the occluded part of the face but they cannot restore the natural expression.

Introduction: In this work we proposed a method which can restore the lower part expression by analyzing the upper part of a face. In our method we assume a face without any expression is in zero expression state. We can easily understand that the changes occur in the upper part and the lower part whenever the face expression changes from zero expression state to any other expression such smile or cry. In fig.1 the first image on left has no expression but the other images have expression and the changes can be noticed on upper part as well as lower part.

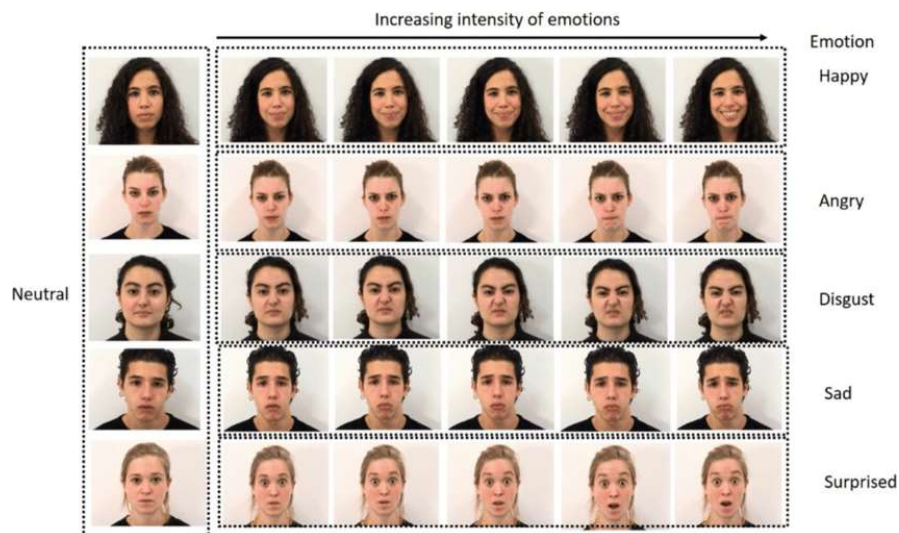


Fig.1: left images are neutral and slowly towards the right side the intensity of expression are increased and upper and lower part of the face is changes symuntaneously (image from ADFES dataset).

Proposed Method: In our proposed method the system learns that which pixels are changing their intensity simultaneously as shown in Fig.2. In training phase, the system takes the neutral face image and change the pixel intensity and finds the pixels of upper part and lower part which are simultaneously changing or not changing. Now system can find the related features of the upper part and the lower part but the system needs to store it. This data storing has huge calculation. For each iteration of pixel intensity change the system gets two matrixes one for upper part and one for lower part. These pair matrixes are related, it demonstrates the relation between upper and lower part. Now system convert the upper part matrix into an encoding vector to cluster it in a unit hypersphere and remembers that the lower part matrix is related to this encoding vector. Now we have a visible part of a target image, next change the pixel values and each iteration of pixel value change, some encoding vectors can be determined which we plot and find its intersection with the training data. At this point it can be determined that, the visible part of the target image belongs to which person we don't know the exact facial

expression so the restoration process start from this point. From the intersection of the encoding vectors, we can determine the lower part matrixes which is converted into image and marge together to get the restored lower part.

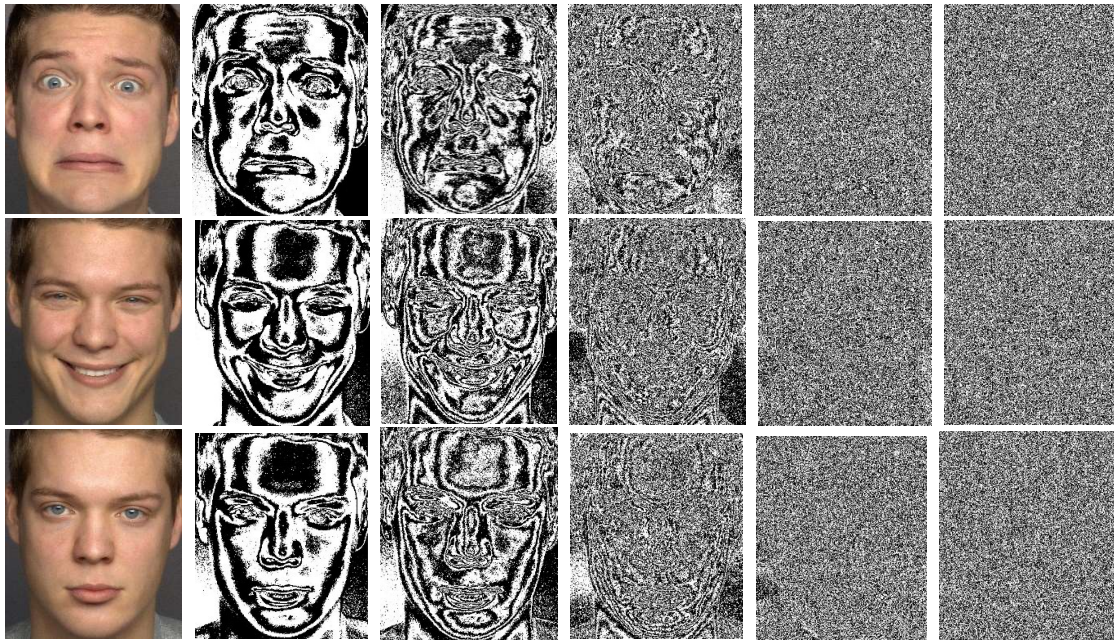


Fig.2: left bottom image is zero expression face and left middle and left top is smile afraid expression. Other images are processed by changing the pixel intensity layer by layer.

Data Analysis and Result: We choose front view mug shot images because it has no head rotation and also has a stable lighting condition. Another reason of choosing mugshot image is if it is not mug shot image then the image will definitely have some head rotation which will cover some part of the and eventually covering the features of facial expression. Our proposed method has 7% higher accuracy comparing to conventional method.

Conclusion: During face expression change if the face is occluded by a face mask, the face expression of the subject can not be identified. Influenced by ‘ADFES dataset’ a method has been developed which relies on the main concept of slowly face expression change. Bit plane extraction has been used and improved face recognition accuracy.

FACES dataset: 171 young (n = 58), middle-aged (n = 56), and older (n = 57)
six facial expressions: neutrality, sadness, disgust, fear, anger, and happiness

- Reference:** 1. <https://www.frontiersin.org/articles/10.3389/fpsyg.2017.02175/full#:~:text=Introduction-Facial%20expressions%20can%20display%20personal%20emotions%20and%20indicate%20an%20individual's,extremely%20important%20for%20social%20interaction.>
2. Putting facial expressions back in context
3. arxiv.org/abs/1503.00088 : Facial Expression Cloning with Elastic and Muscle Models

Jerk-based High Complex Chaotic Generator with Modified Rectangular and Signum Functions

Khunanon Karawanich, and Pipat Prommee

Department of Telecommunications Engineering,

School of Engineering, King Mongkut's Institute of Technology Ladkrabang, Bangkok 10520, Thailand

Email: 64601023@kmitl.ac.th, pipat.pr@kmitl.ac.th

Abstract This work presents a new, highly complex chaotic generator from the conventional jerk model with two different nonlinear functions. The first function is the modified signum function, and the second is the new modified rectangular function. The system can be generated the strange four-scroll attractor by adjusting only one coefficient (k). The Lyapunov exponent and the bifurcation investigate the fundamental dynamics theories of the system. The Kaplan-Yorke dimension (D_{KY}) is 2.45 also proves the high complexity of the system. In this work, the numerical simulations have confirmed the workability by MATLAB.

1. Introduction

In two decade years, new high complexity chaotic attractor has been rapidly developed with multi-scroll or multi-wing chaotic attractors in 3-D autonomous systems [1]. Generally, the increase of scroll number, the dynamic behaviors of the chaotic attractor become more complex. The multi-scroll chaotic system is considerable attention from many researchers [2]. The multi-scroll chaotic behavior is an important issue, that the complexity of system should be carefully investigated. Hence, the performance of the autonomous chaotic system can be confirmed by the numerical analyses as well as the Lyapunov exponent [3]. If the system is highly complex, the Lyapunov exponent of the system would be a higher positive value than the general chaotic system, and the Kaplan-Yorke value is also high. In a third-order chaotic system, the well-known autonomous chaotic system is "jerk model". The general form of jerk model is $\ddot{x} = F(\ddot{x}, \dot{x}, x)$, where x is the position, the first derivative (\dot{x}) denotes for speed, second derivative (\ddot{x}) denotes the acceleration, the third derivative ($\ddot{\ddot{x}}$) represents the jerk [4]. Jerk model is a low complexity structure and able to modify based on one coefficient (k) and without disturbing the nonlinear function ($G(x)$). There are multi-scroll chaotic generators based on jerk model which operated by increasing the breakpoints of nonlinear function to achieve multi-scroll attractors. The nonlinear functions (modified signum and sine) are required by using the multiple breakpoints. These systems utilized the function with multiple breakpoints that suffer from many coefficients are required. Besides, the many coefficients also have drawbacks due to the complicated structure and difficulty of control.

2. Design of the proposed chaotic system and numerical results by MATLAB

In this article, a new 3-D chaotic jerk model is proposed with modified two nonlinear functions and five coefficients. The single-scroll, double-scroll, and four-scroll attractor metamorphosis can be manipulated by using only one coefficient (k). The chaotic behaviors are verified by the route to chaos, the bifurcation. The complexity of attractor is proven by Kaplan-Yorke Dimension (D_{KY}), The MATLAB results show that the high dynamic, complexity attractors, low-complex structure, and conveniently controllable.

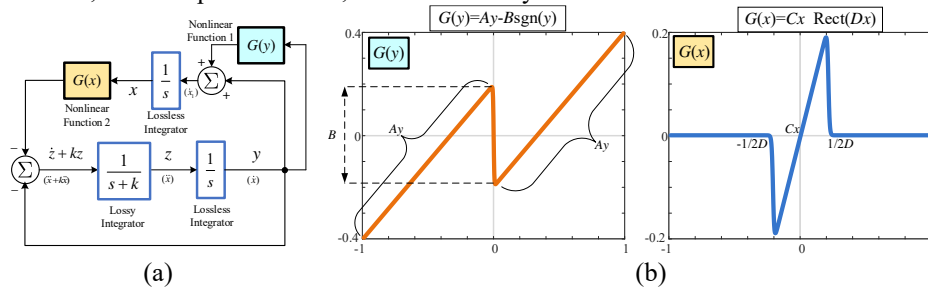


Fig. 1. Design of the proposed chaotic system (a) block diagram (b) modified signum and modified rectangular function

A proposed new four scroll 3-D chaotic system is illustrated by the block diagram as shown in Fig. 1(a). The highlight of this work uses two unique nonlinear function (NLF) to generate complex attractors. The first function using traditional signum function ($G(y)$) and the second function named the modified rectangular function ($G(x)$) are shown in Fig.2(b), respectively. From Fig.1(a), three differential equations are expressed as

$$\begin{cases} \dot{x} = y + G(y), \\ \dot{y} = z, \\ \dot{z} = -kz - y - G(x). \end{cases} \quad (1)$$

where $G(x) = Cx \cdot \text{Rect}(Dx)$, $G(y) = Ay - B \text{sgn}(y)$, and A, B, C, D, k are the constant coefficients.

The proposed system (1) can be generated single-scroll, double-scroll, and four-scroll chaotic attractors through adjusting a single coefficient k . For example, the value of coefficients applied for single-scroll, double-scroll, and four-scroll are respectively, $k = 0.7, k = 0.6$, and $k = 0.4$ while keeping $A=0.6, B=0.2, C=1, D=2.5$, and the initial conditions $(x_0, y_0, z_0) = (0.1, 0.1, 0.1)$. The proposed system is confirmed chaotic behavior by the Lyapunov exponent (LE). The system with a positive LE is usually chaotic. The calculation of LE can be obtained by Wolf's algorithm in MATLAB [3]. In the proposed system, the coefficients $(A, B, C, D, k)=(0.6, 0.2, 1.5, 2.35, 0.4)$ are given with the initial conditions assumed $(x_0, y_0, z_0)=(0.1, 0.1, 0.1)$. The proposed system provides $LE_1=0.241701, LE_2=-0.04$, and $LE_3=-0.448254$, as shown in Fig. 2.

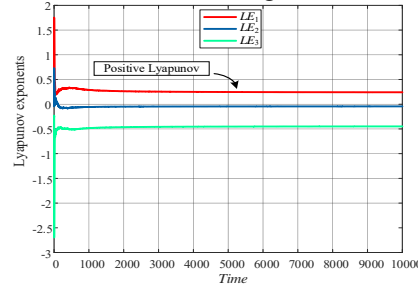


Fig.2 Lyapunov exponent of the proposed system

The complexity of the proposed chaotic system can be verified by using the Kaplan-Yorke dimension (D_{KY}) [3] as

$$D_{KY} = j + \frac{1}{|LE_{j+1}|} \sum_{i=1}^j LE_i = 2 + \frac{LE_1 + LE_2}{|LE_3|} = 2 + \frac{0.241701 - 0.04}{|-0.448254|} = 2.45 \quad (2)$$

where j is the largest integer satisfying $\sum_{i=1}^j LE_i \geq 0$ and $LE_{j+1} < 0$ given $j \leq D_{KY} < j+1$, which D_{KY} indicated to the complexity quantitative of the chaotic systems. In this work, the parameter k was used to represents the various dynamic behaviors. Fig. 3 shows the bifurcation of parameter k in the range 0.1 to 0.8 compared with the results of phase portraits on the z - x plane. The other parameters are $A=0.6, B=0.2, C=1$, and $D=2.5$. Starting from the stable point shown at $k=0.78$, the single-scroll attractor shown at $k=0.7$, the double-scroll attractor shown at $k=0.6$, and the approaching four-scroll attractor shown at $k=0.45$. In highly complex chaotic, the four-scroll attractor can be shown when $k < 0.4$.

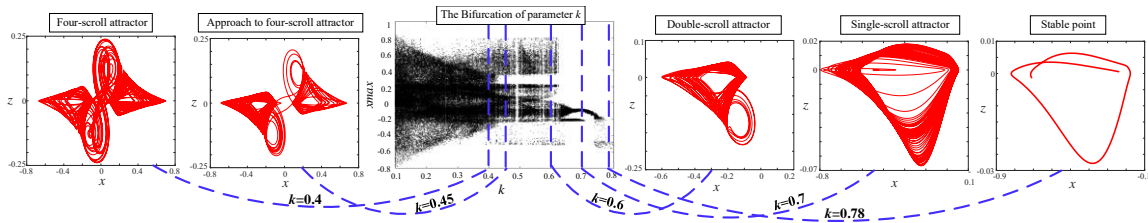


Fig.3 The route to chaos of the proposed system for parameter k

The proposed system's nominal coefficients (NC) [5] are as follows: $A = 0.6, B = 0.2, C=1, D=2.5$, and $k = 0.4$, presented as an interesting attractor on x - y, x - z, y - z and 3D planes in Fig. 4(a)-(c).

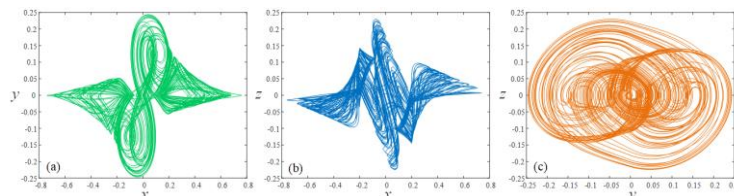


Fig.4 The attractor of the proposed system (a) x - y plane (b) x - z plane (c) y - z plane

Reference

- [1] W. Liu, W. K. S. Tang, and G. Chen, "2 × 2-scroll attractors generated in a three-dimensional smooth autonomous system," International Journal of Bifurcation and Chaos, vol. 17, no. 11, pp. 4153–4157, 2007.
- [2] J. Lu and G. Chen, "Generating multiscroll chaotic attractors: theories, methods and applications," International Journal of Bifurcation and Chaos in Applied Sciences and Engineering, vol. 16, no. 4, pp. 775–858, 2006.
- [3] A. Wolf, J.B. Swift, H.L. Swinney and J.A. Vastano, "Determining Lyapunov exponents from a time series," Phys. D, vol.16, pp.285–317, 1985
- [4] J.C. Sprott, "A new class of chaotic circuit," Physics Letters A, vol.266, pp.19-23, Feb 2000.
- [5] Karawanich K, Prommee P. High-complex chaotic system based on new nonlinear function and OTA-based circuit realization. Chaos Solit Fract 2022;162:112536.

The Computerized Test for Screening Dementia in the Elderly: Pilot Study

Warissara Limpornchitwilai¹, Chatchai Paengkumhag¹, Boonserm Kaewkamnerdpong¹, and Kosin Chamnongthai²

Biological Engineering Program, KMUTT¹, Department of Electronic and Telecommunication Engineering, KMUTT²
lwarissara.p@gmail.com, c.paengkumhag@gmail.com, boonserm.kae@mail.kmutt.ac.th, and kosin.cha@kmutt.ac.th

The problem of the increase in the elderly or the aging society is currently occurring in many countries. In Thailand, the population aged 60 and over will increase to 33% in 2040 [1]. It is one of the problems that require innovation in various parts of medicine, treatment, therapy, and innovation to support their lives. Our focus in this study will be on dementia, the main cause of disability in the elderly [2], a condition most prevalent in the elderly and causes significant damage to themselves and others. There are many tests to assess the risk of dementia using interviews and tests. However, the commonly used assessment test is paper-based, requiring medical staff to evaluate the results [3]. In this pilot research, we proposed using a computerized test to screen for dementia in the elderly by analyzing collected data when the elderly interact with the test on a computer or tablet. The test was developed from the commonly used paper-based test such as Montreal Cognitive Assessment (MoCA), Mini-Mental State Examination (MMSE) [4], and online testing such as the Wisconsin Card Sorting test (WCST) [5]. The test has five tasks in the Thai language that the elderly must complete and use the time around 30 minutes. The developed test has various domains to test their cognitive ability, such as attention, orientation, visuospatial, language, and memory—the detail of each task is shown in Fig 1.



Fig.1: The cognitive domain detail that each task can measure.

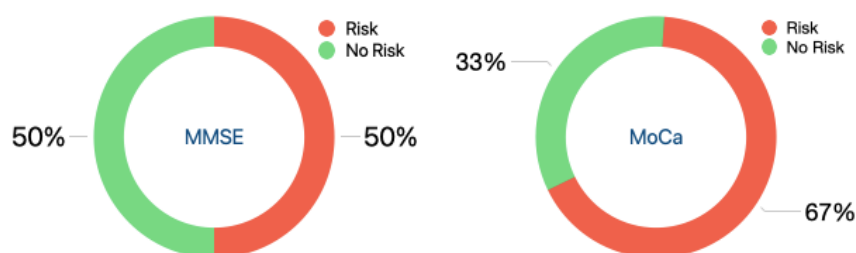


Fig.2: The percentage of risk to be dementia of all participants from MMSE and MoCA results.

In this study, we have 12 participants, six females and six males; all participants are healthy elderly and have never been diagnosed with dementia. For more information on participants, the average age of participants is 63 years, no smoking behavior, and various education level from high school to doctoral degree. Participants take MMSE and MoCA first as a paper-based test in the experiment. After that, they start to take the test on a computer. Both paper-based tests show that six participants have a risk of dementia from MMSE, and eight have a risk of dementia from MoCA as shown in Fig 2. The results of our system, when compared to both paper-based tests, from the average score of our test and MMSE, were not a statistically significant difference with the

statistical values, respectively, are $t = -2.069$, $p = 0.054$. The average score of our test and MoCA was not a significant difference with the statistical values, respectively, $t = 0.868$ and $p = 0.395$. Therefore, when compared with the MMSE and the MoCA, our assessment test did not differ in the assessment results. For more detail about the statistic test of each domain, when compared our test with MoCA, language and memory recall tasks did not have a significant difference with the statistical values, respectively, are $t = -0.23$ and $p = 0.82$, and $t = -0.13$ and $p = 0$. When we compared our test with MMSE, only memory recall task did not have a significant difference; the statistical values, respectively, are $t = -0.69$ and $p = 0.5$. The other test on both MoCA and MMSE is a significant difference.

The correlation between our test and MMSE using Pearson's correlation is 0.65, and MoCA is 0.44, which means both tests have a positive correlation with our test. Analyzing the correlation between time used and the correctness of the responses was no correlation, with a value of 0.016. So, the time taken during the task does not affect the correctness of the response. Analyzing the correlation between the participant's age and the test score found that it is no correlation, with a value of -0.054, meaning the age does not affect the test score. Also factor about education level got a correlation value of -0.25, which means education level does not affect the test score. The detail of correlation results as shown in Fig 3:

	Age	Test1	MeanRT_1	Test2	MeanRT_2	Test3	MeanRT_3	Test4	MeanRT_4	Test5	MeanRT_5	IMC	MMSE	MOCA
Age	1	0	0.41398123	-0.04222	0.30365984	0	0.0531625	0.30099611	0.50792413	-0.2920313	0.69611217	-0.0538411	-0.4713266	-0.1723626
Test1	0	1	0	0	0	0	0	0	0	0	0	0	0	0
MeanRT_1	0.41398123	0	1	0.08809144	0.87089867	0	0.67591988	0.08013498	0.35514363	0.47920943	0.74314076	0.67165969	0.25772018	0.36507273
Test2	-0.04222	0	0.08809144	1	0.07397667	0	-0.3153458	-0.1186683	0.14926379	0.23166619	-0.187089	0.23586135	0.38749609	0.22268089
MeanRT_2	0.30365984	0	0.87089867	0.07397667	1	0	0.8028652	0.05528752	0.40617853	0.46776755	0.76467396	0.65827734	0.11073183	0.08089623
Test3	0	0	0	0	0	1	0	0	0	0	0	0	0	0
MeanRT_3	0.0531625	0	0.67591988	-0.3153458	0.8028652	0	1	-0.2236208	0.24662558	0.45835771	0.62206292	0.47942597	0.1193346	-0.0461485
Test4	0.30099611	0	0.08013498	-0.1186683	0.05528752	0	-0.2236208	1	-0.2244529	-0.3555759	0.07253084	0.27055069	-0.25013	-0.1117987
MeanRT_4	0.50792413	0	0.35514363	0.14926379	0.40617853	0	0.24662558	-0.2244529	1	0.05345255	0.4299873	-0.0112403	-0.2006492	0.18553887
Test5	-0.2920313	0	0.47920943	0.23166619	0.46776755	0	0.45835771	-0.3555759	0.05345255	1	0.17045435	0.71747867	0.74563846	0.50666424
MeanRT_5	0.69611217	0	0.74314076	-0.187089	0.76467396	0	0.62206292	0.07253084	0.4299873	0.17045435	1	0.25559947	-0.2706954	-0.1844394
IMC	-0.0538411	0	0.67165969	0.23586135	0.65827734	0	0.47942597	0.27055069	-0.0112403	0.71747867	0.25559947	1	0.64994709	0.44187315
MMSE	-0.4713266	0	0.25772018	0.38749609	0.11073183	0	0.1193346	-0.25013	-0.2006492	0.74563846	-0.2706954	0.64994709	1	0.65537769
MOCA	-0.1723626	0	0.36507273	0.22268089	0.08089623	0	-0.0461485	-0.1117987	0.18553887	0.50666424	-0.1844394	0.44187315	0.65537769	1

Fig.3: The correlation value of task score, average time used, and participant age.

From the results of this pilot study, the test developed as a computerized test worked well. The t-test and the correlation value show that we can use the developed test to be an assessment the same as the paper-based test we used for screening dementia in the elderly. Furthermore, this study must be tested with more participant numbers to clarify whether the test can replace the paper-based test. Also, must study more detail about each cognitive domain that the test can measure to analyze whether this test can monitor cognitive change in the elderly. Also, each domain has only some that were not significantly different. The test must be adjusted, and the other cognitive task might be added to this assessment tool to develop this test to measure more cognitive domains in one test.

Moreover, we plan to add Artificial Intelligence or AI to our test. It might be screening faster to become an early detection assessment tool that uses less time to take the test. In addition, it might protect familiarity of testing early who can remember the task that may lead to the incorrect test result.

Reference

[1] Economic Research Institute for ASEAN and East Asia (ERIA), “Lessons from One of the Most Aged ASEAN Member States,” *Population Ageing in Thailand*, ERIA, Thailand, June 2021.

[2] I. Lisko, J. Kulmala, M. Annetorp, T. Ngandu, F. Mangialasche, M. Kivipelto, “How can dementia and disability be prevented in older adults: where are we today and where are we going?,” *Journal of Internal Medicine*, vol. 289., no. 6, pp.807-830, 2021, doi.org/10.1111/joim.13227.

[3] Kang Min Yu et al., “Effect of Paper-Based Cognitive Training in Early Stage of Alzheimer's Dementia,” *Dementia and Neurocognitive Disorders*, vol. 18, no. 2, pp. 62-68, Jul. 2019, doi: 10.12779/dnd.2019.18.2.62.

[4] X. Jia et al., “A comparison of the Mini-Mental State Examination (MMSE) with the Montreal Cognitive Assessment (MoCA) for mild cognitive impairment screening in Chinese middle-aged and older population: a cross-sectional study,” *BMC Psychiatry*, vol. 21, no. 1, pp. 485, doi.org/10.1186/s12888-021-03495-6.

[5] F. Barceló, M. Sanz, V. Molina, FJ. Rubia, “The Wisconsin Card Sorting Test and the assessment of frontal function: a validation study with event-related potentials,” *Neuropsychologia*, vol. 35, no. 4, pp. 399-408, Apr. 1997, doi: 10.1016/s0028-3932(96)00096-6.

Effects of the tablet-based gaming app to promote personal help and social skills in student with autism

Chatchai Paengkumhag, M.Ed.¹, Warissara Limpornchitwilai, M.Eng.¹, Kosin Chamnongthai, Ph.D.², and Boonserm Keawkammerdpong, Ph.D.^{1*}

Biological Engineering Program, KMUTT 1, Department of Electronic and Telecommunication Engineering, KMUTT 2

Email address: chatchai.p@mail.kmutt.ac.th | boonserm.kae@kmutt.ac.th ^{1*}

1. Introduction

Autistic children have significant impairments in social interaction, communication and repetitive behaviours that have a direct impact on their ability to engage in activities of daily living and participate in their environment [1]. Today, the number of children with autism is growing steadily around the world, including in Thailand [2]. According to the report of the Department of Mental Health of Thailand has estimated 370,000 individuals with autism. Nowadays, autism does not have a cure. Therapy is needed to help children with autism. The problem is that there are not enough experts to support the growth of increasing number of autistic children. They frequently recommend that parents promote the learning of their child at home. It will facilitate continued development, but it's not easy for inexperienced parents. Consequently, technology (games, computer programs and tablet applications) is now playing an important role in supporting children with autism in many fields such as education, therapy and specific-skills training. Most of the existing technology games have been designed for specific skills. There are not many games that have designed the contents and mechanics of the game through various integrated skills. Moreover, there are a few games to teach personal help skills in daily routines and prepare them to deal with expected situations in their social setting [3]. There is a shortage of creative media suitable for promoting learning for children with autism as mentioned above. Therefore, we developed an educational game that combined the contents, situations, and places that children with autism may encounter in their daily routine. It was about maximizing the effectiveness of promoting language and communication skills, cognitive and practical personal help, and interaction with others in society. We designed and developed the game based on participatory design theory utilizing experts and the perspective of a user. It also corresponds more closely to the lifestyle of autistic children. The purpose of this research is to explore the impact of using tablet-based gaming app to promote personal help and social skills for children with autism in school settings.

2. Methods

This research is Quasi-Experimental Research (The One-Group Pretest-Posttest Design). The research project was approved by the Committee on Ethics of Human Research (KMUTT). It was part of the research project "Game to promote personal help and social skills for autistic children". The certification number was KMUTT-IRB-COA-2021-015 (February 9, 2021).

2.1 Game

We developed the tablet-based gaming app entitled Imboon-Ounjai Travelling Around the World. The development protocol was applied using Participatory Design Theory, conceived from both expert and user viewpoints. The design application was based on the research guidelines of Malinverni L and et al [4] and Strum D and et al [5]. The experts involved therapists and educational designers, testing the efficacy with three voluntary autistic children through demonstration, interview and observation. This design included the content and learning activities, the game mechanism and the reward system. The tablet-based gaming application was adapted to individual autism using Fuzzy Logic.



Fig 1: Learning scenarios in this game

2.2 Assessment forms

Autism Treatment Evaluation Checklists (ATEC) covers four aspects: language/communication, sociability, sensory/ cognitive awareness, and health/ physical/ behavior. The scores may have shown that autistic severity is mild, moderate, severe [6] [7] [8].

The Personal Help and Social Skills Assessment Form is an assessment form created by the researcher for using in this study. It covers the routines of children with autism, composed of six assessment contexts: self-help in the context of the house, school, public transport, cafeteria, playground and store.

2.3 Experiment design

The experimental plan was divided into three sessions. The first session was a before the experiment. Teachers and parents were required to sign the consent form and complete the pre-test evaluation. The second session was the experiment, Teacher were received a 10.4-inch Samsung Galaxy Lite Tab S6 tablet with an internet SIM card. After that, the teachers downloaded the game into the Android OS from the Google Play Store and installed it onto the tablet. Teacher registered every child with autism who took part in the research project. The teachers then supervised autistic children to play games every day at school over a four-week period. It took twenty minutes a time. The third session was after the experiment. Teachers and parents had to complete the assessment as a result of the exam.

3 Results

There were 16 individual autism participants, aged between 6-13 years old, M= 10 years old, S.D.= 2.1. After experimental four weeks, participants showed higher average scores across contexts. Participants were found to have improved their personal help and social skills from the point of view of teachers and parents. A comparison using the Wilcoxon Signed-Rank Test found that competencies in the cafeteria context and in the overall context are significantly different at .05. Although the average score was greater than before-experiment, there was no significant difference.

4. Conclusion and future work

The tablet-based gaming apps can be used as a tool to help autistic children learn and improve their personal help and social skills. For the future, we will add AI to make the game more appropriate and can be adaptive for individual with autism. It's based on data which has collected form this experiment.

Reference

- [1] A. P. Association, "Diagnostic and statistical Manual of Mental Disorder 5th," Library of Congress, Virginia, 2013.
- [2] J. Borg, R. Berman-Bieler, C. Khasnabis, G. Mitra, W. N. Myhill and D. Samant Raja, "Assistive Technology for Children with Disabilities: A Discussion Paper," World Health Organization, 2015.
- [3] K. Spiel, C. Frauenberger, O. Keyes and G. Fitzpatrick, "Agency of Autistic Children in Technology Research - A Critical Literature Review," *ACM Transactions on Computer-Human Interaction*, vol. 26, no. 6, 2019.
- [4] L. Malinverni, J. Mora-Guiard, V. Padillo, L. Valero, A. Hervas and N. Pares, "An Inclusive Design Approach for Developing Video Games for Children with Autism Spectrum Disorder," *Computer in Human Behavior*, vol. 71, pp. 535-549, 2016.
- [5] D. Strum, M. Kholodovsky, R. Arab, D. S. Smith, P. Asanov and K. Gillespie-Lynch, "Participatory Design of a Hybrid Kinect Game to Promote Collaboration Between Autistic Players and Their Peers," *International Journal of Human-Computer Interaction*, vol. 35, no. 8, pp. 706-723, 2019.
- [6] K. Sunakarach and P. Kessomboon, "Validity and Reliability of the Thai Version of the Autism Treatment Evaluation Checklist: A Two-phase Diagnostoc Accuracy Study [Version 1; Referees: Awaiting Peer Review]," *F1000RESEARCH*, vol. 7, no. 538, 2018.
- [7] I. Magiati, J. Moss, R. Yates, T. Charman and P. Howlin, "Is the Autism Treatment Evaluation Checklist a Useful Tool for Monitoring Progress in Children with Autism Spectrum Disorders?," *Journal of Intellectual Disability Research*, vol. 55, no. 3, pp. 302-312, 2011.
- [8] D. A. Geier, J. K. Kern and M. R. Geier, "A Comparison of the Autism Treatnet Evaluation Scale Checklist (ATEC) and the Childhood Autism Rating Scale (CARS) for the Quantitative Evaluation of Autism," *Journal of Mental Health Research in Intellectual Disabilities*, vol. 6, no. 4, pp. 255-267, 2013

Application for Analyzing Data Transmission Path on Communication Network Using Optical Character Recognition

Pattara Kladkaew, Werapon Chiracharit

Department of Electronic and Telecommunication Engineering

Faculty of Engineering

King Mongkut's University of Technology Thonburi

pattara.k@kmutt.ac.th, werapon.chi@kmutt.ac.th

At present, the organization's application system transfers data from the head office to the branches all over the country with internet protocol and often encounters with a problem in data transmission. This can be solved by doing a tracert or traceroute. However, because there are many organization's internet protocol addresses and each router has more than one IP address assigned to it, network administrators need to spend time finding router device information from all IP addresses. This paper therefore presents a tracert or traceroute monitoring system to analyze traffic paths for internet protocol addresses on corporated communications networks. Using OCR to display automatically the result of name of the router device on the traffic path. This allows network administrators to know the names of all router devices on the traffic path about 30 times faster than conventional authentication methods and with validation accuracy of 95%.

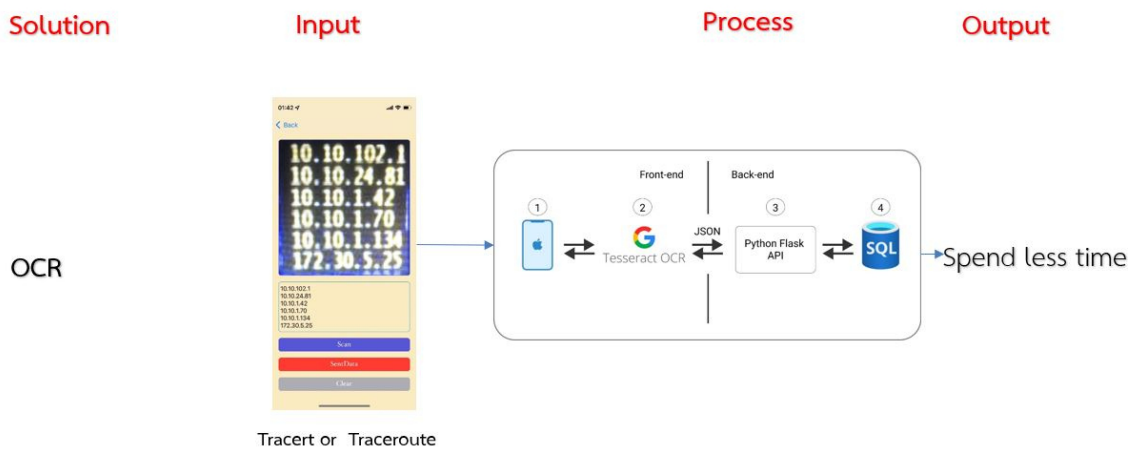


Fig. 1: Working connection

Using SwiftYesseractRTE, the traffic path is analyzed for internet protocol addresses on corporated communications networks. This is a program to detect the IP address from the tracert or traceroute and output it to the router device in the automatic traffic path using Swift 4, which is the Apple preprogramming language. To build the iOS application and manage the database with Microsoft SQL sever to store router device name and IP address data, Python Flask framework is used to act as a server and to transmit data from the application via JSON API with workflow as shown in Fig. 1.

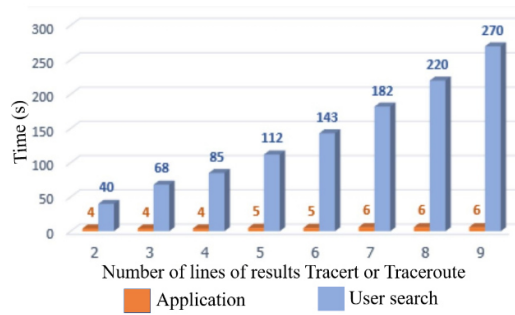


Fig. 2: Duration test bar chart

From the test results in Fig. 2, it shows that the time it took to find the name of the router device from the Tracert or Traceroute results was faster than that of the user searching for it manually. As the number of lines of IP address numbers increases, applications use the same browsing time or only slightly higher. This is different from having the user manually search for the name of the router device from a tracert or traceroute result, when the number of lines of the IP address is increased, the search time is significantly increased.

This research has developed a Tracert or Traceroute monitoring application that allows network administrators to review and get a summary of the name information of all router devices on the line. The data transmission was 30.4 times faster than the average manual data validation method and had validation accuracy of 95%.

A Development of LVDT Demodulator Circuit Based on FPAA chip

Krit Angkeaw ¹, Preechar Thongdit ², and Surachai Chanchay ¹

Department of Instrumentation and Electronics Engineering, King Mongkut's University of Technology North Bangkok.

Bangkok, Thailand.1,

Department of Electrical and Computer Engineering, King Mongkut's University of Technology North Bangkok.

Bangkok, Thailand.2,

surachai.c@eng.kmutnb.ac.th, preecha.t@eng.kmutnb.ac.th, and krit.a@eng.kmutnb.ac.th

Abstracts This paper presents demodulator circuit for LVDT based on the field programmable analog array is implemented. The proposed circuit uses the ratio matrix method and employs a single CMOS Field Programmable Analog Array (FPAA) device. It consists of a summing amplifier, divider circuit, and lowpass filter. The demodulator circuit's functional elements are realized by employing the available Configurable Analogue Modules (CAMs) of the FPAA AN231E04 from AnadigmDesigner®2. Thus, direct current (DC) voltage between -2.43 and +2.3 at 2.5 kHz is proportional to displacement -3 mm until +2.8 mm is outputted. Results show that displacement sensor nonlinear error is $\gamma = 0.27\%$.

INTRODUCTION

LVDT is a transducer that has accuracy in a position measurement. The wire connection of LVDT can be determined for 2 types a 4-wire connection which is also called "open wire" and a 5-wire connection called "ratio matrix wire" [1-5]. These both connections need sinusoidal voltage excitation with the kilohertz frequency range for the iron core and up to a hundred kilohertz for the ferrite core to excite at the primary coil. The magnetic field, which was produced from this excitation, induces both secondary coils to generate the two secondary voltages which have the same frequency as excitation voltage but the difference in amplitudes due to the core distance dependence. The sinusoidal output voltage of LVDT has to be modified to dc voltage before using as a sensor. This signal modification process normally uses a demodulator circuit.

Two kinds of demodulator circuits for LVDT have been introduced such as synchronous demodulators [6] and rational demodulators [7]. Even though the synchronous demodulator circuit is convenient to use because there is a readymade IC which widely provision in the market. But it needs the sinusoidal voltage that is completely compatible with the excitation voltage for infallible operation. Besides, there is a demodulator circuit based on DSP [8] that can compensate for the problem of phase shift between excitation voltage and secondary voltage of LVDT without external tuning but its circuit is complex and needs so many low pass filter circuits to eliminate high order harmonics because of the square wave input voltage. For the rational demodulator technique, there are supplied readymade IC AD598 and AD698 [9] in the market. Both ICs can be excited at the primary coil with excitation voltage in the frequency range of 20 Hz up to 20 kHz and give dc voltage output. However, they need an external RC connection to eliminate the phase lag problem.

This paper presents the development of a rational demodulator technique based on an FPAA chip without an external passive devices connection. This proposed circuit can easily be tunable via AnadigmDesigner®2 software and gives the dc voltage output that relates to the moving core distance.

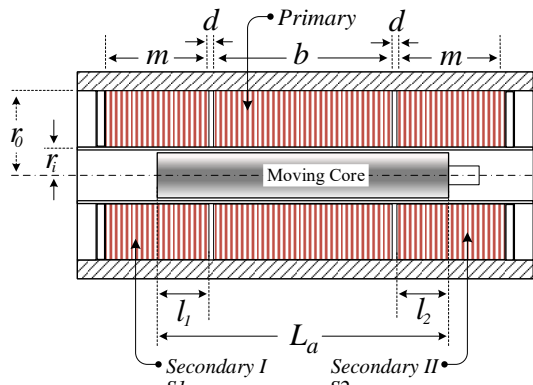


Fig.1: Internal structure of LVDT

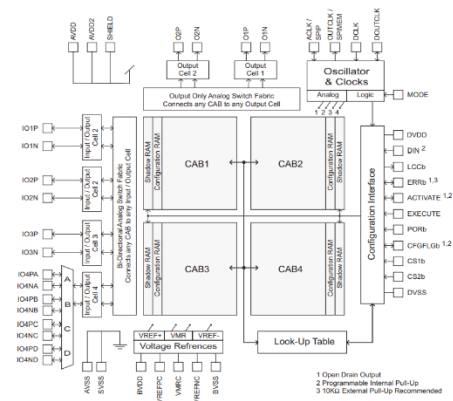


Fig.2: Internal architecture of FPAAs

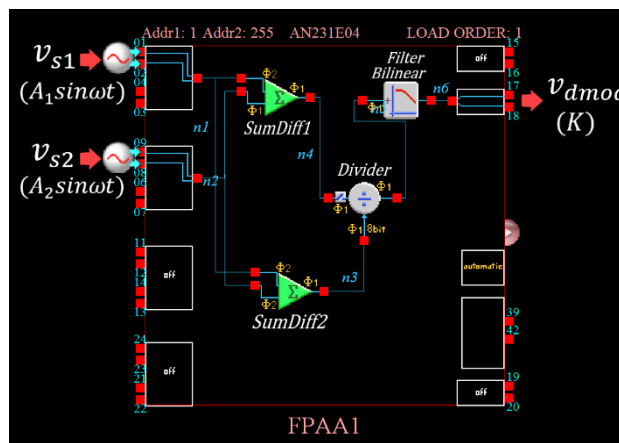


Fig. 3: Internal function of signal conditioning circuit based on FPAAs

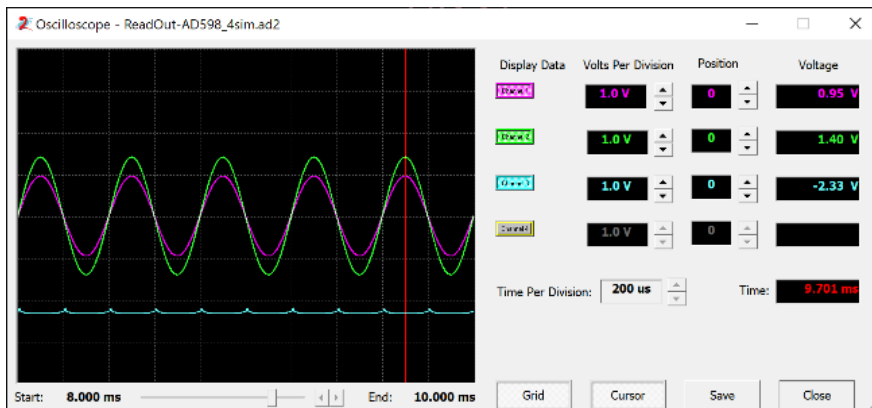


Fig.4: Output waveform at the distance of the LVDT core equals -2.8 mm

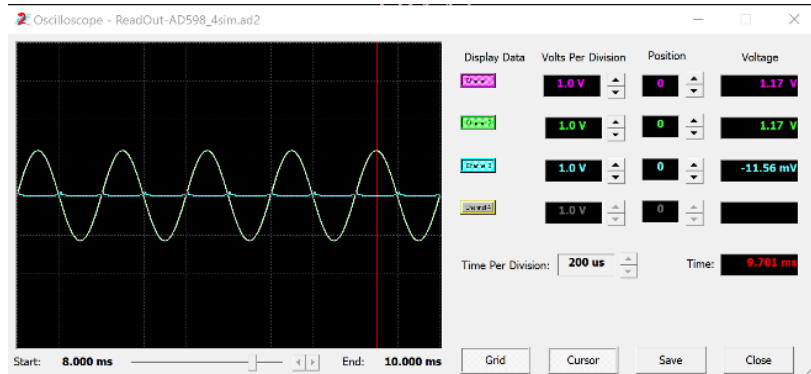


Fig.5: Output waveform at a distance of LVDT core equals 0 mm

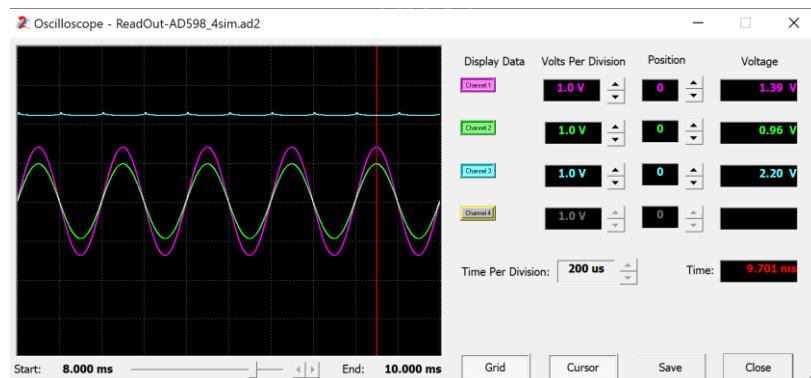


Fig. 6: output waveform at a distance of LVDT core equals +2.8 mm

Conclusion

From the simulation results of the proposed circuit using AnadigmDesigner@2 software, it can be seen that the output voltages at each core distance of LVDT from the proposed circuit are close to the dc voltage that was calculated from the rational voltage principle. It means that these output voltages from the proposed circuit at every core distance in the operation range are in good agreement with ideal linearity. This proposed circuit can be developed for more convenient use to the users such as the addition of an oscillator circuit block in order to generate excitation voltage at the primary coil instead of using an external oscillator circuit which needs the calculation process for any required devices. While in the FPAA based, the calculation for any devices is not needed, the required frequency of the oscillator can be set via AnadigmDesigner@2 software and also can be implemented on the fly to the FPAA chip simultaneously.

REFERENCE

- [1] R. Pall'as-Areny and J. G. Webster, *Sensors and Signal Conditioning*. New York, NY, USA: Wiley, 2001.
- [2] W. Petchmaneelumka, K. Songsuwankit, and V. Riewruja, "Accurate LVDT signal converter," *Int. Rev. Elect. Eng.*, vol. 11, no. 3, pp. 340–347, 2016.
- [3] W. Petchmaneelumka, W. Koodtalang and V. Riewruja, "Simple Technique for Linear-Range Extension of Linear Variable Differential Transformer," in *IEEE Sensors Journal*, vol. 19, no. 13, pp. 5045-5052, 1 July, 2019.
- [4] K. Banerjee, B. Dam, and K. Majumdar, "A novel FPGA-based LVDT signal conditioner," in *Proc. IEEE Int. Symp. Ind. Electron.*, Taipei, Taiwan, pp. 1–6, May 2013.
- [5] K. Angkeaw, S. Chunchay, and P. Thongdit, "A Wide Linearity Range of LVDT Using Approximate Function," 18th International Conference on Electrical Engineering/Electronics, Computer, Telecommunications and Information Technology (ECTI-CON), Chiang Mai, 21, pp. 825-828
- [6] R. Liu, and H. Bu, "Design on LVDT Displacement Sensor Based on AD598. *Sensors & Transducers.*, vol. 160, no.12, pp. 68–73, Dec. 2013.
- [7] R. Casanella, O. Casas, M. Ferrari, V. Ferrari, and R. Pallas-Areny, "Synchronous demodulator for autonomous sensors," *IEEE Trans. Instrum. Meas.*, vol. 56, no. 4, pp. 1219–1223, Aug. 2007.
- [8] R. M. Ford, R. S. Weissbach, and D. R. Loker, "A DSP-based modified Costas receiver for LVDT position sensors," in *Proc. 17th IEEE Instrum. Meas. Technol. Conf.*, Baltimore, MD, USA, pp. 1448–1452, May 2000.

A Study on Programming Control for Sorting Robots

Narissara Thoonthaisong¹, Tanaporn Payommai², Somsin Wangkhuntod³ and Kosin Chamnongthai⁴

^{1,2,3}Department of Electronic Engineering, Faculty of Engineering and Technology, Rajamangala University of Technology Isan, Thailand.

⁴Department of Electronic and Telecommunication Engineering, Faculty of Engineering, King Mongkut's University of Technology Thonburi, Thailand.

E-mail: j_payommai@hotmail.com

Nowadays, the advancement technology of robotics in today's era. Robotic transportation systems are being developed greatly. Therefore, the robot system is important for the safety of working in industrial systems such as battery factories. Both water and dry Nano Coating Chemicals for Solar Cell Surface Coating. Therefore, transport robots play an important role in transporting heavy equipment, careful and timely delivery. To allow robots to work instead of humans in the transportation of goods within the factory. Therefore, the researchers are interested in applying the information obtained from robot technology to be useful in such work. As for the transport simulation after the factory production line, To reduce cost, increase safety and reduce human working time. Therefore, there is interest in the application of the DOBOT Magician robotic arm cooperate with the walk-behind car by using a microcontroller to help control the robot arm to pick up the mock-up product by the station. To create a station-based transport robot in the form of a transport simulation in a flat factory environment. It will make transportation more convenient, save time, can reduce the use of human labor. and increase the safety of workers in the workplace even more. The principle of operation by means of setting conditions for the robot to follow a predetermined path. is to get the value from the detector to meet condition 1. If true, the robot must stop walking. If false, condition 2 is checked. If condition 2 is true, the robot will turn left or right. If false, the robot will go ahead as follow Fig.1.

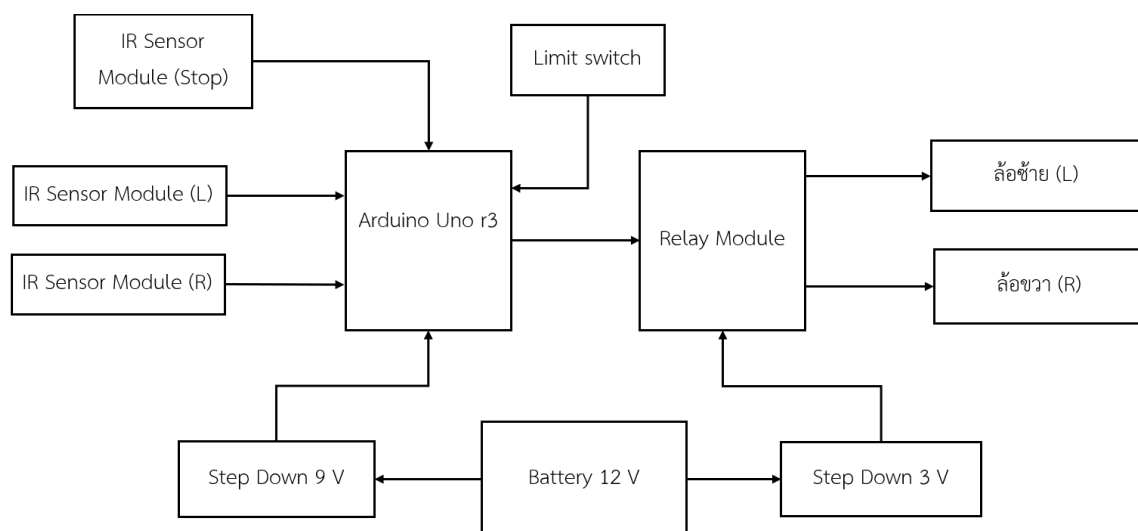
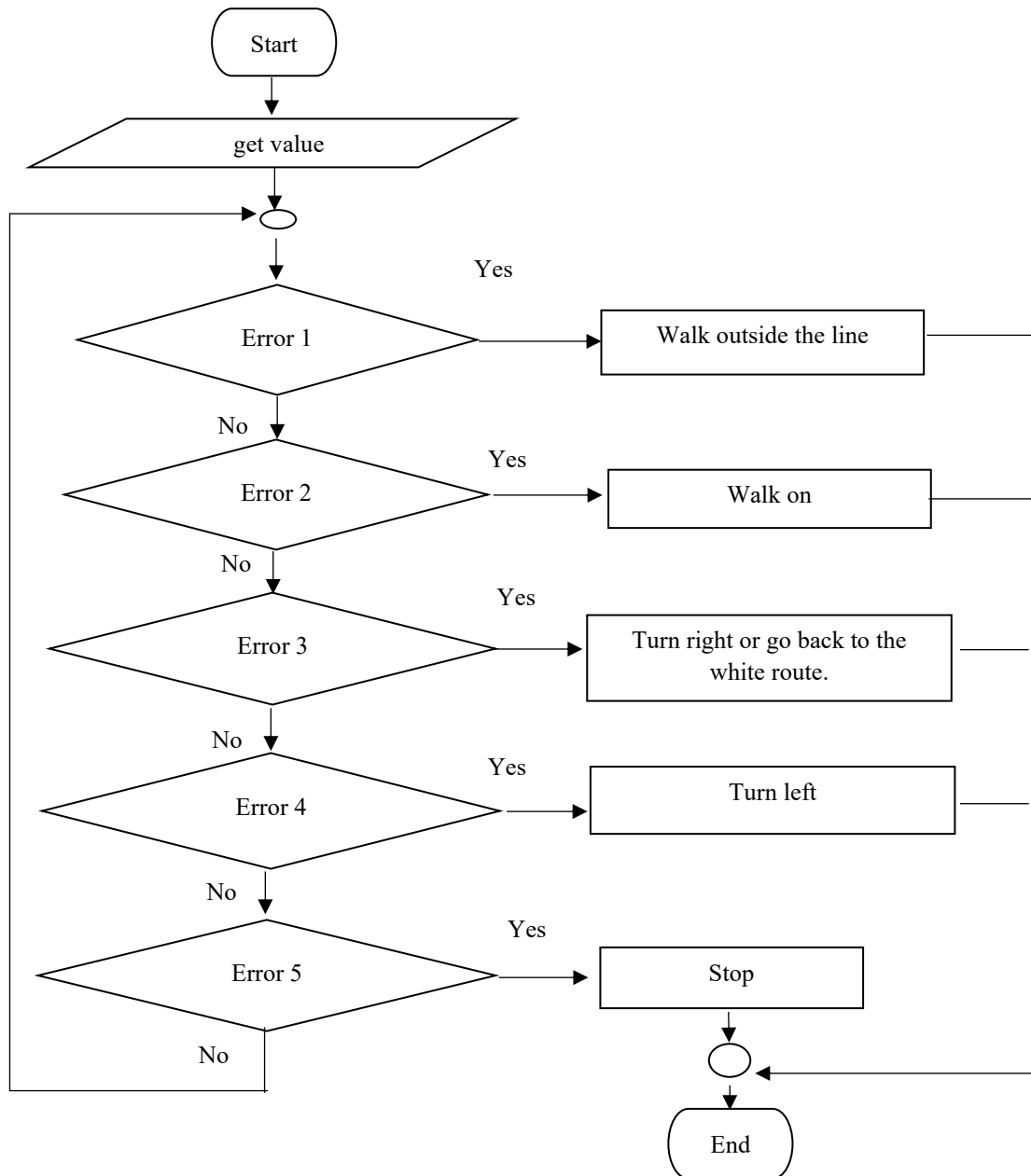


Fig.1: Block diagram of the running car running along the line.

The work plan after the trial when faults were found. The correction was to modify the work plan of the linear robot system by adding 5 sensors and using PWM to help reduce the error of the line. Running with a relay that acts like a switch and there is a high error at the station's stopping angle The PWM system solves the problem of linear walking by finding the error value of the object sensor device added by checking the error value to determine the direction of the car. work change plan as follow Fig. 2.

**Fig. 2:** Flowchat of working schematic diagram of a line walking robot.

The coding base on Working on connecting a robot arm to a walk-behind car The robot arm can be connected to the microcontroller board through the interface legs of the DOBOT Magician robot arm to transmit a pulse signal for each leg when the working conditions are met.

The results, all operations can be specified conditions and can go forward, turn left and right, go off the track, can stop and continue working. Implementation of the construction of a model project of a station-based transport robot system can be continued in the part of the robot arm DOBOT Magician to be used to model the station transport robotic system to complete.

A Resistorless Temperature-insensitive Electronically-adjustable Single VDGA-based Voltage-mode Instrumentation Amplifier

Montree Siripruchyanun¹, Burin Theppota², and Wiset Saksiri³

^{1,2,3}Department of Teacher Training in Electrical Engineering, Faculty of Technical Education, King Mongkut's University of Technology North Bangkok, Bangkok, THAILAND

montree.s@fte.kmutnb.ac.th¹, burin.tpt@gmail.com², and wiset@kmutnb.ac.th³

Abstract—This article describes a novel voltage-mode instrumentation amplifier with fully electronic controllability and temperature insensitivity. Its circuit description is very simple comprising only single active building block namely voltage differencing gain amplifier (VDGA) without any passive elements to achieve high differential-mode gain and common-mode rejection ratio (CMRR). Its gain can be widely adjustable by electronic method via input bias currents, it then can be easily modified to automatic or microcontroller-based control systems. Several performances of workability of the proposed instrumentation amplifier are disclosed using PSpice simulation with the model parameter of 0.25 μ m CMOS process. The output deviation due to temperature variation is about 0.00135%/°C. The total harmonic distortion (THD) of output voltage is 0.89%. Total power consumption of the proposed circuit is 0.18mW at ± 1.2 V power supply.

Introduction—Generally, an instrumentation amplifier (IA) is an important circuit in analog signal processing. It can be found in bio-medical sensing [1], data acquisition systems, industrial process control, readout circuit of biosensors, automotive transducer and linear position sensing [2]. The IAs are employed to enlarge a significant differential signal and to suppress any unwanted common mode signals, noise and disturbances [3]. The IAs having high common-mode rejection ratio (CMRR) and tunable differential-mode gain (Ad) are definitely demanded.

From survey of the mentioned voltage-mode IAs obtainable in the literature [4-8], most of the voltage-mode IAs confront main drawbacks. For instance, they comprise a resistor which degrade the performance of the IAs, as stated earlier. Their gains of some voltage-mode IAs cannot be electronically controlled, they are not suitable for both automatic and microcontroller-based controls. In addition, the output voltages of the most voltage-mode IAs depend on variation of temperature due to temperature dependence of the semiconductor devices used in the circuits. Consequently, when they are employed in temperature change environment, their circuit stabilities are deficient. particularly in microcontroller-based and automatic control systems. The example applications can be found in [9-10]

In this work, an attempt to design a voltage-mode instrumentation amplifier with improved performance in such electronic controllability and temperature insensitivity using the VDGA as active building block is proposed. It uses only single VDGA with free from resistor to achieve a high CMRR. Its differential gain and CMRR are high. Furthermore, power consumption is low. The electronic tunability of the differential gain is an included feature. Non-idea analysis is disclosed to survey the performance of the proposed IA. Lastly, PSpice simulation results are included to show workability of the proposed circuit.

Main proposed—Fig. 1 is the proposed IA using VDGA including its output equation. Fig. 2 shows the time responses by adjusting the bias currents I_{BA} to be 20 μ A, 40 μ A and 60 μ A, where input is a sinusoidal signal with frequency of 1kHz and 10mVp-p amplitude and setting $I_{BB} = 50\mu$ A and $I_{BC} = 30\mu$ A as constant values. The simulated results from the test can be seen that the signal gain changes according to the adjustment of the bias current I_{BA} or the signal gain can be controlled by electronic method. Particularly, temperature dependance of the output voltage was also disclosed, as seen in Fig. 3. It founds that the output voltage is slightly relied on temperature variation for 0, 27, 50 and 100 °C, where input is a sinusoidal signal with frequency of 1kHz and 10mVp-p amplitude. In addition, Fig. 4 depicts output voltage deviation relative to temperature variation from 0 to 100 °C, it is seen that the average output voltage deviation due to temperature variation is less than 0.00135%/°C, it can be ignored for conventionally accurate applications.

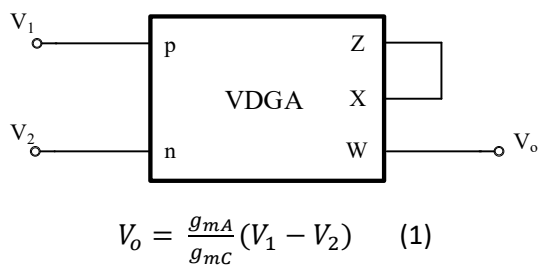


Fig. 1. Proposed VDGA-based instrumentation amplifier.

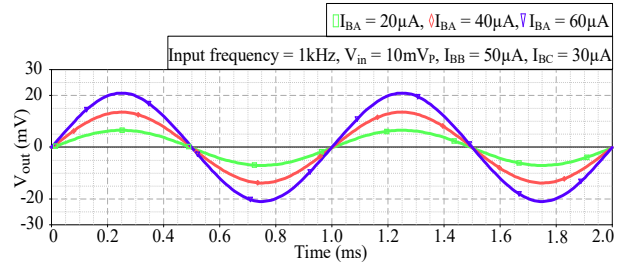


Fig. 2. Transient responses of the output voltage obtained from the proposed IA for adjusting I_{BA} .

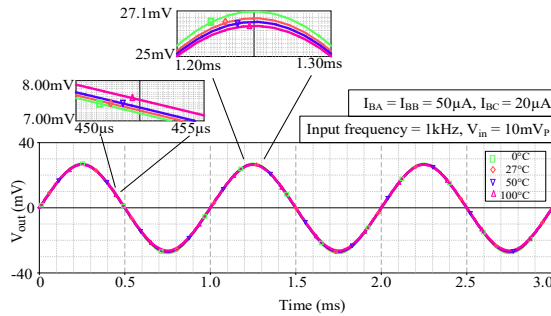


Fig. 3. Temperature dependence of the output voltage for temperature variation of 0, 27, 50 and 100 °C.

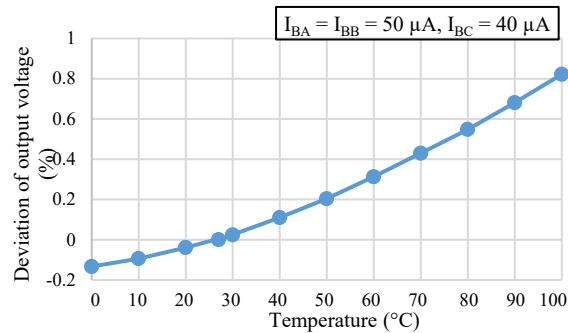


Fig. 4. Output voltage deviation relative to temperature variation.

Conclusion—The new voltage-mode instrumentation amplifier using only single VDGA as active building block has been presented. The proposed IA is without any passive resistors unlike the previously proposed voltage-mode IAs to achieve high differential-mode gain and CMRR. The outstanding features of the proposed IA are that it yields widely electronic controllability and output voltage is temperature-insensitive due to temperature compensation of internal transconductances of the VDGA. The given PSpice simulation results confirm several performances of workability of the proposed IA. The total power consumptions are 0.18mW at $\pm 1.2V$ power supply. Consequently, the proposed IA is suited for applications in instrumentation, industrial control, biomedical sensors and communication systems, especially, in portable electronic equipment.

References

- [1] R. Nagulapalli, K. Hayatleh, S. Barker, S. Zourob, N. Yassine, S. Rparathy, and A. Tammam, "A novel high CMRR trans-impedance instrumentation amplifier for biomedical applications," *Analog Integr Circ Sig Process*, vol. 98, pp.233–241, 2019.
- [2] R. Das and S. K. Paul, "Current mode instrumentation amplifier with CDCCC." *Analog Integr Circ Sig Process*, vol. 108, pp. 455–468, 2021.
- [3] Z. M'harzi, M. Alami, and F. Temcamani, "Low voltage, high CMRR, and wide bandwidth novel current mode current controlled instrumentation amplifier," *Analog Integr Circ Sig Process*, vol. 90, pp. 199–205, 2017.
- [4] P. Prasopsin and W. Wattapanitch, "Design of a low-power high open-loop gain operational amplifier for capacitively-coupled instrumentation amplifiers," *Int J Circ Theor Appl*, vol. 45, pp. 1552– 1575, 2017.
- [5] C. A. Prior, C. R. Rodrigues, A. L. Aita, J. B. D. S. Martins and F. C. B. Vieira, "Design of an integrated low power high CMRR instrumentation amplifier for biomedical applications," *Analog Integr Circ Sig Process*, vol. 57, pp. 11–17, 2008.
- [6] W. Bai and Z. Zhu, "A 0.5-V power-efficient low-noise CMOS instrumentation amplifier for wireless biosensor," *Microelectron J*, vol. 51, pp. 30-37, 2016.
- [7] D. M. Das, A. Srivastava, J. Ananthapadmanabhan, M. Ahmad, and M. S. Baghini, "A novel low-noise fully differential CMOS instrumentation amplifier with 1.88 noise efficiency factor for biomedical and sensor applications," *Microelectron J*, vol. 53, pp. 35- 44, 2016.
- [8] R. Sonkusare, O. Joshi, and S. S. Rathod, "SOI FinFET based instrumentation amplifier for biomedical applications," *Microelectron J*, vol. 91, pp. 1-10, 2019.
- [9] J. Hirunporm and M. Siripruchyanun, "A current-mode PID controller using voltage differencing gain amplifiers," 18th Int. Sym. On Commu. & Info. Tech. (ISCIT 2018), Bangkok, Thailand, pp. 261-265, 2018.
- [10] M. Siripruchyanun and J. Hirunporm, "A fully/electronically controllable voltage-mode Schmitt trigger based on only single VDGA and its applications," *AEU – Int J Electron Commun*, vol. 131, pp.1- 29, 2021.

Title of Abstract: Classification of COVID-19 severity based on self-reported symptoms through the Home-Isolation platform

SRIENGCHHUN CHHEANG, Wiroon Sriborrirux, and Krisana Chinnasarn

Faculty of Informatics, Burapha University, Faculty of Engineering, Burapha University, and Faculty of Informatics,
Burapha University

sriengchhunchheang@gmail.com, wiroon@go.buu.ac.th, and krisana@buu.ac.th

COVID-19 attacks the human respiratory system, where the virus can spread from person to person extremely fast. It seriously damages the national economy and human health, especially health resources. Bed limitation has become one of the big problems of health resources during this virus spread, so home isolation platform was introduced to settle this problem. Contrastingly, the number of patients using the platform is extremely high compared to doctors who need to check and diagnose the patients. We investigate using machine learning algorithms to predict the severity of COVID-19 patients who treated themselves at home through the platform. Self-reported such as symptoms, age, sex, etc, of 4079 patients that were collected while using the home isolation platform have been used. Dataset was applied to Supervised learning algorithms and selected the best algorithm for deploying as a micro-service to use with the platform. The result shows that Xgboost has the highest accuracy and time computation compared to other algorithms. Hyper-parameter optimization is also performed for the Xgboost algorithm to boost accuracy. Furthermore, the Xgboost model developed in this study has been deployed as a micro-service (API) that is available for use with other platforms that have the same dataset.

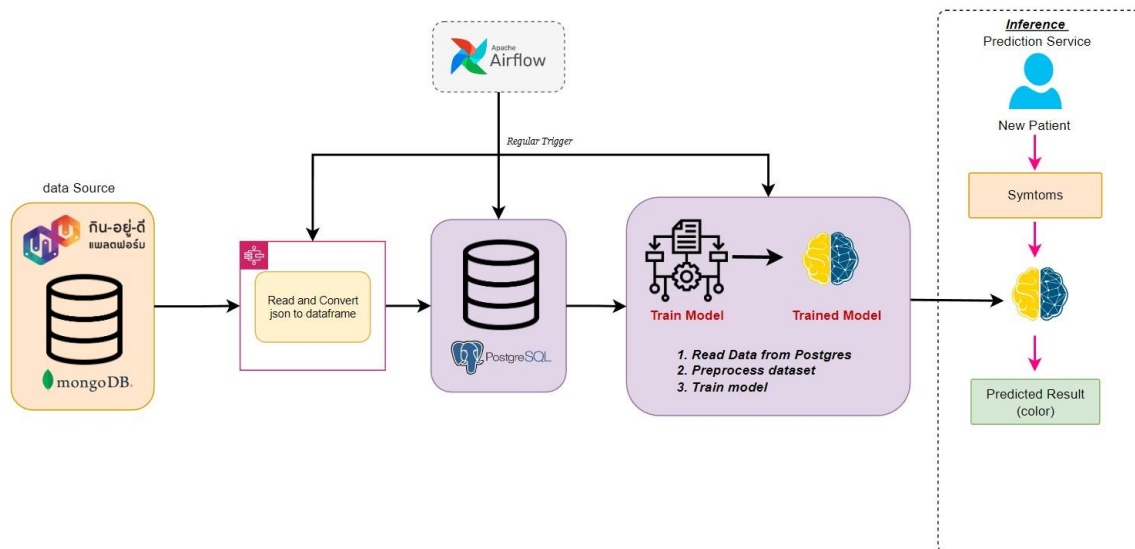


Fig.1: Full system of the Micro-service that will apply to the Home-isolation platform ([weSAFE@HOME](#))

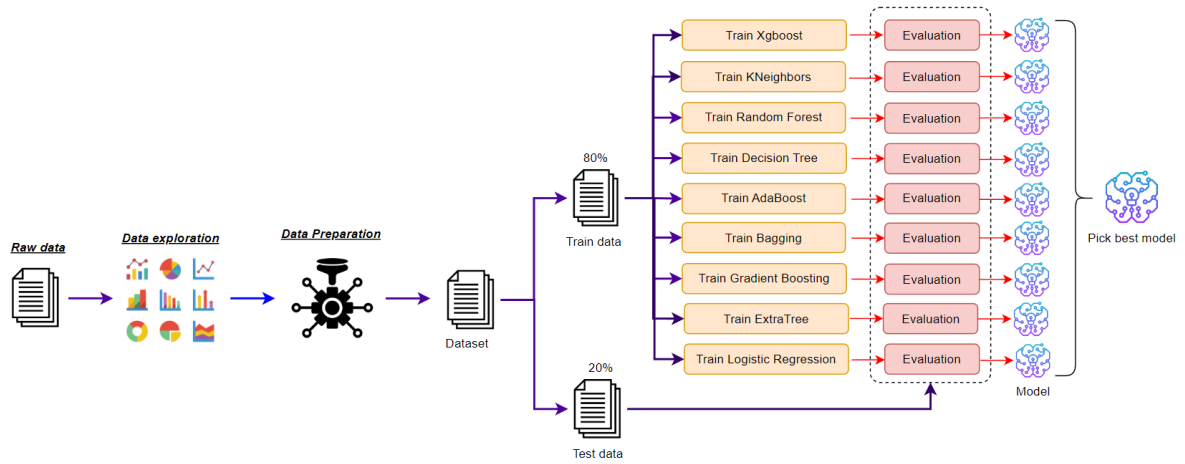


Fig.2: Training and selecting the best model flow

Semantic Scene Understanding in Fast Camera Motion Using Spatial and Local-Global Temporal Feature Fusion

Dipanita Chakraborty¹, Werapon Chiracharit², and Kosin Chamnongthai³

Department of Electronics and Telecommunication Engineering, Faculty of Engineering, King Mongkut's University of Technology Thonburi, Bangkok, Thailand ^{1,2,3}

dipanita.chakraborty@mail.kmutt.ac.th¹, werapon.chi@kmutt.ac.th², and kosin.cha@kmutt.ac.th³

To increase efficiency in video processing applications, Content-Based Video Retrieval (CBVR) is considered to be one of the essential tasks. However, the fundamental step of CBVR, known as scene understanding module lacks adequate semantic temporal feature information in existing methods [1][2]. As a result, existing methods suffer from miss classification in presence of fast camera motion activity. Therefore, this paper has proposed feature fusion based method that extracts semantic global and local temporal features corresponding to their spatial features. Whereas, global temporal features learn the velocity correlation between neighboring frames of a scene, the local temporal features learn the velocity correlation between frame objects of

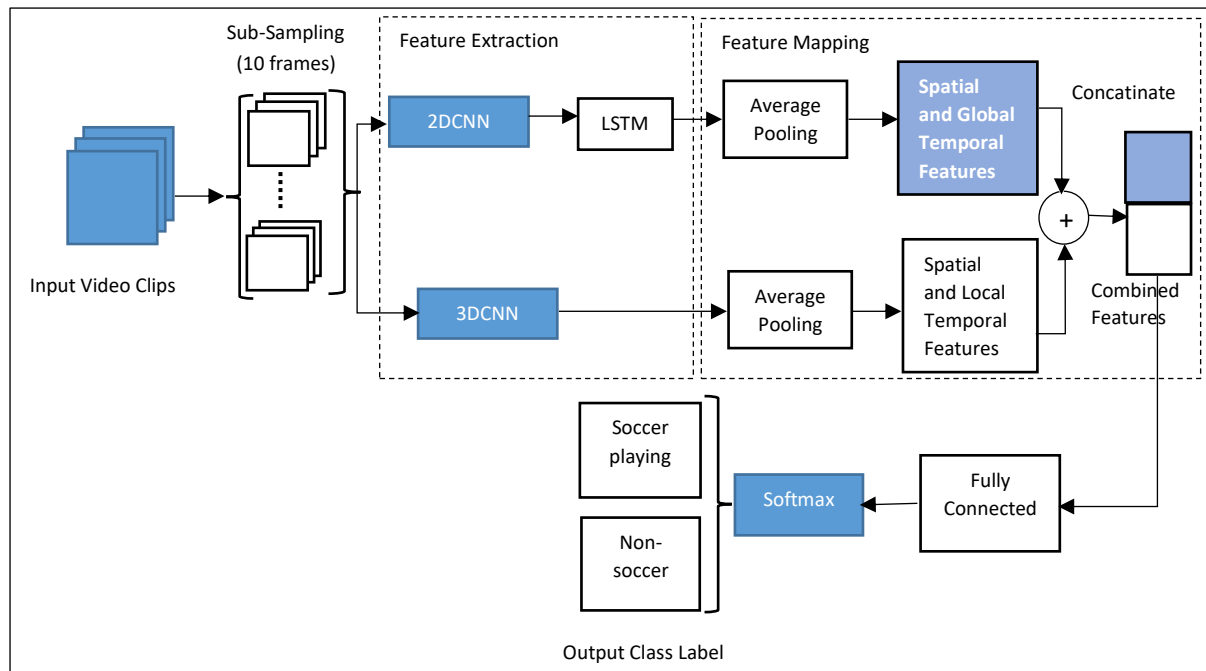


Fig.1. Architecture of Proposed Method for Semantic Scene Understanding in Fast Camera Motion

a scene. Our proposed system is able to detect soccer playing scenes in normal and fast camera motion, as shown in Table 1. We have designed our proposed system architecture in two streams, as depicted in Fig 1. Firstly, input video clip is sub-sampled into 10 frames of clips. Secondly, each 10 frame clip is fed through one stream using 2DCNN-LSTM(convolutional neural network-long short-term memory) network to extract the spatial and global temporal feature map. Simultaneously, each 10 frame clip is fed through another stream using 3DCNN (3-dimensional CNN) to extract spatial and local temporal feature map. Thirdly, feature maps from both streams are concatenated. Lastly, fully connected layer, and softmax layer are added respectively, for classifying the clips into two output class labels, soccer playing scene and non-soccer. The proposed system implementation details are illustrated in Table 2. Our two-stream 3D-CNN-LSTM based proposed method has achieved higher accuracy than the existing methods. We have compared our experimental results with other methods in Table 3.

Table 1: Example of Soccer Playing Scene in Normal and Fast Motion



Average Velocity	Soccer Playing Scene
Normal	
Fast Camera Movement	

Table 2: Implementation Specifications of Proposed System

Device	Classifier (2DCNN-LSTM and 3DCNN)
CPU: Intel(R) Core(TM) i7-10750H @2.60 GHz GPU: Nvidia Titan 1650i Memory Size: 8.00 GB System Type: 64-bit OS. Software: MATLAB R2021b	Convolution Layer: 22 Maximum Pooling Layer: 4 Average Pooling Layer: 1 Fully Connected Layer: 1 Softmax Layer: 1 2DCNN Kernel: (N×N) 3DCNN Kernel: (N×N×N) LSTM Layer: Many to One
	Input Frame Size: 224×224 MiniBatch Size: 10 video clips Iterations: 1000 Base Learning Rate: 1×10^{-4} Momentum: 0.9 Output Class Label: 2

Table 3: Experimental Results Comparison of Our Methods with Existing Methods

Methods	Overall Accuracy
HOG+SVM [1]	96%
CNN-RNN [2]	94%
Ours [3D-CNN-LSTM]	97.8%

Reference

- [1] T. Oyama and D. Nakao, "Automatic extraction of specific scene from sports video," *2015 10th Asian Control Conference (ASCC)*, 2015, pp. 1-4, doi: 10.1109/ASCC.2015.7244727.
- [2] M. A. Russo, L. Kurnianggoro and K. -H. Jo, "Classification of sports videos with combination of deep learning models and transfer learning," *2019 International Conference on Electrical, Computer and Communication Engineering (ECCE)*, 2019, pp. 1-5, doi: 10.1109/ECACE.2019.8679371.

A Phase-Locked-Loop Algorithm Enhancement for Off-Board EV Charger Based on a Three-Level NPC Converter Under Non-Ideal Three-Phase Grid Voltages

Thidarat Thanakam ¹ and Yuttana Kumsuwan ²

Graduate Program in Electrical Engineering¹ and Department of Electrical Engineering^{1,2}, Faculty of Engineering,

Chiang Mai University, Chiang Mai, Thailand

thidarat_tha@cmu.ac.th¹ and yt@eng.cmu.ac.th²

In this paper, the enhancement of the control algorithm for the three-phase three-level neutral point clamped (NPC) converter-based off-board battery charger to support the utility grid when the non-ideal three-phase grid voltage occurs is presented. By applying the standard phase-locked loop (PLL) controller into the conventional $\alpha\beta$ -PLL algorithm, it is possible to obtain more accurate grid angle and sinusoidal grid currents to conserve the grid power quality and support the EV battery charging. The system operations are verified in the simulation results.

Off-board battery chargers with dc charging applications have become widespread due to the rapid advance of electrical transportation technology. Their dc charging applications are based on the charging power level standard of Level-2 (power levels up to 19.2 kW) and Level-3 (high-power fast charging). In off-board electric vehicle (EV) charger systems, AC-DC conversion is the main factor of battery charging. Either two-level converters or multi-level converters are used in off-board chargers. When compared with the two-level converters, the multi-level converters provide lower switching loss, less electromagnetic interference, and better waveform quality to meet the high-power charging requirements. The converters are interfaced with the utility grid to convert AC to DC power for EV battery charging. In the low-voltage distribution system, the non-ideal grid voltage including voltage distortion and voltage imbalance, are the main problem. As a result, the chargers cannot correctly detect a grid angle, which leads to unworkable charging and affects power grid quality. To overcome the problem, the enhanced PLL control technique for the distorted and unbalanced three-phase grid voltages is developed based on the three-phase PLL algorithm. This method is applied to the off-board battery charger with a three-phase three-level NPC converter as shown in Fig. 1, which can support both EV battery charging and power quality of the utility grid.

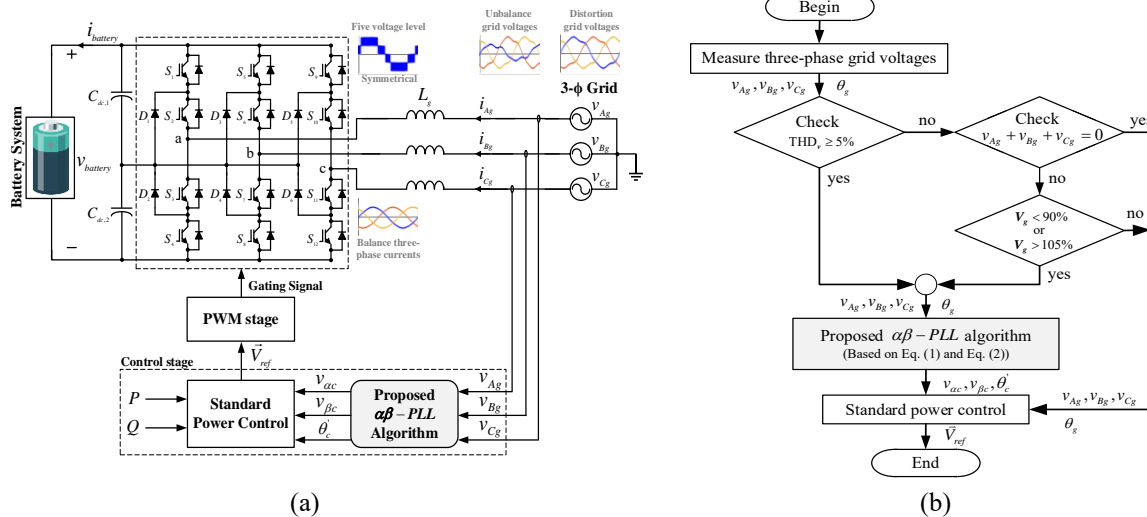


Fig.1: Schematic diagram of the operation. (a) Off-board EV charger based on three-level NPC converter-based using the proposed PLL algorithm. (b) Flowchart of the control stage for the proposed PLL algorithm.

Again, Fig. 1(a) depicts the off-board EV charger using the proposed PLL algorithm. The power stage (AC-DC) is based on a three-phase three-level NPC converter. The control stage consists of the proposed PLL algorithm and the standard current control to generate the reference voltages which is used in further the pulse width modulation (PWM) stage to generate the gate signals of the switching devices. The operation of the control stage shows in Fig. 1(b). When the three-phase grid voltages are distorted or unbalanced according to the IEEE std 519TM-2014 and IEEE std 1159-1995 standards. The proposed algorithm prepares to generate new signals that correlate only with the fundamental component of the grid voltages instead of using the distorted grid voltages directly, as shown in the following:

$$v_{ac} = \hat{V}_{gc} \sin(\theta_c), v_{bc} = -V_{gc} \cos(\theta_c) \quad (1)$$

where THD_v is the total harmonic distortion of the voltage. V_g is the rms value of the grid voltage. $v_{\alpha c}$ and $v_{\beta c}$ are the α and β - axes control reference voltage, respectively. \hat{V}_{gc} is the peak value of the control grid voltage. θ_c is the control angle of $v_{\alpha c}$ and $v_{\beta c}$. and θ_g is the grid angle. Additionally, the conventional PLL algorithm is developed by applying the standard PLL after getting $v_{\alpha c}$ and $v_{\beta c}$ or θ_c . This leads to the new control angle (θ_c'), which is used as the reference angle (θ_{ref}) within the standard power control. The transfer function can be represented in terms of:

$$\frac{\theta_c'}{\theta_c} = \frac{k s + k_i}{s^2 + k s + k_i} \quad (2)$$

where k_p is the proportional gain and k_i is the integral gain.

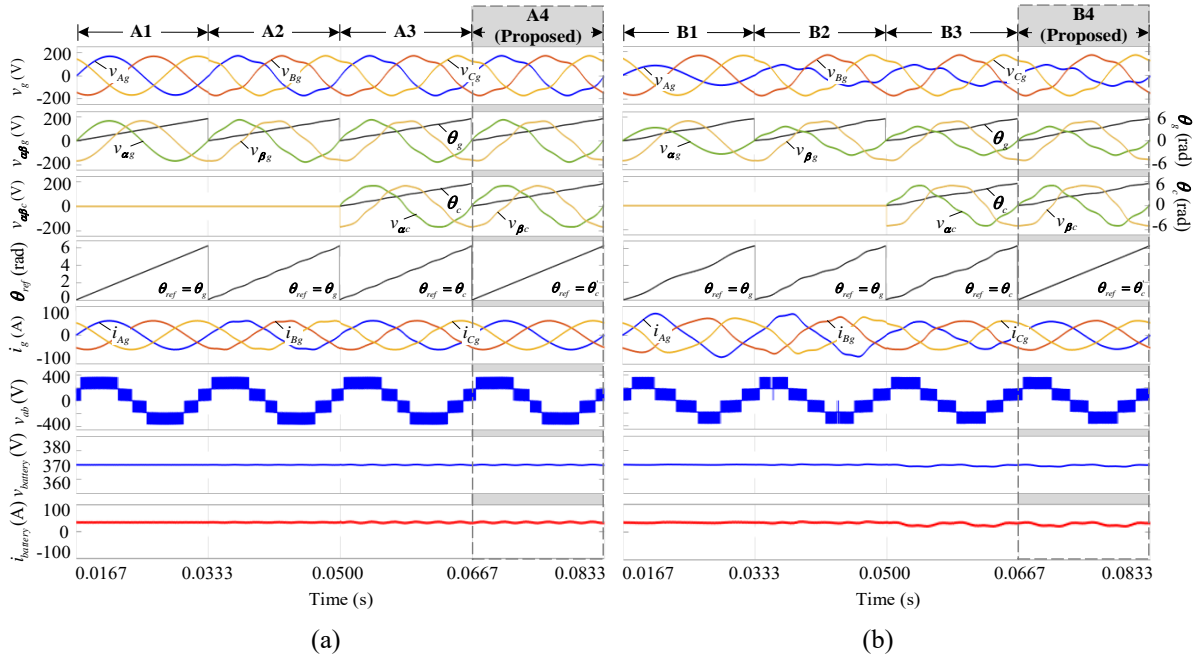


Fig. 2: Simulation results of the off-board EV charger system for the various PLL algorithms under non-ideal three-phase grid voltages. (a) distorted and balanced grid voltages. (b) distorted and unbalanced grid voltages.

In order to validate the idea of the proposed PLL algorithm for the off-board EV charger system, the simulation results were established in the Matlab/Simulink environment using the grid phase voltage of 120 V with a frequency of 60 Hz. The power rating of the off-board battery charger is 12.5 kW; the input inductor is 0.5 mH; the dc-link capacitor (C_{dc}) is 2200 μF . The switching frequency is 18 kHz and the nominal battery voltage is 370 V. The simulation results are shown in Fig. 2 under condition of case studies A (see Fig. 2(a)) and B (see Fig. 2(b)), which are only distortion and distortion together with unbalancing of the grid voltages, respectively, with 10% of THD_v . At $t = 0.0167$ s to 0.0333 s, the off-board EV charger system are initially operated with the standard PLL algorithm under the normal grid voltages (see cases A1 and B1) and switched to under the non-ideal grid voltages at $t = 0.0333$ s to 0.0500 s (see cases A2 and B2). Then, the PLL algorithms are applied with the conventional and proposed methods, at $t = 0.0500$ s to 0.0667 s (see cases A3 and B3) and $t = 0.0667$ s to 0.0833 s (see cases A4 and B4), respectively. Obviously, the proposed PLL algorithm in cases A4 and B4 can support linearity for the θ_{ref} , which is used in the standard power control, and can obtain the sinusoidal grid current waveforms, which meet the IEEE std 519TM-2014 under distorted and/or unbalanced grid voltages. Whereas, the line-to-line of the converter voltage (v_{ab}) performs five-level unipolar PWM shape in accordance with the three-level NPC converter operation. This results can confirm the performance of the off-board battery charger that employs the proposed PLL algorithm.

This paper has focused on PLL controller enhancement, which is based on the conventional PLL method by applying the standard PLL method to produce the new reference grid voltages and the new control angle. This strategy is employed in the off-board three-level NPC converter for EVs, which can support the grid power quality, especially during grid voltage distortion and unbalanced conditions. The AC-side expresses the sinusoidal grid currents with low distortion and the battery can absorb the constant power on the DC-side even with the non-ideal grid voltages.

Towards Eye Gaze Gesture Passwords Recognition

Zakariyya Abdullahi Bature¹, Kosin Chamnongthai¹ and Sunusi Bala Abdullahi²

¹Department of Electronics and Telecommunication Engineering, King Mongkut's University of Technology Thonburi, Bangkok, Thailand.

²Department of Computer Engineering, King Mongkut's University of Technology Thonburi, Bangkok, Thailand.

Zakariyya.abature@mail.kmutt.ac.th, kosin.cha@kmutt.ac.th, sunusi.ab@mail.kmutt.ac.th.

People with severe motor-related disabilities suffer to control manual switches with gaze gestures due to the sensitivity of the eyes to saccades and lack of fixation points to define the gesture very well. The existing works try to use 2D velocity features of the eyes to recognize eye gestures that can be used as passwords but, motion features approximate the fixation points to the reference frames which leads to most of the data clustering at reference points and the remaining data points were few and sparsely separated to maintain the shape and direction of the original gaze. This paper proposed subjecting 2D velocity to simple moving average (SMA) for denoising and to create more fixation points along the path of the gesture to solve the issues of eye saccades. To evaluate the performance of the proposed method, HideMyGaze datasets were used to construct new features set from eye motion features and train with multilayer perceptron (MLP) algorithms for the recognition of gaze gestures. The results show that our approach outperformed the conventional methods with 11.69% accuracy and it is applicable to disabled individuals that use eye patterns as the only input modality.

Key words: Gaze gestures, Recognition, Simple Moving Average, MLP.

I. Introduction

There are approximately over 132 million people having motor related disabilities, these people use their eye for communication [1] as they cannot move some parts of their body but can utilized their vision system which is one of the most significant parts in human that contributes largely to decision making for daily activities. With eye tracking technique nowadays, human attention can be investigated from the eye properties in real time [2]. This significantly played a vital role in many heterogeneous [3]. Human eyes fixate on relevant points or any stimulus for a short time and then moves to another point [4]. The patterns formed by these eyes movement were fast and uncontrolled due to the speed of the saccades [5] leading to noise that generally affect the performance in many applications [6].

The use of 2D optical flow approximation in [7]-[8] leads to the clustering fixation points around reference frame and saccades to be sparse leading to misclassification in password recognition from the eye gaze gesture. This work proposed usin subjecting the optical flow features in to SMA to denoised and create more missing fixations point for password gestures recognition using MLP algorithm.

II. Material and Method

The materials used in this work consist of computer having Intel(R) Core (TM) i5-10300H CPU @ 2.50GHz, RAM 8.00 GB and HideMyGaze closed eyes sub-camera Dataset. The flow chart of the proposed method was given in Fig. 1. The 2D optical motion features of the eyes was extracted and utilized. SMA function in eq. (1) denoised [9] and create more fixations points along the paths of the eyes motion and feed the signal to the multilayer perceptron (MLP) algorithms for the recognition.

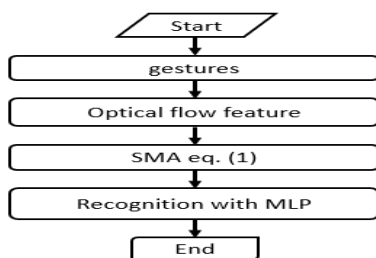


Fig.1: Flow Chart of proposed method..

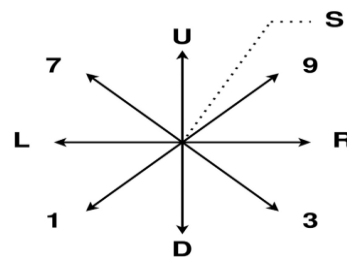


Fig.2: Gestures in HidemyGaze Dataset.

$$v_{avg} = \frac{1}{n} \sum_{i=1}^n v_i \quad (1)$$

Where v_{avg} is the denoised signal, v_i is the original signal and n is the window size between $1 < i \leq n$.

III. Results and Discussion

The dataset contained 830 gestures samples of 9 password from 20 participants. It was split into the training and testing ration of 0.9:0.1 and fed to the input layer of Back propagation MLP algorithm having sigmoid function, 50 neurons was employed with 100 iteration. The results show that, SMA improved the general performance accuracy of the recognition algorithm of these gestures passwords with 11.69% better than the conventional method.

Table 1: Comparison Result.

gestures	Accuracy (%)	MAE	RMSE
HideMyGaze [8]	74.5	Nil	Nil
Our method	86.19	1.1752	1.4619

IV. Conclusion

For years there are many efforts to operates HCI and improve gaze gesture and password recognition. with human eyes, but due to saccadic motion of the eyes, it remain very challenging. Thus, this work recognized different gaze gestures used for password with up to 86.19% accuracy using MLP algorithm. This could be assistive to the disabled individuals and may be adopted for general usage in future.

Reference:

- [1] M. Dahmani *et al.*, “An intelligent and low-cost eye-tracking system for motorized wheelchair control,” *Sensors (Switzerland)*, vol. 20, no. 14, pp. 1–27, 2020, doi: 10.3390/s20143936.
- [2] Tobii, “How do Eye Trackers works?,” <https://www.tobii.com/>, 2021. .
- [3] X. Zhang, X. Liu, S. M. Yuan, and S. F. Lin, “Eye Tracking Based Control System for Natural Human-Computer Interaction,” *Comput. Intell. Neurosci.*, vol. 2017, pp. 1–9, 2017, doi: 10.1155/2017/5739301.
- [4] S. Yeamkuan and K. Chamnongthai, “Fixational Feature-Based Gaze Pattern Recognition using Long Short-Term Memory,” in *APSIPA Annual Summit and Conference 2020*, 2020, pp. 1103–1106.
- [5] E. Chong, N. Ruiz, Y. Wang, Y. Zhang, A. Rozga, and J. M. Rehg, “Connecting gaze, scene, and attention: Generalized attention estimation via joint modeling of gaze and scene saliency,” *Springer Nat. Switz. AG*, pp. 397–412, 2018, doi: 10.1007/978-3-030-01228-1.
- [6] M. Alfaroby E., S. Wibirama, and I. Ardiyanto, “Accuracy Improvement of Object Selection in Gaze Gesture Application using Deep Learning,” in *ICITEE 2020 - Proceedings of the 12th International Conference on Information Technology and Electrical Engineering*, 2020, pp. 307–311, doi: 10.1109/ICITEE49829.2020.9271771.
- [7] R. D. Findling, L. N. Nguyen, and S. Sigg, “Closed-Eye Gaze Gestures: Detection and Recognition of Closed-Eye Movements with Cameras in Smart Glasses,” *Lect. Notes Comput. Sci. (including Subser. Lect. Notes Artif. Intell. Lect. Notes Bioinformatics)*, vol. 11506 LNCS, pp. 322–334, 2019, doi: 10.1007/978-3-030-20521-8_27.
- [8] R. D. Findling, T. Quddus, and S. Sigg, “Hide my Gaze with EOG!: Towards Closed-Eye Gaze Gesture Passwords that Resist Observation-Attacks with Electrooculography in Smart Glasses,” in *ACM International Conference Proceeding Series*, 2019, pp. 107–116, doi: 10.1145/3365921.3365922.
- [9] S. Hansun, “A new approach of moving average method in time series analysis,” in *2013 International Conference on New Media Studies, CoNMedia 2013*, 2013, pp. 0–3, doi: 10.1109/conmedia.2013.6708545.

IDF-Sign: Addressing Inconsistent Depth Features for Dynamic Sign Words Recognition

Sunusi Bala Abdullahi¹ and Kosin Chamnongthai²

Department of Computer Engineering, King Mongkut's University of Technology Thonburi Bangkok¹, Department of Electronics and Information Engineering, King Mongkut's University of Technology Thonburi Bangkok²

sunusi.ab@mail.kmutt.ac.th¹ and kosin.cha@kmutt.ac.th²

Abstracts The need for effective sign language and hand gesture models is rising due to the rapid increase in the hard-of-hearing population and the trending touchless interfaces. Existing recognition models achieved good performance using either single or/and multiple-depth spatial and temporal (SPT) raw data or reconstructing the SPT module, still are prone to misrecognition especially to dynamic sign words (DSW) because there exist many inconsistent features across hand motions and shapes. This article aims to design simple yet efficient and consistent models from the multivariate pairwise-consistency feature ranking (PairCFR) recognition approach known as IDF-Sign in SPT modules. The temporal module is obtained from the temporal hand features, while the spatial features were obtained from the moving frame average, which is calculated from each 3D frame and is found very correlated with hand gesture depth indices. The PairCFR was used to rank and select the SPT at different combined skeletal hand features. Extensive SPT model evaluations using Optimized Forest on GSL-20, DSG-40, and ASL dataset achieved 78%, 65.07%, and 95.33% of the top-1, respectively. The main specialty of the method is depicted in figure 1.

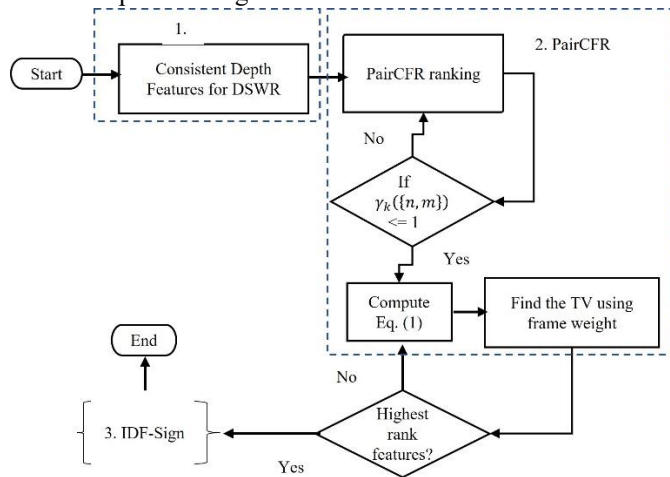


Fig. 2: The proposed method

1. Consistent Depth Features for DSWR: For example, the DSW contain video frames that have similar information and coordinates such as READ and DANCE. These words are from different classes but exhibit many frames with similar inconsistent features, leading to misrecognition. As reported in Battison 1978, there exist over 40 dynamic sign words with handshape variation in ASL which need critical observations and analysis at the wrist and fingers configuration to distinguish among them. Most of the state-of-the-art (SOT) methods treated the features separately, and their evaluations failed to capture the inconsistency depth features [1], [2], [3]. Since the standard FS and ranking methods [4] have inherited limitations of $O(2n)$ complexity. Applying these methods to DSW may provide expensive computation which lead to misrecognition. Addressing this problem, we extend the capability of the pairwise consistency FR (PairCFR) with threshold selection (TV) method to DSW depth features, where each of its evaluations identified the highly correlated features that exhibit low ranking. The selected and ranked features were further learned using TV to automatically select a midpoint value from the feature, in which less significant features will be dropped unbiasedly. The scores provided by the PairCFR-TV method can be expanded to make all new depth features to swing between 0 and 1. This is a significant achievement for the depth information $k = \{U_1, \dots, U_f\}$ of DSW since the PairCFR yields scores within a narrow range which controls training complexity, and uncertainty in modeling. The final classification is achieved using Optimized Forest (OF).

2. PairCFR: The multivariate consistency FR discriminates the redundant features using inconsistency measure I [5]. Then multivariate PairCFR function γ_k^u when $n \in \{1, \dots, z\}$ can be formulated as [5]:

$$\gamma_k^u(n) = \frac{1}{z-1} \cdot \sum_{\substack{m \in \{1, \dots, z\} \\ m \neq n}} \gamma_k(\{n, m\}) \quad (1)$$

where $\gamma_k(\{n, m\}) = 1 - I_k(\{n, m\})$ denotes the consistency metric of the subset established by the features n and m , $\forall m$ restricted at $m \neq n$.

Corollary: For $I_k(f)$, a feature subset f within a video frame V , k is obtained from the total sum of all the inconsistency count I_h for all the patterns divided by the total number of the sequences in k . However, I_h per each pattern (values of the selected features without class) is computed as the total number of the same patterns in the data set minus the number of sequences of the majority class of the pattern.

3. IDF-Sign: The method is developed using OF classification through strength of Genetic Algorithm (GA) to obtain an optimal subforest from random forest. In this article we select 20, 1, 20, and 120, for number of iterations, random seed, size of population, and batch size, respectively. The IDF-Sign is experimentally verified. The experiment is conducted with ten signers which performed each sign many times. The signers were requested to hang leap motion sensor (LMS) at their chest. The LMS provides the 3D coordinate of complete skeletal hand joints, for details readers are refer [4]. A frame rate of 64 fps and taken along x, y, and z dimension is obtained. The videos were automatically saved as comma separated value files which are readily fed into weighted linear regression to control the inherent noise. The output of the WLR is fed into the PairCFR for feature ranking and selection, finally the selected frames are fed into the OF classifier. We further performed experiment with some of the depth baseline data set: (1) Greek Sign Language (GSL) comprised of 20 dynamic word signs randomly collected from similar and non-similar signs. The data set is performed by six signers with each sign for an average of seven times. Signers were directed to stand in front of a MS Kinect sensor, and all were captured at the same positions. (2) Deutsche Gebardensprache-German Sign Language (DGS) comprised of phonetically balanced subset of HamNoSys phonemes. These syntaxes were performed by fifteen signers for an average of five times per sign. The data set is captured using a mobile system to reflect the exact real-life applications of the SLR system. We evaluate the performance of IDF-Sign using signer-dependence (SI) and signer-independence (SD). This strategy is repeated across all signers in the data set.

Results: In Tables 1-4, we provide the results of comparison between the proposed IDF-Sign with four SOT methods. The results were obtained using the stated strategies in section 3 with top-k metrics, where $k = 1, 2, 3$, and 4 respectively. However, we provide only the results of top-1 (1%) from SI which is more readily available to the SOT methods. In our PairCFR we were able to learn the consistent features and build them inside the classifier, which lead to increase accuracy of up to 4%. In addition, authors in [1] tried to enhance the performance of decision tree method though the accuracy was improved, however the PairCFR method improved the SP-boosting learning with more than 3% on GSL-20 data set. DGS evaluation, one of the authors in [1] proposed SP-boosting in which the positive feature subsets of the phoneme is believed to occur, where all other subset features were regarded negative and irrelevant. The SP-boosting achieved top-accuracy of 59.8 and 49.4% for SD and SI, respectively, however as the number of sign features rise accuracy will drop. In this case PairCFR outperformed the SP-boosting in DGS and provides an increment of more than 2%. In general, the results of the proposed PairCFR are better and improved the recognition performance of the 3D depth features, single signer features, irresponsible multi-articulatory features from non-native speaker, and non-manual features.

Conclusion: This article developed a method that is computationally feasible to learn complex manual and non-manual depth features for sign language and human action recognition. Passing the depth features into the PairCFR for learning and ranking the inconsistency features provide good basis to recognition improvement. However, the major disadvantage to this method is the discretization at some point which affect the recognition performance. The method can be extended into human action recognition and other touchless interfaces.

Table 1: Results of Comparison between IDF-Sign with SOT methods on DGS dataset @top-1% Table 2: Results of Comparison between IDF-Sign with SOT methods on GSL dataset @top-1%

Approach	Accuracy (%)	Approach	Accuracy (%)
SP + HMM [2]	55.4	SP-boosting [1]	76
Boosted [1]	49.4	Markov models [1]	54
Tr-msHMM [3]	63.1	Tr-msHMM [3]	63.1
IDF-Sign	65.07	IDF-Sign	78

Table 3: Results of Comparison between IDF-Sign with SOT methods on GSL-20 with two strategies

Strategies		Markov models		SP-boosting		IDF-Sign	
		Top-1 (%)	Top-4 (%)	Top-1 (%)	Top-4 (%)	Top-1 (%)	Top-4 (%)
Signer-Independent	1	56	80	72	91	73	94
	2	61	79	80	98	79.9	99
	3	30	45	67	89	71	93
	4	55	86	77	95	78.8	98
	5	58	75	78	98	80.6	98
	6	63	83	80	98	82	99
Avg. Accuracy		54	75	76	95	78	97
Signer-dependent		79	92	92	99.90	95.3	98.99

Table 4. Results summary of the New created data set

Class	Accuracy of approach (%)		Class	Accuracy of the approach (%)	
	FFV-BiLSTM [6]	IDF-Sign		FFV-BiLSTM	IDF-Sign
Again	90	95.3	Fork	90	95.9
Angry	90	90.5	Good	90	93.9
Bad	100	99.4	Hey	90	95.2
Child	90	88.2	Happy	80	92.7
Cheap	80	94.4	Hot	90	95.5
Dance	90	99.2	Jump	80	90.7
Eight	100	99.8	Like	90	94.8
Embarrass	100	98.1	Money	90	93.6
Expensive	90	94.9	Read	100	100
Excuse	100	98.7	Short	90	95.3

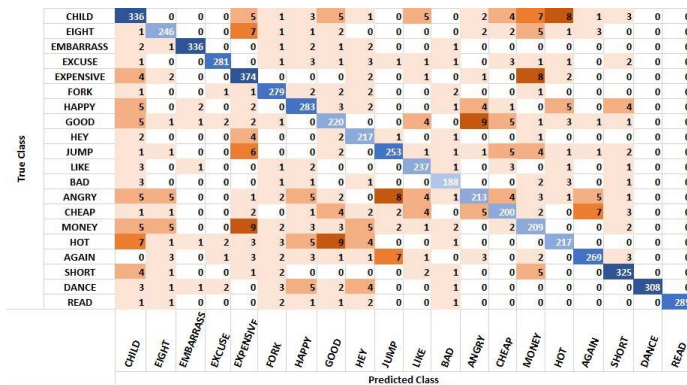


Fig. 2: The confusion matrix of the highly correlated dynamic ASL words

References

- [1] H. Cooper, E.-J. Ong, N. Pugeault, and B. Richard, "Foreword," in *Gesture Recognition*, 1st ed., S. Escalera, Ed. Cham, Switzerland: Springer International Publishing, 2017, pp. 89–118.
- [2] E. J. Ong, H. Cooper, N. Pugeault, and R. Bowden, "Sign Language Recognition using Sequential Pattern Trees," in *Proceedings of the IEEE Conference on Computer Vision and Pattern Recognition*, 2012, pp. 2200–2207, doi: 10.1109/CVPR.2012.6247928.
- [3] S. Tornay, O. Aran, and M. Magimai.-Doss, "An HMM approach with inherent model selection for sign language and gesture recognition," in *LREC 2020 - 12th International Conference on Language Resources and Evaluation, Conference Proceedings*, 2020, no. May, pp. 6049–6056.
- [4] S. B. Abdullahi and K. Chamnongthai, "American Sign Language Words Recognition of Skeletal Videos Using Processed Video Driven Multi-Stacked Deep LSTM," *Sensors*, vol. 22, no. 4, pp. 1–28, 2022, doi: 10.3390/s22041406.
- [5] F. Jimenez, G. Sanchez, J. Palma, L. Miralles-Pechuan, and J. A. Botia, "Multivariate Feature Ranking With High-Dimensional Data for Classification Tasks," *IEEE Access*, vol. 10, no. 2022, pp. 60421–60437, 2022, doi: 10.1109/ACCESS.2022.3180773.
- [6] S. B. Abdullahi and K. Chamnongthai, "American Sign Language Words Recognition Using Spatiooral Prosodic and Angle Features: A Sequential Learning Approach," *IEEE Access*, vol. 10, no. 2022, pp. 15911–15923, 2022, doi: 10.1109/ACCESS.2022.3148132.

Efficient PDM-to-PCM Converter

Rithea Sum¹, Chanon Khongprasongsiri²,
Watcharapan Suwansantisuk³, and Pinit Kumhom⁴

^{1,3,4} Department of Electronic and Telecommunication Engineering, Faculty of Engineering,

King Mongkut's University of Technology Thonburi, Bangkok 10140 Thailand

² National Astronomical Research Institute of Thailand, Chiang Mai, Thailand

Email: rithea.s@mail.kmutt.ac.th, chanon@narit.or.th,

watcharapan.suw@mail.kmutt.ac.th, and pinit.kumhom@mail.kmutt.ac.th

Sound is an essential piece of information that humans are interested in. Digital microphones are the most common sensors used to capture signals or sounds. The most common types of microphone that are used these days are the Micro-Electrical Mechanical System (MEMS) microphone due to their low cost, size, and noise robustness. MEMS microphones are embedded in many electronic devices such as smartphones, smart watches, smart speakers, computers, etc.

The output of MEMS microphones is the result of a sigma-delta oversampling ADC that is embedded in the MEMS microphone. It is a one-bit quantizer in the MHz rate of data that is encoded as Pulse Density Modulation (PDM). Unfortunately, the PDM data is not useful as the Pulse Code Modulation (PCM), which is easily analyzed and processed. In other words, the PDM data must be converted to PCM data before being further processed. The sampling frequencies of the PDM signal fall between 1MHz and 3MHz, while the PCM signals use sampling frequencies in the kHz range. Therefore, the main operation in the PDM-to-PCM Converter is downsampling and anti-aliasing filter.

The conventional methods for PDM-to-PCM signal are done by using decimation filters based on Cascaded-Integrator-Comb (CIC) filters then an anti-aliasing filter is added to remove any under-sampling frequencies that may appear in the signal. This drawback is that many filter coefficients need to be used to archive high Signal-to-Noise (SNR) values. Therefore, these days, Convolutional Neural Networks (CNNs) are used to design filters that can reduce the number of coefficients, i.e., decreasing the filter orders while maintaining the quality of the predicted signal close to the target. Lowering the number of filters order can reduce noticeable energy consumption when implementing them on embedded devices [1]. Nevertheless, decimation filters which are essential for converting PDM-to-PCM as they determine the quality of the signal passed from the MEMS microphone can be designed using the concept of CNNs. Vitolo, et al. [2] proposed a conventional method for a PDM-to-PCM converter based on 1-dimension CNN. It performs two of 1D-convolutions that use 89 trainable parameters for predicting the PCM signal from PDM.

In this paper, we develop a method for a PDM-to-PCM converter that is sufficiently accurate and uses fewer parameters than the conventional method. The proposed method utilized an IIR filter to decimate PDM signals to a kHz range and used CNN subsampling to filter out the unwanted frequencies for archiving aliasing-free signals. This method reduces the number of trainable parameters by 65 percent while keeping the quality of the predicted PCM signals to an acceptable factor based on the calculation of the Mean Absolute Error (MAE) compared to the original PCM signal. The main contribution of this paper are the following: 1. a method of approximating the PCM signal from PDM with IIR downsampling filter and CNN subsampling 2. a comparison of the proposed method with the conventional method in terms of the number of parameters used in approximating the PCM data and 3. the comparison of the original PCM signal to the predicted PCM signal in terms of MAE.

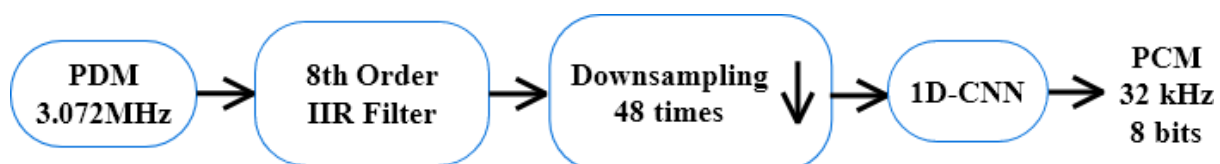


Fig.1 The proposed architecture for PDM-to-PCM Converter

The architecture of the proposed method is divided into two stages. As shown in Fig. 1, the input PDM signals are downsampled by a factor of 48 from 3.072 MHz signals using an 8th-order IIR filter in the first stage. The output from this stage is a signal with a sampling rate of 64 kHz. These signals are then passed to the proposed method's second stage, which utilizes 23 parameters from 1D-CNN as an anti-aliasing filter to remove the unwanted frequencies. Finally, the proposed 1D-CNN-based filter outputs a PCM signal with a sampling frequency of 32 kHz and 8-bit depth words.

To evaluate the proposed method, we first compare the number of parameters required by the conventional CNNs-based PDM-to-PCM Converter [2] with our proposed method. The proposed method reduces the number of parameters needed by 65%. Then, the mean-square error is introduced to evaluate the proposed method's correctness. According to the proposed method, we archive the 0.0026 MAE, which is acceptable and comparable to the conventional method. Fig.2 demonstrates an output example compared with the original PCM signal in the time and frequency domain, which did not illustrate the obvious difference. In other words, the number of reduced parameters did not affect the quality of the result, and it depicts the better quality of the result in some cases. Therefore, the proposed method is suitable for further implementation on the embedded device to decrease energy consumption.

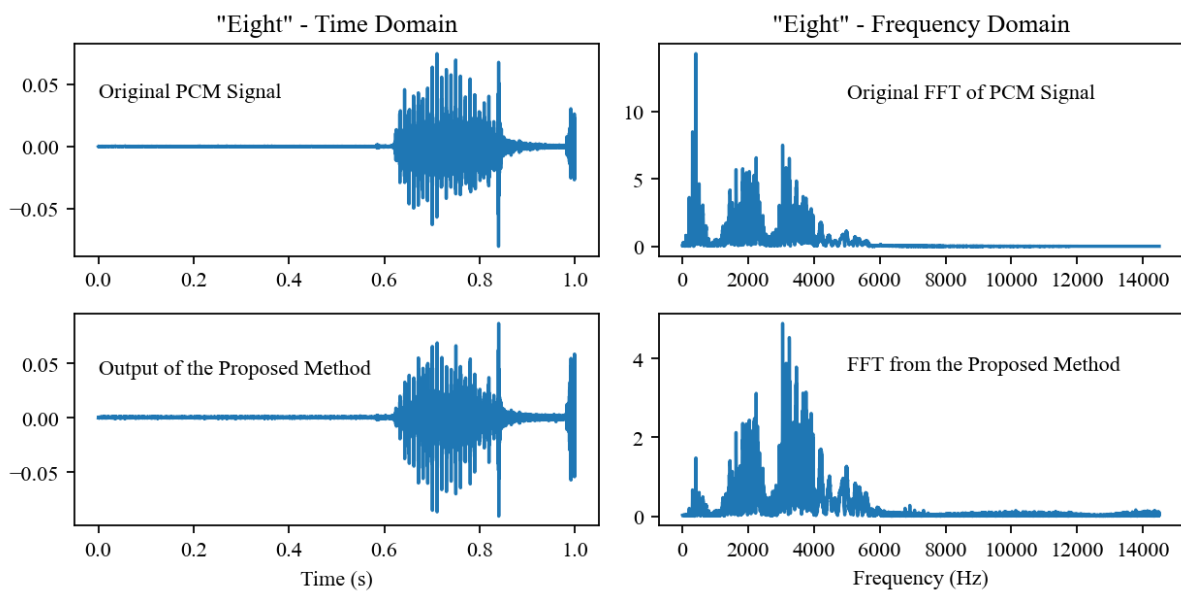


Fig.2 Audio signal "Eight" represent in Time and Frequency Domain

Reference

- [1] S. Aggarwal, "Efficient design of decimation filter using linear programming and its FPGA implementation," *Integration*, vol. 79, pp. 94-106, 2021/07/01/ 2021, doi: <https://doi.org/10.1016/j.vlsi.2021.03.008>.
- [2] P. Vitolo *et al.*, "Quantized ID-CNN for a Low-power PDM-to-PCM Conversion in TinyML KWS Applications," in *2022 IEEE 4th International Conference on Artificial Intelligence Circuits and Systems (AICAS)*, 13-15 June 2022 2022, pp. 154-157, doi: 10.1109/AICAS54282.2022.9869909.

INDEX

(By Name)

A		Hiromu Koda	9
A. Waris	15	Hoang Thi Yen	3
Agung Tri Wijayanta	20, 29, 31	Hoang Trong Thuc	IV
Ahmad Imam Rifa	20	Hua Li	16
Akihito Nagahama	5, 7	I	
Ali Mehdi	13	I G B Baskara Nugraha	15
Apiwat Sangnoree	18	J	
Arika Fitonna Ridassepri	29	Jiro Ida	III
B		K	
Boonserm Kaewkamnerdpong	47, 49	Katsuhiko Nishinari	5
Budi Kristiawan	20, 31	Kayoko Yamamoto	11
Burin Theppota	58	Kazuki Nishi	1
C		Kenji Tanaka	5, 7
C. Wulandari	15	Khunanon Karawanich	45
Chanon Khongprasongsiri	71	Kinkind Raras Heliani	29
Chao Ding	16	Koji Enoki	20, 31
Chatchai Paengkumhag	47, 49	Korpakit Kobthanyakit	41
D		Kosin Chamnongthai	43, 47, 49, 56, 62, 66, 68
Dineshwar Doddapaneni	27	Krisana Chinnasarn	60
Dipanita Chakraborty	62	Krit Angkeaw	53
Do Duy Nhat	25, 27	M	
F		Miu Fujita	1
Fitria Rahmawati	29	Montree Siripruchyanun	58
G		Muhammad Kamran	11
Guanghao Sun	3	N	
H			
Hideo Isshiki	13		

The 4th ASEAN UEC Workshop 2022

Narissara Thoonthaisong	56	T	
Natapong Wongprommoon	39	Tanaporn Payommai	56
Nghia Cao Xuan	33	Thidarat Thanakam	64
Ngoc-Tuan Do	37	Tien Hai Nguyen	22
Nguyen Quang Dat	25, 27, 35	Tin Suwanmad	41
P		Trio Adiono	II
Pattara Kladkaew	51	Trong Thanh Han	33
Pham Thanh Hiep	I	V	
Phu-Cuong Le	37	Van-Nam Le	37
Pinit Kumhom	71	Van-Phuc Hoang	37
Pipat Prommee	45	Veronica Bolon-Canedo	V
Preechar Thongdit	53	Vijender Kumar Solanki	27
Q		W	
Qing Shen	16	Warissara Limpornchitwilai	47, 49
Quang Huy Duong	22	Watcharapan Suwansantisuk	71
Quang Nguyen Van	33	Werapon Chiracharit	51, 62
R		Wibawa Endra Juwana	31
Rithea Sum	71	Wiroon Sriborrirux	60
S		Wiset Saksiri	58
S. Permana	15	Y	
S. Pramuditya	15	Yumeno Hatori	7
Shun Kitakaze	9	Yuttana Kumsuwan	64
Siradanai Srisamranrungrueang	39	Z	
Siraphop Tooprakai	41	Zakariyya Abdullahi Bature	66
Somsin Wangkhuntod	56		
Sriengchhun Chheang	60		
Sukmo Utomo Abdillah Amin	31		
Sunusi Bala Abdullahi	66, 68		
Surachai Chanchay	53		
Susanta Malakar	43		

INDEX

(By Last name)

A		H	
Abdullahi Sunusi Bala	66, 68	Han Trong Thanh	33
Adiono Trio	II	Hatori Yumeno	7
Amin Sukmo Utomo Abdillah	31	Heliani Kinkind Raras	29
Angkeaw Krit	53	Hiep Pham Thanh	I
B		Hoang Van-Phuc	37
Bature Zakariyya Abdullahi	66	I	
Bolon-Canedo Veronica	V	Ida Jiro	III
C		Isshiki Hideo	13
Chakraborty Dipanita	62	J	
Chamnongthai Kosin	43, 47, 49,56, 62, 66, 68	Juwana Wibawa Endra	31
Chanchay Surachai	53	K	
Chheang Sriengchhun	60	Kaewkamnerdpong Boonserm	47, 49
Chinnasarn Krisana	60	Kamran Muhammad	11
Chiracharit Werapon	51, 62	Karawanich Khunanon	45
D		Khongprasongsiri Chanon	71
Dat Nguyen Quang	25, 27, 35	Kitakaze Shun	9
Ding Chao	16	Kladkaew Pattara	51
Do Ngoc-Tuan	37	Kobthanyakit Korpakit	41
Doddapaneni Dineshwar	27	Koda Hiromu	9
Duong Quang Huy	22	Kristiawan Budi	20, 31
E		Kumhom Pinit	71
Enoki Koji	20, 31	Kumsuwan Yuttana	64
F		L	
Fujita Miu	1	Le Phu-Cuong	37
		Le Van-Nam	37
		Li Hua	16

The 4th ASEAN UEC Workshop 2022

Limpornchitwilai Warissara	47, 49	Sun Guanghao	3
M		Suwanmad Tin	41
Malakar Susanta	43	Suwansantisuk Watcharapan	71
Mehdi Ali	13		
N		T	
Nagahama Akihito	5, 7	Tanaka Kenji	5, 7
Nguyen Tien Hai	22	Thanakam Thidarat	64
Nhat Do Duy	25, 27	Theppota Burin	58
Nishi Kazuki	1	Thongdit Preechar	53
Nishinari Katsuhiko	5	Thoonthaisong Narissara	56
Nugraha I G B Baskara	15	Thuc Hoang Trong	IV
P		Tooprakai Siraphop	41
Paengkumhag Chatchai	47, 49	V	
Payomma Tanaporn	56	Van Quang Nguyen	33
Permana S.	15	W	
Pramuditya S.	15	Wangkhuntod Somsin	56
Prommee Pipat	45	Waris A.	15
R		Wijayanta Agung Tri	20, 29, 31
Rahmawati Fitria	29	Wongprommoon Natapong	39
Ridassepri Arika Fitonna	29	Wulandari C.	15
Rifa Ahmad Imam	20	X	
S		Xuan Nghia Cao	33
Saksiri Wiset	58	Y	
Sangnoree Apiwat	18	Yamamoto Kayoko	11
Shen Qing	16	Yen Hoang Thi	3
Siripruchyanun Montree	58		
Solanki Vijender Kumar	27		
Sriborrirux Wiroon	60		
Srisamranrungrueang Siradanai	39		
Sum Rithea	71		